UNIVERSITÀ
DEGLI STUDI
FIRENZE

INTERNATIONAL DOCTORATE IN
ATOMIC AND MOLECULAR PHOTONICS

CICLO XVIII

COORDINATORE Prof. Roberto Righini

A Bosonic Mixture for the Simulation of Impurities and Quantum Magnetism in Optical Lattices

Settore Scientifico Disciplinare FIS/03

Dottorando
Stefano Conclave

Tutor
Dott. Francesco Minardi

Coordinatore
Prof. Roberto Righini

Anni 2012/2015

It comes as no surprise he's taken by surprise.

Contents

Introduction

The last decade or so has seen the application of ultracold atoms in a great variety of research fields, stemming from the from the original application in studies on quantum degeneracy [1] and in the context of atom optics [2]. This growing interest has been motivated by their nature of simple and relatively controllable quantum system, which gets as close as modern experiments can do to realizing almost ideal and a priori noise-free conditions [3], yet accompanied with a wide tunability in specific relevant features, such as the interaction coupling [4].
Above all, the addition of optical lattices [5] in the experiments has allowed so far outstanding achievements in a wealth of aspects of research on quantum matter, from the early realizations of condensed matter models, most importantly [6], to the contributions in the field of critical phenomena [7, 8] or the simulation of exotic gauge fields [9, 10], just to name a few. At the same time, many technical advancements have been introduced that furthermore increased the range of accessible information in the experiments, most importantly the single site imaging recently obtained on both bosonic lattice systems [11, 12] and fermionic ones [13].

In the modern perspective of research on cold atoms, to experimentally tackle different classes of problems, the most suitable atomic species are chosen for the experiments depending on their specific properties. For instance, heavy alkali-earth-like atoms allowed to experimentally emulate SU(N) symmetric models [14–16], given their large total angular momentum (which is identified as the spin degree of freedom, for what concerns cold atoms) and level structure, with ultra-narrow transition lines; dipolar gases have been employed to implement long-range and typically anisotropic interactions [17].
In this sense, a whole other series of problems becomes accessible when more than one species is involved, realizing a quantum mixture of distinguishable components. The different subjects of mixture experiments depend on the fermionic or bosonic nature of the two components involved; as a matter of fact, though, most experiments so far were limited to the case where one of them is a fermion[1]. In recent years these (Bose-Fermi) mixtures were successfully able to address fundamental problems like the polaronic behavior of impurities in fermionic baths [20, 21].

[1] Among other reasons for this, one must note that it was very often the case for mixture experiments to be " historically " born for the purpose of using a bosonic species as the coolant for a second fermionic one [18, 19]. Consequently, they attracted an initial attention, determining a more widespread understanding of such systems.

On the other hand, the case of two distinct bosonic species is relatively less explored; most of the work which lies ahead actually goes beyond the mere extension of the knowledge gathered on fermionic problems to bosonic mirror ones. Heteronuclear Bose-Bose mixtures, in particular, have been suggested for the observation of a wealth of other exotic phases [22, 23]; a particular series of theoretical works has addressed them as candidates for the simulation of antiferromagnetic phases [24], and diagnostic techniques were also identified for such experiments which don't require the aid of high resolution imaging [25].

An important role in this context can be played by the ^{87}Rb-^{41}K experiment at LENS (Florence) [26], where this Thesis work was performed. In the past years it has allowed the first realization of multi-component lattice systems with bosons, which were used in a wide range of topics like the quantum phase transition from superfluid to Mott insulator [27], or the more recent study on a quantum impurity with adjustable coupling in a 1D bath of bosons [28]. This chosen combination of atomic species is characterized by the their tunable mutual (or interspecies) interaction, which is granted by its Feshbach resonances, a kind of collisional resonance most used in cold atoms systems. The possibility to control this interaction (while leaving unchanged that among atoms of the same species), identifies the class of problems this experiment is suitable to face.
Because this is a rare feature among standard Bose-Bose mixtures, quantitative studies in the specific case of ^{87}Rb and ^{41}K were performed for most of the proposed works on these systems. Most notably, required experimental conditions and expected results were explored for both the production antiferromagnetic phases [29, 30] and the study of Bose polaron physics beyond the Frölich framework [31, 32].

While the feasibility of these proposals has been established, at least in terms of physical requirements, their practical realization with the original Rb-K apparatus was inhibited by a series of technical limitations, which affected the stability of the experiment and the properties of the ultracold samples. Over the years, the old conception of the apparatus had become a negative bias in both its ease of use and the control over its running conditions.
Major issues regarded the atom number and the the balance among the populations of the two species. Taking as an example the subject of magnetic-like phases in the lattice, numerical simulations carried out in [30] highlighted the importance of a proper tuning in the size of the samples and the relative fraction between the populations (as in the specific value for the interaction coupling). Besides, for a sufficiently low entropy-per-particle to be achieved [29], an adiabatic state preparation protocol (as used in [33, 34]) would be required, to which a controllable initial population in the lattice sites is essential.
In the experiment, the typical size of quantum degenerate samples was about one order of magnitude smaller than in similar mixture systems (for instance [19], on different species of Rb-K). At the same time, the shot-to-shot fluctuation in the mixture balance strongly depended on the desired relative population [35]. While these differences were partly motivated by physical properties peculiar to the ^{87}Rb-^{41}K case, the system was

still open to improvements.
Besides, some aspects of the sample preparation procedure lacked a proper characterization in the old running conditions: this is the case, for instance, of the relative effect from the different laser cooling stages (especially on ^{41}K) and some of the loss processes occurring on the mixture. In absence of studies on the mixture by other experiments, these issues contributed as a second limitation to the introduction of improvements on our system.
Finally, in view of future works, two other critical aspects for an upgrade of the experiment were the possibility to perform fast transfers between the internal states of the hyperfine structure and the magnetic field stabilization.

In the course of my PhD work, all these aspects were specifically tackled in a systematic renewal of the experimental apparatus, towards its intended use for studies on the physics of impurities and ultracold bosonic mixtures in optical lattices. As we shall see in the course of this Thesis, notwithstanding several technical issues with the apparatus which arose throughout the process, the newly optimized system grants significantly improved running conditions, while also leaving room for the implementation of further upgrades on a short timescale.

The Thesis manuscript is outlined as follows:
Chapter 1 reviews the basic theory needed to understand the physics behind a cold atom experiment.
Chapter 2 is entirely devoted to the description of the experimental apparatus, focusing on the substantial changes made in the context of my PhD work.
Chapter 3 describes the offset-lock method implemented on one of our Rb laser sources and its features.
Chapters 4 and 5 present the characterization of the renewed experiment and the optimization steps which lead to the development of its procedure, as a consequence of the new conditions available for the system.

Chapter 1

Theory

This Chapter is aimed at introducing the basic elements of theory needed to understand the physics behind a cold atoms experiment, more specifically in our case of interest for bosonic atoms.

1.1 Bose-Einstein Condensation

In the framework of quantum mechanics, a fundamental distinction among particles arises when a set of identical ones is considered, as a consequence of a symmetrization "postulate". That is, the total wavefunction of the system must be either symmetric or anti-symmetric under particle exchange.
This classification is associated with the spin of the particles, dividing them into two big groups: those with half-integer spin have an anti-symmetric total wavefunction, they are called *fermions*; those with integer spin have a symmetric wavefunction, they are called *bosons*. The symmetry properties are mirrored in the particles' statistics; in the case of bosons the occupation number $n(\varepsilon_i)$ of the state with energy ε_i (and degeneracy g_i) is given by the Bose-Einstein distribution

$$n(\varepsilon_i) = \frac{g_i}{e^{(\varepsilon_i - \mu)/k_B T} - 1} \tag{1.1}$$

in terms of the chemical potential μ, the temperature T and the Boltzmann constant k_B.

In a gas, a macroscopic manifestation of this quantum mechanical property can occur, provided that the effects of temperature are made small enough.
More specifically, it can be demonstrated that for a gas of identical bosons a critical temperature T_c exists below which the occupation of the lowest energy state becomes macroscopic (in that the number of particles N_0 in this state becomes comparable to the total particle number N). This phenomenon produces a whole new phase of matter which is called a Bose-Einstein condensate (BEC), where the gas behaves as a single macroscopic matter wave.
To understand how this happens, consider how each thermal particle is characterized by an intrinsic size that quantifies the spatial extension of its wavepacket, called the *De*

Broglie thermal wavelength

$$\lambda_{dB} = \sqrt{\frac{2\pi\hbar^2}{Mk_BT}}. \tag{1.2}$$

where M indicates the particle's mass. The De Broglie wavelength can also be seen as a measure of the scale at which quantum mechanical features of the particle become relevant. As the temperature of the gas is lowered down, the particles' statistics will show up in the bulk once the mean spacing in the gas becomes comparable to λ_{dB}.
In general the BEC reflects a condensation of particles in phase space, rather than in the real space. Already from this simple considerations, it is clear that its formation depends on the interplay both temperature and density: the ratio of the two associated length scales (λ_{dB} and the inter-particle particle spacing) is called *phase-space density* (PSD) ρ_{PS} and it represents the physically relevant parameter in identifying the conditions for a BEC. Theory for the case of non-interacting bosons in a box yields a first estimate of the critical value of phase-space density to be

$$\rho_{PS} = n\lambda_{dB}^3 \simeq 2.612\,. \tag{1.3}$$

This result stands as a valuable guideline to address the experimental requirements, albeit derived for a system much different from those of typical experiments.

To give a more realistic microscopic description of what happens in real cold atom systems, in fact, one has to include in the hamiltonian the presence of:

- *Trapping potential (V_{ext})*: some kind of spatial confinement for the gas is needed in real experiments, that can be well approximated for most cases by a harmonic potential, as we shall see later on;
- *Interaction energy (V_{int})*: cold atomic samples are dilute and interact mainly via s-wave collisions, which can be modeled by a purely contact potential $V_{\text{int}}(\vec{r} - \vec{r'}) = g\delta(\vec{r} - r')$ with a coupling constant $g = \frac{4\pi\hbar^2 a}{M}$, whose only parameters are the atomic mass M and the s-wave scattering length a.

A self-consistent Heisenberg equation can be derived using this hamiltonian, using a Bogoliubov approximation, for the "condensate wave function" Φ [36, 37]. The latter is a complex wavefunction defined as the expectation value of the bosonic field operator, so that $|\Phi(\vec{r}, t)|^2$ will give the BEC density $n_0(\vec{r}, t)$. The Heisenberg equation of Φ is called the Gross-Pitaevskii equation (GPE)

$$i\hbar\frac{\delta\Phi(\vec{r}, t)}{\delta t} = \left[-\frac{\hbar^2\nabla^2}{2m} + V_{\text{ext}}(\vec{r}) + g\,|\Phi(\vec{r}, t)|^2\right]\Phi(\vec{r}, t) \tag{1.4}$$

In the case of repulsively interacting atoms ($a > 0$), an analytic solution of the GPE is possible for the ground state density, by dropping out the kinetic energy term in

(1.4) (Thomas-Fermi approximation), since at low temperatures the energy is strongly dominated by the contribution due to interactions. The result is the *Thomas-Fermi distribution* for a repulsive BEC

$$n_{TF}(\vec{r}) = \begin{cases} \frac{1}{g}\left[\mu - V_{\text{ext}}(\vec{r})\right] & \text{per} \quad \mu > V_{\text{ext}}(\vec{r}) \\ 0 & \text{per} \quad \mu < V_{\text{ext}}(\vec{r}). \end{cases} \tag{1.5}$$

which depends on the chemical potential μ. This distribution allows to address a peculiar feature, consequence of the interactions and unique to the BECs of repulsive atoms: its spatial distribution mirrors the reversed trapping potential. This is used in the experiments as a key signature to identify when a BEC is produced.
We also note that the n_{TF} vanishes abruptly over a finite distance. In reality this second aspect is not strictly correct, being an artifact induced by the failure of Thomas-Fermi approximation on the edges of the trap; still, the actual profile does not deviate strongly and the Thomas-Fermi prediction of (1.5) fits the experimental results quite efficiently.

1.1.1 Experimental realization with cold atoms

A BEC was first directly observed with ultracold atomic gases in 1995 [38, 39], following a cooling process whose essential features are still common to most current experiments. Typically, the critical phase space density is experimentally reached with two classes of techniques, one after the other [40].

The first stage relies on *laser cooling* techniques, which bring the atoms down to temperatures below 100 μK (see next Section). Inside a ultra-high vacuum system, minimizing the detrimental effect of background gas, the atoms are spatially confined by means of magnetic or optical forces, where in some cases an additional laser cooling can be performed.
A different and conclusive stage takes place inside of the trapping potential, where a forced evaporation is generally used to bring the PSD down to its critical value for the condensation.

Evaporative cooling is based on the combination of a selective removal of higher energy atoms inside the trap, with a re-thermalization of the remaining ones to a lower temperature; a sequence of such steps performed on a proper timescale, leads to a progressive decrease of the temperature in the sample, while simultaneously increasing density, at the cost of a reduction of the atom number. This general mechanism is differently realized depending on the nature of the trap (magnetic or optical, as in the discussion of the experimental results), but in optimal conditions it can always increase the PSD by at least 6 orders of magnitude. In particular, the rate of (elastic) collisions has to be sufficiently large for the evaporation to be efficient.

Cold atoms proved to be valuable candidates for mimicking many different theoretical models and real systems, due to their high cleanliness and an unparalleled degree of tunability in many parameters. An essential feature for many experiments is the possibility to tune the interactions inside the system, exploiting the phenomenon of

Feshbach resonances [4].
In cold atoms the two-body interaction only depends upon the s-wave scattering length a, which is set by the specific collisional channel the atoms are into (meaning the set of quantum numbers that identify the isolated atoms). A Feshbach resonance is observed when a bound state from a closed channel gets close in energy to the channel occupied by the atoms, typically as the magnetic field is varied, when dealing with samples polarized in Zeeman sub-levels. The phase shift acquired in the interaction process strongly varies in this case, resulting in a diverging scattering length at the resonance point between the two states [37]. For an isolated resonance the scattering length variation with the B field is well approximated by

$$a(B) = a_\infty \left(1 - \frac{\Delta_B}{B - B_0}\right) \tag{1.6}$$

where B_0 is the resonance magnetic field, Δ_B the resonance width and a_∞ the scattering length far away from it.
Thanks to this behavior in atomic systems the interaction can be tuned from attractive to repulsive, or zeroed out altogether, and even dynamically changed with respect to the relevant timescale of the experiment [41].

1.2 Laser cooling and trapping

In this section we want to briefly introduce some key concepts about the cooling and trapping techniques used in the cold atoms experiments, that will be useful in the discussion of how we developed the new experimental procedure to a double BEC. More extensive treatments of these topics can be found, for instance, in [42–44].

Our starting point is the simplest picture to describe the atom-light interaction. In this we consider a two level atom, with transition frequency ω_{12} and natural linewidth Γ for the excited state, in a monochromatic electric field of frequency ω_L. Working in the dipole limit for the field (and under the rotating wave approximation), we can write a general expression for the force exerted on the atom by the light, averaged over many fluorescence cycles, as [42]

$$\vec{F}(\vec{r}, t) = -\left[\vec{\nabla}(\phi)\,\frac{\hbar\Gamma}{2}\,\frac{s}{1+s} + \vec{\nabla}(\Omega_R)\,\frac{\hbar\delta}{\Omega_R}\,\frac{s}{1+s}\right] \tag{1.7}$$

in terms of the Rabi frequency $\Omega_R(\vec{r}) = -\frac{d\,E_0(\vec{r})\,\hat{\varepsilon_z}\cdot\hat{\varepsilon}(\vec{r})}{\hbar}$ and the saturation parameter $s = \frac{\Omega_R^2/2}{\delta^2+(\Gamma^2/4)}$, where $\delta = \omega_L - \omega_{12}$ indicates the detuning of the field from the atomic transition. The force in (1.7) can be treated in the limiting conditions when only of its two terms dominates, since they scale differently with the intensity $I_L \propto \Omega_R^2$ and the detuning δ: while the first term behaves as $\sim \Gamma^2 \frac{I_L}{\delta^2}$, the second one has a dependence $\sim I_L/\delta$.

The first contribution dominates for small detuning. It represents the *scattering force*,

whose nature is more easily understood in the case of a plane wave, when it reduces to

$$F_{\text{scatt}}(\vec{r}, t) = \hbar k_L \left[\frac{\Gamma}{2} \frac{\Omega_R^2/2}{\delta^2 + (\Gamma^2/4) + (\Omega_R^2/2)} \right] = \hbar k_L \Gamma_{\text{scatt}} \tag{1.8}$$

by conveniently substituting for the photon absorption rate Γ_{scatt}, where the factor $\hbar k_L$ gives the momentum carried by a single photon. So, the second equality in (1.8) makes it explicit that the F_{scatt} represents the variation of the atomic momentum due to the photon scattering.
This force is dissipative in nature, peaked in $\delta = 0$, and it linearly increases with the laser intensity up to a saturation value of $\hbar k_L \Gamma/2$, when approaching the saturation intensity of the transition.

1.2.1 Laser cooling in the Doppler limit

Equation (1.8) is a consequence of the fact that photons, alongside with the energy changing the internal state of the atom, also carry a finite momentum affecting the atomic motion. This stimulated process, unlike the spontaneous emission one, occurs always in a well defined direction (that of the laser propagation). The most basic laser cooling techniques, at their core, are nothing but schemes engineered to make an atom preferentially absorb counter-propagating photons with respect to its own velocity.

Optical molasses

The simplest of such schemes is called *optical molasses*. It makes use of two identical counter-propagating beams, both red-detuned from the atomic transition.
An atom with zero velocity will experience an identical contribution from the two beams, only in opposite directions, resulting in a vanishing total force; on the other hand, these same contributions won't cancel out for an atom moving with velocity v along the beam axis, due to the different Doppler shift of their frequencies.
In the atomic reference frame the counter-propagating (co-propagating) beam acquires an effective detuning of $\delta + k_L v$ ($\delta - k_L v$) that is closer to (farther away from) resonance, given that $\delta < 0$ (and provided a small enough velocity); thus realizing the basic condition for laser cooling. In particular, this force effectively behaves as a viscous one $F = -\alpha v$ for small velocities, but only up to $|v| < \Gamma/k_L$.

An intrinsic temperature limit for this scheme is set by the same fluorescence cycles it relies on. More in specific the spontaneously emitted photons involved in the process, given their random emission, determine a diffusive component to the atomic motion which counteracts the overall slowing effect: ultimately, a steady-state will be reached when friction and diffusion are reciprocally balanced. Theory predicts a temperature lower bound of $T_D = \hbar\Gamma/(2k_B)$ (for $\delta = -\Gamma/2$), called the *Doppler temperature*, which is shared by all other schemes based on the similar fluorescence mechanisms to those described above. For alkali atoms it is usually on the order of $\sim$100 μK.

Magneto-optical traps

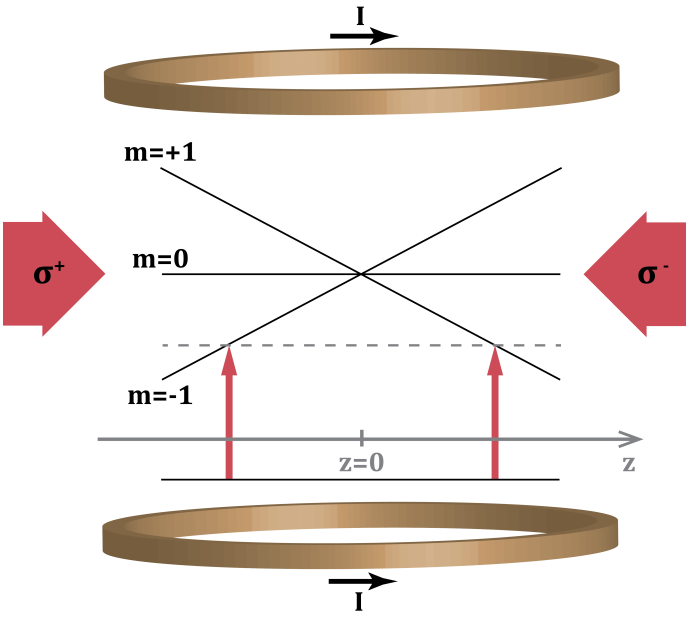

Figure 1.1: Scheme of a one dimensional MOT. The energy shift of the Zeeman levels with the position z is proportional to the black lines.

The scattering force can also be used to provide a spatial confinement together with the cooling, by combining laser beams with a small magnetic field gradient in a *magneto-optical trap* (MOT).
In one dimension (z) a MOT consists of the magnetic field $B = bz$ produced by a couple of quadrupole coils (where current runs in anti-Helmoltz configuration) and two counterpropagating laser beams, one σ^+-polarized and the other one σ^-, coming from the $z < 0$ and $z > 0$ directions respectively. Consider for simplicity a two level atom, with $F = 0$ in the ground state and $F' = 1$ in the excited one, separated by a transition frequency that sees a bare red-detuning of the lasers.
For a moving atom in $z = 0$, where the magnetic field vanishes, the MOT configuration effectively reduces to the optical molasses scheme. At the same time, for an atom stopped in $z > 0$, the magnetic energy splitting of the Zeeman sub-levels moves the laser closer to resonance on the $|F = 0\rangle \rightarrow |F' = 1, m_{F'} = -1\rangle$ transition: since the latter is driven by the σ^--polarized beam, pointing towards $z = 0$, the preferential absorption from this beam translates to a restoring force towards the center. The analogous happens on the $z < 0$ side, inverting the role of the two beams and the net result of the contributions provides the confinement effect in the MOT.
The properties of the MOT make it the ideal solution for the initial capturing and cooling stage of cold atoms experiments.

1.2.2 Optical molasses in the sub-Doppler regime

Efficient cooling techniques have been devised that overcome the Doppler limit, relying on a more realistic description of the atomic structure. They exploit the degeneracy

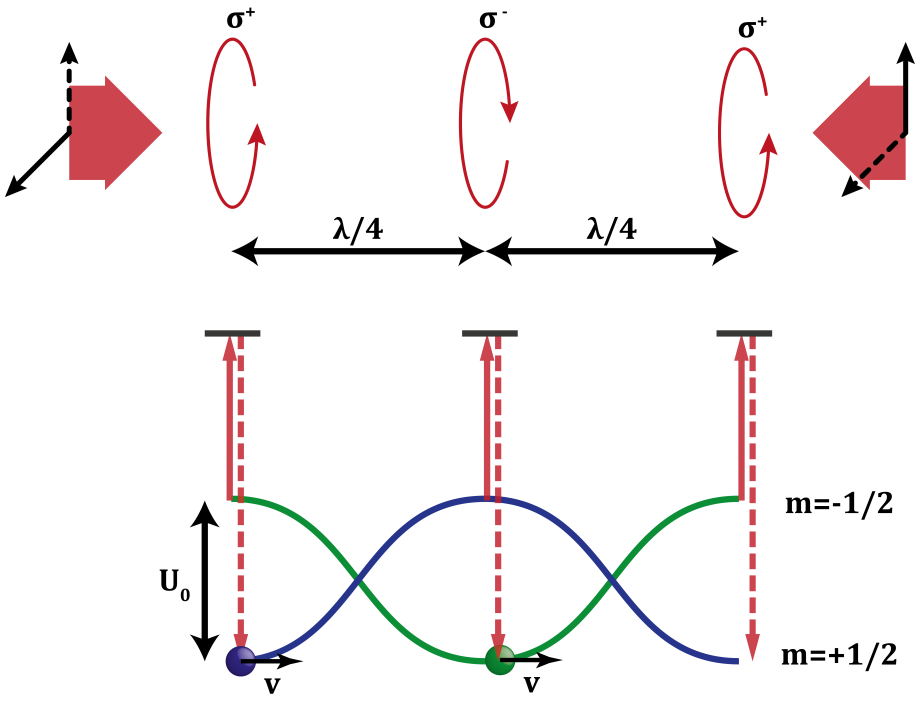

Figure 1.2: Sketch of the Sisyphus cooling mechanism in one dimension.

of the energy levels and the selection rules for optical transitions, providing the kinetic energy removal via some kind of optical pumping, rather than simple fluorescence (as in the Doppler cooling). Another common ingredient for most of them is the use of a polarization gradient in the laser field. Here we will limit our description to the scheme known as *Sisyphus cooling*, for the sake of quickly introducing some results of more general validity among the other polarization cooling techniques, such as that used on our experiment.

Sisyphus cooling makes use of two counterpropagating beams of the same wavelength λ_L, with orthogonal linear polarizations: the total field has no intensity modulation, but it possesses a polarization gradient along the beam axis, whose periodicity is $\lambda_L/2$. A σ^+ polarization gets rotated to σ^- after a distance of $\lambda_L/4$, passing by (orthogonal) linear polarizations at $\lambda_L/8$ and $3\lambda_L/8$.

Consider for simplicity an atom with a total angular momentum of the ground state $J_g = 1/2$, and no degeneracy in the excited one. In the dressed atom picture, the presence of the laser field lifts the degeneracy of the $m_g = \pm 1/2$ Zeeman sub-levels, by the light-shift energies. Then, if λ_L is sufficiently close to the atomic transition, optical pumping can also occur among the Zeeman sub-levels (Fig. 1.2).

As a consequence of the polarization gradient, a matched spatial dependence is simultaneously induced in both the light-shift and the optical pumping rates between the sub-levels. In particular, for each sub-level the energy shift maximum occurs where also the transition rate is maximum, with the maxima for the two sub-levels spatially "phase" shifted by half of a period.

The final requirement is to properly choose the detuning sign to favor the optical pumping from the high energy sub-level to the lower energy one, over the opposite process. A sketch of the resulting configuration is depicted in Fig. 1.2. A moving atom taken at the bottom of the energy curve (for instance, one in the $m_g = +1/2$ state at the point where the field is σ^+ polarized), increases its potential (internal) energy at the expense of the kinetic one as it reaches the point of its maximum light-shift, where it will most probably be optically pumped to the other Zeeman sub-level. Since the latter is lower in energy, the atom will effectively be giving away to the electric field an energy amount equal to the light-shift splitting U_0; this same process occurs every time it crosses a polarization gradient period, continuously slowing down the atom as it moves.
Within this simplified picture, a description of the cooling in terms of a mean viscous force $\propto -\alpha_{\text{subD}}\, v$ is again possible, like in the Doppler case; for all sub-Doppler schemes, though, the friction coefficient α_{subD} only depends on the laser via its wavelength and detuning, not intensity [42]. On the other hand, this description only stands corrected under the assumption that the optical pumping happens on a much faster timescale than the motion across the potential wells, a statement quantified as $v\frac{1}{\Gamma} \ll \lambda_L$. Notably, the velocity at which the approximation breaks down is found to be proportional to the laser intensity [42]: so for all polarization gradient techniques, the optical power sets the velocity capture range[1], while the cooling efficiency is independently set by the detuning.

An estimate of the limit temperature attainable with the Sisyphus scheme can be qualitatively given, considering that the cooling process will stop once the kinetic energy of the atom becomes smaller than the light-shift induced splitting U_0 between the Zeeman levels, since it won't be anymore possible for the atom to escape from a potential well. By equating $k_B T_{\text{PolGrad}} \approx U_0$ and substituting for the theory predicted value of U_0 for sufficiently large detunings [42], we get a lower temperature bound of

$$T_{\text{PolGrad}} \sim \frac{\hbar \Omega_R}{k_B |\delta|} \tag{1.9}$$

where Ω_R indicates the Rabi frequency of a single beam. This estimate, here derived heuristically for a couple of linearly polarized laser beams (which identify the Sysiphus cooling), is more strictly valid for the other σ^+-σ^- polarization gradient scheme used on our system. In most experiments, temperatures comparable to T_{PolGrad} are produced over timescales that can be on the order of a few tens of ms; a theoretical justification of this result requires a more refined approach [45, 46].

A more profound temperature limit for sub-Doppler techniques is set by the *recoil temperature* $T_R = \frac{\hbar^2 k_L^2}{2M k_B}$, which measures the energy associated to the scattering of photons from the cooling laser (of wavevector k_L); the recoil limit holds for all schemes where nothing prevents the absorption and emission processes from occurring even on an atom which approaches zero velocity, maintaining the minimum energy always above that due to photon scattering.

[1] This also implies that the processes we described will typically become relevant just for velocities at which the Doppler cooling stops being efficient (and viceversa).

1.2.3 Optical trapping

The second term of (1.7) dominates over the scattering force when $\delta \gg \Gamma, \Omega_R$ and it is associated to the off-resonant part of the atom-light interaction. In fact, a more convenient expression is given by substituting the Rabi frequency with $\Omega_R^2 = \frac{\Gamma^2 I_L}{2I_s} = \frac{6\pi\Gamma I_L}{\hbar c k_L^3}$, where we made a further substitution for the saturation intensity I_S, in order to get the explicit dependence on the detuning and the natural linewidth

$$F_{\text{dip}} \simeq -\frac{3\pi}{2ck_L^3}\frac{\Gamma}{\delta}\nabla(I). \tag{1.10}$$

We call (1.10) the *dipole force*, which is easily recognized to be a conservative one, noting that $F_{\text{dip}} = -\nabla V_{\text{dip}}$. This defines a proper dipole potential, that varies in space linearly with I_L: it accounts for the fact that a inhomogeneous distribution of the off-resonant laser intensity determines a different light-shift at each point in space. Hence an atom will have a position dependent internal energy, equivalent to V_{dip}, whose effect on the atomic motion can be described in terms of the dipole force.

The optical traps used for cold atoms are based on the effective spatial confinement provided by this conservative force [47]. Depending on the sign of the detuning in (1.10), atoms will preferably dwell in the maxima or minima of the laser intensity, for $\delta < 0$ or $\delta > 0$ respectively. The depth of the trap can be directly controlled with the intensity, the larger the latter, the deeper the trap.
In the experiments, different profiles of the laser intensities are used to produce different potentials; here we report three relevant cases, limiting the discussion to red detuned dipole lasers only:

- *Single beam traps:* For a single gaussian laser beam focused on the atoms, the trapping potential at the point of the beam waist w_0 can be taken as being harmonic, to a good degree of approximation. The trapping frequency of each direction will be proportional to the associate intensity gradient, so a single beam gives a rather shallow confinement along its propagation axis; the ratio of longitudinal over transverse trap frequencies scales as $\sim \lambda_L / w_0$, amounting to a factor of 10^{-5} or worse for typical experimental conditions.

- *Crossed dipole traps:* A direct way to get a more symmetric confinement in all directions is to confine the atoms at the crossing point of two different dipole laser beams (not interfering with each other). This produces a crossed-like configuration of the trap, whose potential around the overlap region is still harmonic for cold atoms. Indicating the maximum of the dipole potential as V_0, taken to be at the center of the overlap region of the beams, in this case we get identical frequencies $\omega_{\text{long}} = \sqrt{2V_0/w_0^2}$ along the two axes of the beams and a larger but comparable frequency $\omega_{\text{orth}} = \sqrt{4V_0/w_0^2}$ along the third (orthogonal) axis.

- *Optical lattices:* Standing waves are typically produced in the experiments by either using two counterpropagating beams at the same frequency and polarization,

or with a single retroreflected one. The intensity profile in both cases is a sinusoid, with a spatial period $d_{\mathrm{Latt}} = (\lambda_L/2)\sin\Theta$ set by the laser wavelength λ_L and the angle Θ between the interfering beams. This confines the atoms inside a periodic potential along the direction of the beam.

Whatever the intensity profile, it is a convenient choice to have large detunings on dipole lasers, in order to minimize the effect of the resonant contribution in (1.7), which heats up the atoms and allows them to escape the confinement. Since the dipole potential scales as $\sim I_L/\delta$, though, a large intensity will be needed to guarantee a reasonably deep trapping potential. In the experiments the depth of dipole potentials is usually measured in units of the single photon recoil energy of trapping light, defined as $E_R = \hbar^2 {k_L}^2/2M$ for atoms of mass M, or as the equivalent temperature of the hottest atoms V_{dip} can confine, defined via $k_B T_{\mathrm{trap}} = V_{\mathrm{dip}}$.

Chapter 2

The renewed experimental apparatus

The initial part of my PhD work was devoted to a complete reconstruction of the optical setup and some major changes in the vacuum one. This Chapter deals with the details of this work and the reasons behind it.

Just like in its previous version, our experiment extends over two separate optical tables.
The first one is entirely devoted to the optical setup of the cooling and repumping sources (*Optics' Table*), generating all the different quasi-resonant beams involved in the experiment; the detailed description of the scheme and the laser sources can be found in Section 2.4. The second optical table (*Vacuum Table*) hosts the vacuum setup and the atomic sources, presented in Sections 2.2 and 2.2.1. On the Vacuum Table we also find the 1064 nm sources of both dipole lasers (optical trap and optical lattice), whose description can be found at the end of this Chapter.

2.1 The mixture

Rubidium and Potassium belong to the group of alkali elements, characterized by an electronic ground state with a single valence electron in the outermost shell, while all low-lying ones are completely filled. In this case the only contribution to the total angular momentum is provided by the spin. For the laser cooling of all alkali atoms the D_2 line of the fine structure is most commonly used, which connects the ground state $^2S_{1/2}$ with the first excited one $^2P_{3/2}$. The presence of the nuclear spin complicates the picture, splitting these levels and adding en extra structure which goes beyond the two-level atom model.

In these real systems, then, the cooling actually occurs between specific hyperfine structure levels. Still, any chosen transition is never quite as isolated in energy as that between different fine structure levels and during the fluorescence cycles there will be a finite probability for the atoms to be pumped away from the desired cycling transition. The magnitude of this probability depends on the exact hyperfine splitting of each species' structure, but in all practical cases it requires a second laser frequency

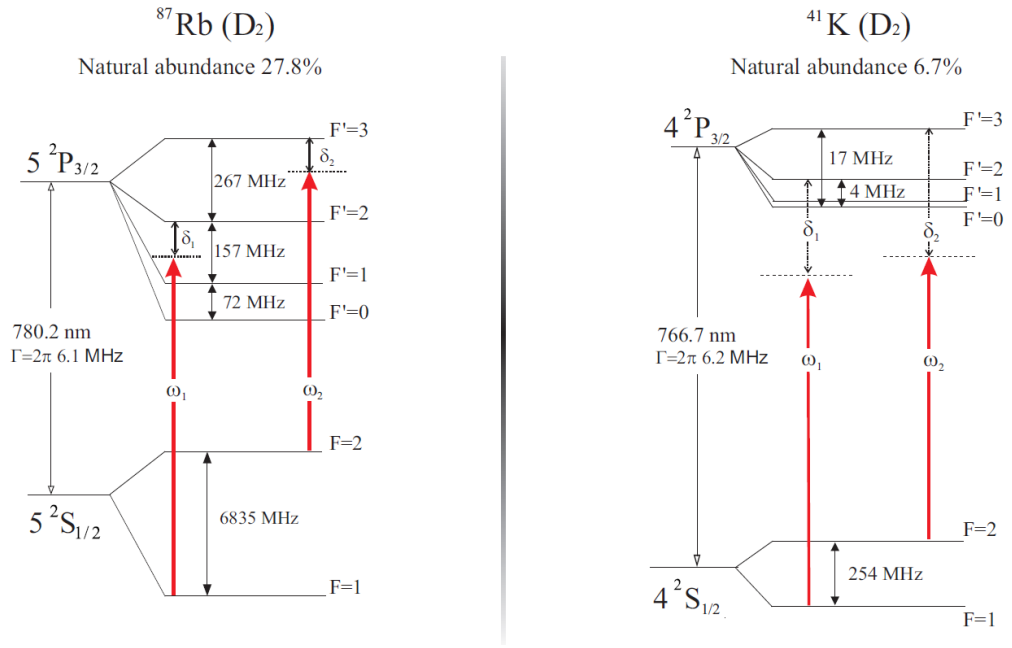

Figure 2.1: Hyperfine level structure of the D_2 line levels for ^{87}Rb and ^{41}K.

to optically pump the escaped atoms back on the cycling loop levels. So, on top of the cooling light, real systems also require a second one which is usually referred to as repumping light.

Both species in our experiment share the same nuclear spin $I = 3/2$, with the consequence of an identical hyperfine structure and the same set of allowed optical transitions according to selection rules. These are reported in Fig. 2.1, where we indicate the total angular momentum of the atom as $\vec{F} = \vec{J} + \vec{I}$ (sum of the electronic and nuclear ones respectively). The cooling transition for our species is the $|\,^2S_{1/2}, F = 2\rangle \rightarrow |\,^2P_{3/2}, F' = 3\rangle$. Cycling over this transition it is possible for the atoms to be pumped into the $|\,^2S_{1/2}, F = 1\rangle$ sub-level of the ground state, via the off-resonant transition $|\,F = 2\rangle \rightarrow |\,F' = 2\rangle$. The repumping frequency used to effectively close the cooling cycle is resonant to the transition $|\,^2S_{1/2}, F = 1\rangle \rightarrow |\,^2P_{3/2}, F' = 2\rangle$.

The ^{87}Rb ground state has a hyperfine splitting of 6.8374 GHz, while the $F' = 2 - F' = 3$ splitting in the D_2 excited manifold is enough to limit the probability of off-resonant transitions. So the repumping light requires significantly less power with respect to the cooling one, about one order of magnitude smaller.
On the other hand, the hyperfine splitting of ^{41}K is extremely small, especially for the excited state where it becomes comparable to the natural linewidth of the transition ($\simeq 2\pi \cdot 6$ MHz). Due to this, for potassium there is no easy distinction in roles between the cooling and repumping light, and similar optical powers are needed at both frequency components.

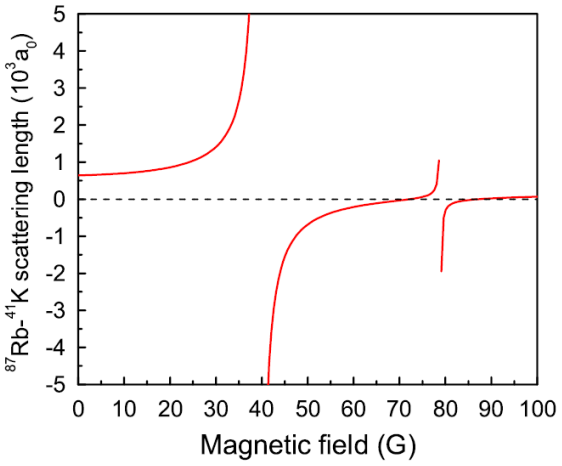

Figure 2.2: Interspecies scattering length $a_{\mathrm{Rb-K}}$ versus magnetic field for the collisional channel $\{^{87}\mathrm{Rb}$: $F=1$, $m_F=1$; $^{41}\mathrm{K}$: $F=1$, $m_F=1\}$. Semi-theoretical curve taken from [48].

2.1.1 Feshbach resonances

The species of our mixture only posses Feshbach resonances for the intraspecies interactions at high magnetic fields (~1000 G ^{87}Rb; ~440 G for ^{41}K) and the corresponding scattering lengths can be treated as constant with the magnetic field; in $|F=2,m_F=2\rangle$ for each species we get $a_{\mathrm{Rb-Rb}} \approx 99a_0$ [49] and $a_{\mathrm{K-K}} \approx 85a_0$ [50] in units of the Bohr radius a_0.
On the other hand, Feshbach resonances for the interspecies interaction were first observed at relatively low fields with the old version of our apparatus [48]: when both species occupy the $|F=1,m_F=1\rangle$ sub-level of the ground state, the scattering length $a_{\mathrm{Rb-K}}$ follows the semi-theoretical prediction in Fig. 2.2. The first broader resonance is centered in $B_0^{\mathrm{low}} = (35.2 \pm 1.6)$ G, while the second one in $B_0^{\mathrm{high}} = (78.61 \pm 0.12)$ G.
An remarkable property of the ^{87}Rb-^{41}K mixture in $|1,1\rangle$ descends from the resulting profile of the scattering length, which allows to smoothly tune the interspecies interaction from a strongly attractive to strongly repulsive regime (with a zero-crossing point in between), without crossing either one of the resonances.

2.2 Vacuum setup

At the time of restarting our experiment, we experienced an unexpected failure of the sealing valve giving access to the Rb atomic sources. On the one hand the accident caused a significant delay in the process of restarting the experiment. Still, as we shall discuss later on, it ultimately lead to an extra improvement in the quality of our quantum degenerate samples, thanks to the lower background pressure reached after the (otherwise unplanned) baking and pumping procedure.
After restoring the optimal working conditions, we went for a significant change in the vacuum system. Until then the experiment made use of separate pre-cooling chambers

for the two species, but our decision was to seal out of the setup what was formerly used as the Rb pre-cooling chamber, switching to a scheme with a single common chamber. The main reason behind this choice was that a visible layer of oxide had formed on the inside face of the Rb chamber's windows, as a consequence of the vacuum loss, causing a measurable reduction in the windows' transmittance.

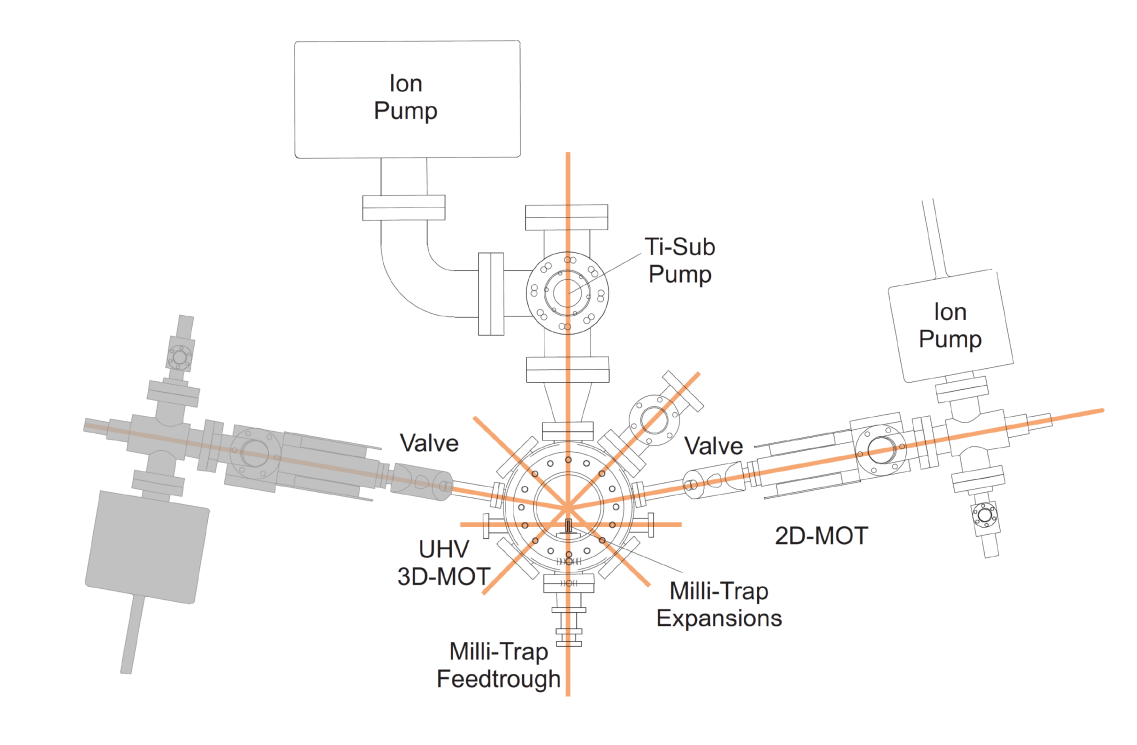

Figure 2.3: Top view of the full vacuum setup, including (highlighted in grey) the section which was sealed out of the experiment.

The vacuum setup is currently composed of two main chambers, the 2D-MOT chamber and the Main chamber.
The 2D-MOT chamber is outermost one, it hosts the atomic sources and the region where the pre-cooling stage takes place, in a bi-dimensional MOT (2DMOT). This first chamber has the shape of a rectangular parallelepiped, elongated towards the second chamber, with rectangular windows (BK7 glass, 80 × 35mm) taking up most of its four larger faces. Its metal structure is the only one of the system built in titanium, the metal which best matches the thermal expansion coefficient with the BK7 glass of its windows, which are directly glued onto the structure itself.
The apertures to the atomic sources lay on the side opposite to the Main chamber, next to the connection to a 20 l/s ion pump (*Varian Diode Cell 20 l/s*). The chamber's pressure was pumped down to about 10^{-9} mbar, a value which can increase up to two orders of magnitude when the atomic sources are turned on to give a sufficient flux of atoms.
The connection between the two chambers occurs through a flexible bellow (to relieve mechanical stress between them). The conductance is limited by a narrow channel

on the side of the 2D-MOT chamber, whose diameter of 1 mm and length of 10 mm are small enough to maintain a differential pressure among the two sections. This is, since a pressure below 10^{-10} mbar (Ultra-High Vacuum, UHV) must be kept in the Main chamber or the background gas collisions would prevent the formation of good quantum degenerate samples. A valve is mounted opposite to the 2D-MOT chamber, that can be shut to isolate the UHV region when changing the atomic sources.
The Main chamber was built from a single block of non-magnetic steel, in a cylindrical shape (height 90 mm, external diameter 190 mm). Eight apertures open on its side: seven of them provide horizontal optical access (for MOT, dipole and probe beams); another one is connected to a 55 l/s ion pump (*Varian Vac Ion Plus 55*) and a Ti sublimation pump. The two horizontal faces are almost entirely taken up by large viewports (130 mm diameter), maximizing the optical access along the vertical direction.

2.2.1 Atomic sources

A first difference of the new system from the past use is that both atomic sources must be sharing the same chamber.

For either of our species two kinds of sources can be typically used: vapor cells, where atoms are released by directly heating up a solid sample within an ampule, or dispensers. In the latter a tiny hollow metal wire, containing a stable alkali salt, sputters out the alkali species when sufficient heating is provided (by sending an electric current through the wire) to trigger chemical reactions inside the container. On our experiment both kinds of source were used at different times in the past, but this was while running with separate pre-cooling blocks.
With sources of rubidium and potassium sharing a single pre-cooling chamber, the use of vapor cells on both species stops being a viable option. In fact K is heated up more than Rb in normal operation, so it would most likely contaminate the source of this second species. On the other hand, if by any chance Rb contaminates K, the operating temperature of K would give an exceedingly high pressure for Rb.
Our solution fro the new system was to limit the use of a vapor cell only to potassium, using dispensers on rubidium instead. This exploits the fact that the temperature scale regulating the release from dispensers is not directly related to the thermodynamic properties of the alkali metal; the temperature dispensers are at, in normal running conditions, prevents the potassium deposits.
Natural abundance of ^{41}K is quite low (6.7%), to obtain a larger pressure we decided to use an enriched source, by having the ampule sample prepared from a suitably enriched salt. After heating up the ampule we could estimate the fraction of potassium-41 to be about 40% if the total, as measured from the relative amplitudes of saturated absorption lines from the different isotopes inside the pre-cooling chamber.

We note that other experiments on a rubidium-potassium mixture with a single source chamber use dispensers on both species (for instance [51]). This is not a convenient option for us, since our vacuum feed-through can only hold a few dispensers and the consequent need for frequent substitutions could eventually lead to a loss of vacuum

cleanliness (removal of the vacuum feed-through holding the dispensers cannot happen without exposing the whole 2D-MOT chamber to air).

2.3 Magnetic field sources

In cold atoms experiments, different kinds of magnetic fields are used. Homogeneous fields are primarily used for the interaction control and the compensation of external contributions, such as Earth's field itself. The most relevant application of inhomogeneous ones, instead, are magnetic traps.
In a magnetic trap the confinement is provided by the Zeeman shift experienced by the atom moving in a position dependent magnetic field $\vec{B}(\vec{r})$, which in the case of a field quantized along the z-axis results in a potential

$$U_{magn}(z) = -\vec{\mu}\cdot\vec{B} = \mu_B g_F m_F |B(z)|, \tag{2.1}$$

indicating with μ_B the Bohr magneton and with g_F the Landé factor. States for which $g_F m_F > 0$ are low-field seeking states, trapped by the magnetic field's minima.
The second equality in (2.1)is valid under the assumption that the field variation seen by the atom over time isn't faster than the Larmor precession frequency, that is

$$(1/B)\,|dB/dt| \ll \mu_B B/\hbar$$

so the atom's magnetic moment will always be aligned to $\vec{B}$.

In our setup two different magnetic traps are used, the Quadrupole Coils and the millitrap which we will briefly describe below, plus three other magnetic field sources. Two small rectangular coils are mounted on the horizontal faces of the 2D-MOT chamber and shaped around them, and a third larger one is placed orthogonally; all three coils are supplied by separate DC voltage generators and provide the magnetic field gradient and an horizontal bias, respectively, for the pre-cooling magneto-optical trap.
A set of two coils is wrapped around each of the Quadrupole Coils, it is used to provide a vertical bias field. A horizontal bias field, aligned with the millitrap axis, is instead provided by a large single square coil (*Shim Bias Coil*), overlapped to the external bias coil of the millitrap (see below) and shaped around it. Both the horizontal and vertical bias field's power supplies are remotely controlled by analog channels.

2.3.1 Quadrupole Coils

The first magnetic field source are the Quadrupole Coils, which we use in the initial laser cooling stage and in a short phase of purely magnetic trapping.
Each of the two circular coils (diameters: internal 9 cm, external 15 cm) is supported by an aluminum water-cooled plate, and both of them are held on a translation stage used to shift the position of the quadrupole field along the principal axis of our main vacuum chamber. They are connected to a specifically designed circuit (described in [52]) that allows to: turn on/off the field on a fast time-scale (on the order of ms) even

at high currents, using an IGBT transistor; switch the current configuration between Helmoltz and anti-Helmoltz, by selectively flipping the current direction in one of the coils via a set of relais.

Depending on the current configuration, two different generators are used as the coils' supply.
The principal supply is a *Agilent 6692A*, which we use to produce the actual quadrupole field (Anti-Helmoltz configuration). It delivers up to 6.6 kW, as 110 A/60 V, and its output is remotely controlled via a GPIB and an analog voltage. The quadrupole configuration is first employed with small currents and magnetic field gradients (≈16 Gauss/cm, with 4 A) during the initial laser cooling stage, inside the 3D Magneto-Optical Trap. Later on in the procedure, we turn on again the quadrupole field at a much larger current to magnetically confine the cold atoms during the movement towards the center of our main magnetic trap.
Then, there are two operations for which the coils are switched to produce a uniform field in the region of the atoms (Helmoltz configuration): during the internal state transfers between hyperfine states and when we need to tune the interspecies interactions through Feshbach resonances. In this configuration we use a different bipolar power supply (*Kepco BOP20-10M*, ±20 V/±10 A) for the coils.
The two power supplies are connected in parallel to the input of the MOSFET circuit, with high current diodes placed at each of the supplies' output to prevent back-actions (or cross-talk) among them; a precision resistor (*Isabellenhütte RUG-Z*, 0.5 Ω) is added in series to the cathode output of the Kepco supply, to allow for current sensing and stabilization.

2.3.2 The millitrap

The final cooling of our samples to quantum degeneracy takes place inside a peculiar kind of magnetic trap, called the *millimetric-trap* or *millitrap*, whose schematic depiction is reported in Fig. 2.4.
Similarly to the micro-chip based magnetic traps used in other experiments, it is held inside the vacuum system, but unlike them it is macroscopic in size and can be treated by all means as a standard macroscopic trap. It combines the advantages of having a magnetic field source very close to the atoms, so strongly confining fields are obtained with a low power consumption (<10 W), with the possibility to have optical access along all three spatial directions.
The main element of the millitrap structure is a hollow copper cylinder (length: 17 mm; diameters: internal 5 mm, external 9 mm) with two cut sections along the longitudinal direction. This part is mounted onto a ceramic chip with two circular copper traces, ensuring an electric contact all the way to outside of the vacuum chamber. Two concentric external coils, added on the outside of the vacuum system (4 cm away from the magnetic field zero), provide a bias field to the structure.
This geometry produces a field distribution equivalent to that of a standard Ioffe-Pritchard trap: it can be expanded close to the minimum as a harmonic potential,

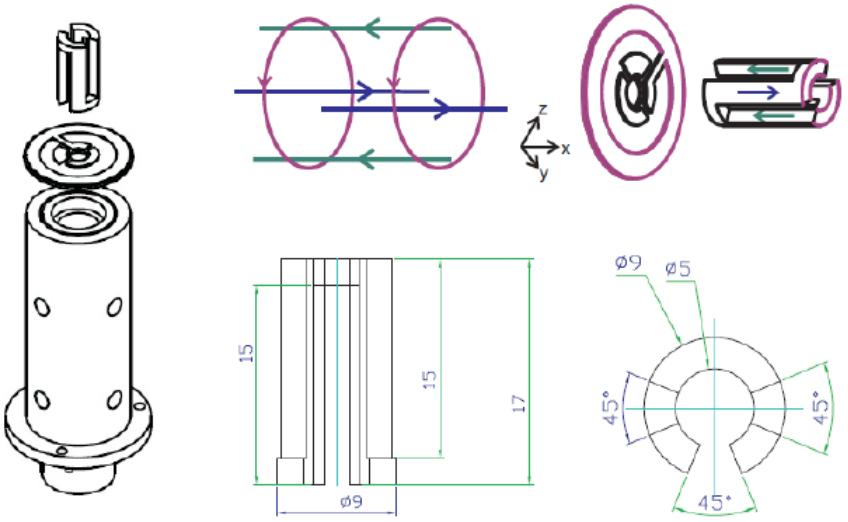

Figure 2.4: *Left hand side:* Disassembled view of the millitrap. *Center and right-hand side:* Details on the millitrap mount inside the vacuum; Correspondence of the current flow directions between the millitrap and a standard Ioffe-Pritchard configuration.

in this case axially symmetric around the cylinder axis, plugged with an offset. In polar coordinates it yields

$$\left|B(z,\rho)\right| \simeq \left(b_0 + b_0'\right) + \left(\frac{b_2}{2}\right) z^2 + \left(\frac{b_1^2}{2(b_0 + b_0')}\right) \rho^2, \tag{2.2}$$

which depends upon the multipole expansion coefficients b_n of order n for the millitrap and that of the external bias b_0'. They in turn will be set by the supplied current.
During the magnetic confinement we provide the millitrap with 70 A , producing a ≈6.3 G bias and a harmonic profile around the minimum with frequencies:

- $\omega_{ax} \approx 2\pi \cdot 16$ Hz in the axial direction;
- $\omega_{\perp} \approx 2\pi \cdot 200$ Hz in the transverse directions.

The current for the magnetic trap comes from a *Agilent 6671* (0-8 V, 0-220 A), whose setting values are remotely controlled by GPIB and analog signals. In the experiment we keep it at 70 A during the magnetic confinement; remote fast switching on and off is possible thanks to dedicated MOSFET circuit (controlled via a TTL signal), similar to that of the Quadrupole Coils, which allows to fully extinguish the millitrap current in ≈1 ms.
Finally, we must note that the optical access granted by the apertures in the millitrap is enough for the laser trapping beams and the detection ones, but too small for any efficient laser cooling[1]. This is why we need to perform all laser cooling stages, prior

[1] For instance, in a 3D-MOT the capture velocity range of incoming atoms is proportional to the size of the beams and it would be far too narrow for diameters of a few mm.

Table 2.1: List of the AOMs on the Optics' Table, with numbers referenced to the labels in Fig. 2.5.

1	Rb Repumper Opt. Pumping + Probe
2	Rb Repumper TA Injection
3	Rb 3D-MOT
4	Rb Push
5	Rb 2D-MOT
6	Rb Cooler Opt. Pumping
7	Rb Cooler Probe
8	Rb Spectroscopy
9	K Spectroscopy
10	K Cooler Switch
11	K Repumper
12	K Push
13	K Cooler 2D-MOT
14	K Repumper 2D-MOT
15	K Repumper Switch
16	K Probe
17	K Opt. Pumping
18	K 3D-MOT

to the magnetic trapping, in the center region of the Main Chamber (onto which the atomic beams from the pre-cooling chamber are pointing); then we subsequently move the atomic samples into the millitrap region, during a short termed magnetic trapping provided by the Quadrupole Coils, as they shift along the Main Chamber axis thanks to the translation stage they were mounted on.

2.4 The new optical setup

On the Optics' Table, the beams from different laser sources are split in separate arms, undergoing different frequency shifts provided by Acusto-Optical Modulators (AOMs), that are finally fiber launched to the the experiment (via polarization-maintaining optical fibers). More specifically, in our case there are five distinct lights we need to produce from each source, which we name after the stage of the experiment they are used in: 2DMOT, 3DMOT, Push, Optical Pumping and Probe beams respectively (whose roles will be discussed in the Chapter devoted to the experimental procedure).
Before this work, the original optics' setup had become a limiting factor for many aspects of the experiment; its main flaws being the poor alignment stability and a generally low supply of optical power due to its aging sources, matched with a scheme which made local upgrades extremely difficult. This lead us to the choice of a full reconstruction of the Optics' Table, with new sources and a smarter design, finally resulting in the current optical setup depicted with (relatively faithful) detail in Fig. 2.5. This section explains its

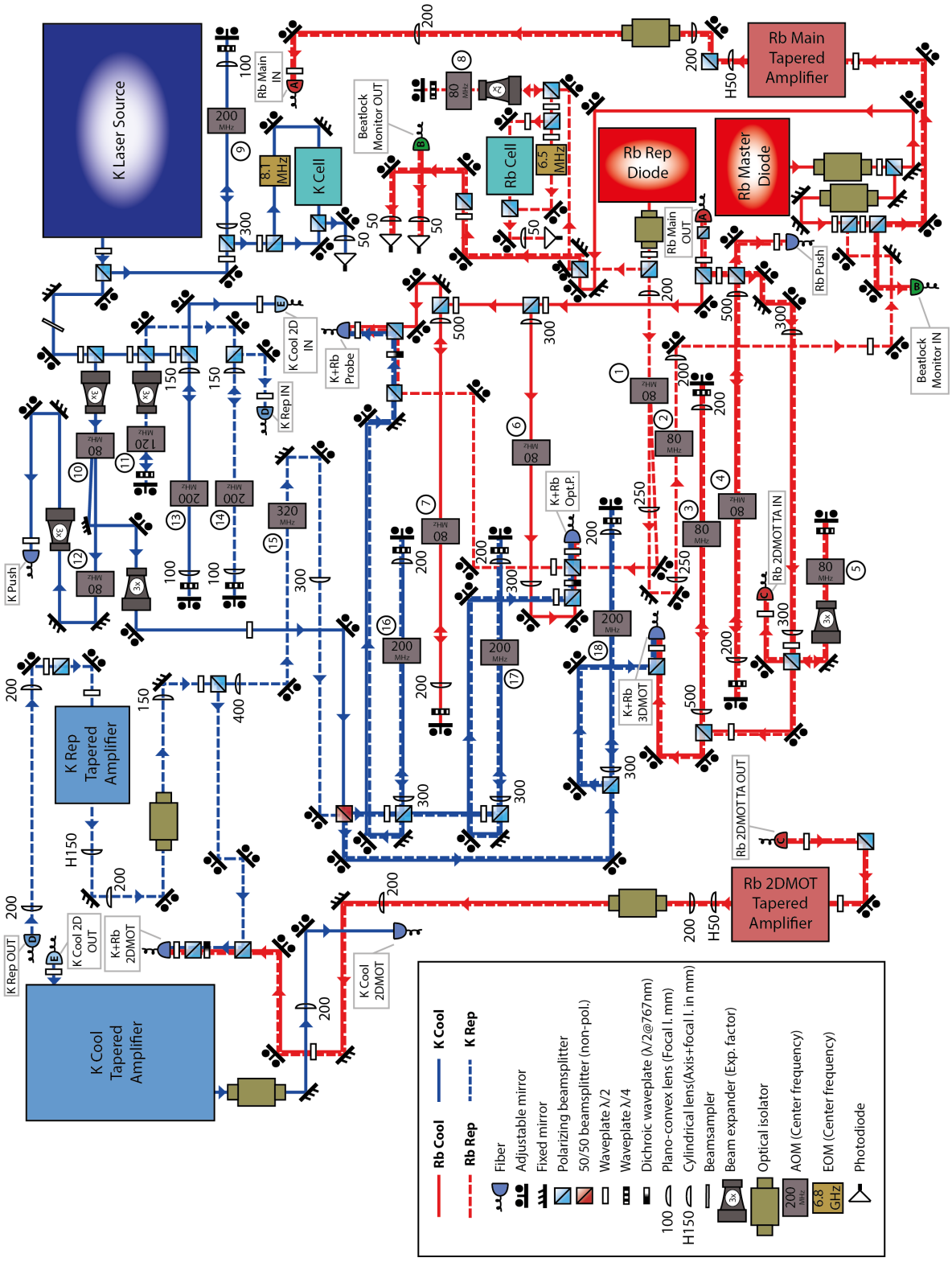

Figure 2.5: Detailed scheme of the optical setup. See the legend for further details.

main features, technical solutions, and the ideas behind them.

2.4.1 Designing choices

In the designing process, our first aim was to get a major increase of optical powers in the MOTs of both species, which we achieved by adding an extra optical amplifier (Tapered Amplifier, or TA) for the amplification of each species' 2D-MOT light (that being the most power-hungry step of our experimental procedure).

On top of the power issue, we also needed an enhanced day-to-day stability and ease of use of the optical system.
For this objective's sake we pursued the tasks of:

- *Compactness on the optics' table*, saving up space for extra components;
- *Reduction of the optical paths' length and choice of stable adjustable optics*, to minimize all pointing instabilities;
- *Ease of realignment and future upgrade*, even in case of substitution of a main source, for instance.

In our mixture experiment most of the beams shined on the atoms must carry four different wavelengths, namely that of cooling and repumping transitions for both species: the need to produce and combine four different laser beams in most of the fibers was causing of a great deal of complexity in the previous setup. This was also resulting in more room being taken up on the optical table and more power being wasted after each combination on a polarizing beam-splitter cube (PBS), due to imperfect simultaneous setting of the polarization for the lights at different wavelengths of 780 nm and 767 nm (partly observable even where using suitable dichroic waveplates).
Our solution to this issue was to avoid using separate parallel paths, by overlapping the cooling and repumping lights of each species as early as possible, hence letting them travel through a single common AOM instead of two separate ones. This configuration strongly reduces the length of optical paths needed, the number of required AOMs and subsequently the combining optics afterwards. More in specific, we tested and implemented different solutions for the rubidium and potassium lights, due to the different nature of their level structure and laser sources.

Potassium-41 has an extremely small cooler-repumper (hyperfine) splitting of 254 MHz, so we can use a single laser source and produce the second frequency with a 200 MHz AOM in double pass scheme, but we need similar powers of both lights.
The laser is frequency-stabilized by saturation spectroscopy near resonance, then a small fraction of its output goes to the AOM producing the repumper light, that eventually injects a second dedicated TA generating the power for the potassium repumper.
In order to get large powers at both frequencies on potassium we make use of two extra TAs, with one of them solely dedicated to the production of 2D-MOT light on the cooling transition. Then, with the only exception of 2D-MOT beams, the two high power cooling and repumping lights (from the *Toptica TA pro* and the K Repumper TA, respectively)

are overlapped on a single non-polarizing cube (50% transmission/50% reflection) to allow for them to go through the same double pass AOMs and fibers.

Rubidium-87 has a much larger hyperfine splitting than potassium-41, that would require more complex solutions to be produced from a single laser source, but because of this it is also asking for much smaller repumping light powers.
For the production of Rb cooling and repumping lights we use two separate semiconductor laser diodes. In the scheme we implemented on Rb we spatially overlap the two diodes' outputs right before injecting the first TA (referred to as *Rb Main TA* hereon). Note that, after getting combined on a PBS, the two beams are orthogonally polarized with each other, while the amplifier only works on a given liner polarization. We use a second PBS in the line to only let fractions of each beam with proper identical polarizations into the Rb Main TA injection.
What makes this a viable option is that an extremely small amount of repumping light is needed to get the desired cooling/repumping ratio of powers ($P_{Rep}/P_{Cool} \approx 0.1$) at the TA output: in fact, a good majority of the repumper power goes wasted on the last PBS, while most of the cooling one goes through. Such condition grants us that the cooling light alone will be enough to saturate the TA injection. This is a crucial point at the times of the experimental procedure (optical pumping and probing) where we must be able to selectively shine the cooling light on the atoms, while still keeping the TA in a stable running condition.

A further reduction of the optical arms' length was possible with the use of compact telescopes as adaptive optics on several of the AOMs set up in a double-pass configuration. Unlike the usually favorable *cat's eye configuration*, which allows to exploit a wider frequency bandwidth without physical misalignment of the beam this solution, the use of these compact optics requires a realignment of the double-pass when RF frequency is changed; so we limited this solution solely to the AOMs whose frequency isn't changed during the experimental procedure.
Finally, as a results of the designing choices we just introduced, we were able to reduce the extension of the optical setup by one third, while still getting out larger powers wherever needed.

Concerning the improvements on the ease of use, our solution was to split the scheme into different areas, mostly through the use of optical fibers connecting different points on the table, in such a way that any change or misalignment only affects a smaller subsection of the scheme. With sufficient planning it was also possible to fold the system in such a way that even major changes could stay localized in a restricted area of the table surface, provided that the future scheme fits into the same space.
For instance, the use of optical fibers is extremely efficient right at the input of all three TAs which aren't directly injected by laser diodes. This positioning grants us a good degree of mutual independence among the various sections (before and after each fiber), while minimizing the power loss due to imperfect fiber coupling (the main disadvantage in the use of fibers instead of free-running beams), since fairly low powers are needed on the TA injection side.

As a final remark, we must stress another advantage brought in by the new setup:

for both Rb and K we now have significant extra power and room on the optical table available, that was used for the production of optical beams to be employed in Raman hyperfine transfers (via π-pulses) on both species; in the past, we were only able to produce pi-pulses on K with a separate setup using our Ti:Sapphire laser as a source, whereas now it can be employed up for other purposes.

2.4.2 Laser sources and laser locks

The laser sources for both species are a combination of one (or more than one) semiconductor laser diode and a Tapered Amplifier (TA) set up in a MOPA (Master oscillator power amplifier) scheme. As anticipated in the previous section, the lockpoint and the independent frequency shift of each source is chosen in such a way that the desired relative detuning between cooling and repumping light(for each species) is obtained *before* they are combined and sent through shared AOMs. In the following pages we report the detailed way in which this is done and how the frequencies are handled in the new setup; Figures 2.5 and 2.6 can be used for reference. As a foreword, we note that we will refer to all lights and beams classifying them as "cooling" and "repumping", only (even if some of them are not actually used for the laser cooling).

Rubidium

The sources for rubidium are two diode laser setups: a commercial one for the cooler (*Toptica DL pro*) and a homemade one for the repumper, with its semiconductor diode (*Sharp GH0781JA2C*, max 120 mW nominal output power at 25°C) mounted in an ECDL (extended cavity diode laser) system, with Littrow configuration[2]. In standard running conditions we get about 40-50 mW of optical power at each source's output; immediately after the optical isolators, a first small fraction of this power (2-4 mW) is taken on a PBS to be used for the locks of the two lasers.

The repumping source is locked ≈77 MHz below the relative transition ($|F=1\rangle \rightarrow |F'=2\rangle$). More precisely, we lock it 153 MHz above the $|F=1\rangle \rightarrow |F'=0\rangle$ transition, after a frequency shift provided by a double pass AOM (*Rb Spectroscopy AOM*).
The error signal for the lock is produced by a standard lock-in amplifier from the Doppler-free absorption profile of the $|F=1\rangle \rightarrow |F'=0\rangle$ line, taken on a spectroscopy cell after the Rb Spectroscopy AOM. We use a modulation transfer scheme where the pump beam alone is modulated by an Electro-Optical Modulator (EOM) (*QBig EO-F7L*, resonant at 6.54 MHz). The active stabilization for the lock is provided by a standard P-I servo amplifier.
On the path of the repumping beam there are two different AOMs, which are never turned on at same time during the experimental procedure. During the actual laser cooling stages, only the second AOM (*Rb Ta Injection AOM*) is turned on, shifting down the beam frequency by ≈-71 MHz and sending a small fraction of the repumping light into the Rb Main TA (together with the cooling one).

[2]There the feedback is provided by a UV diffraction grating, which was preferred over an IR one in order to maximize the power output (at the cost of a smaller feedback reflection for stabilization).

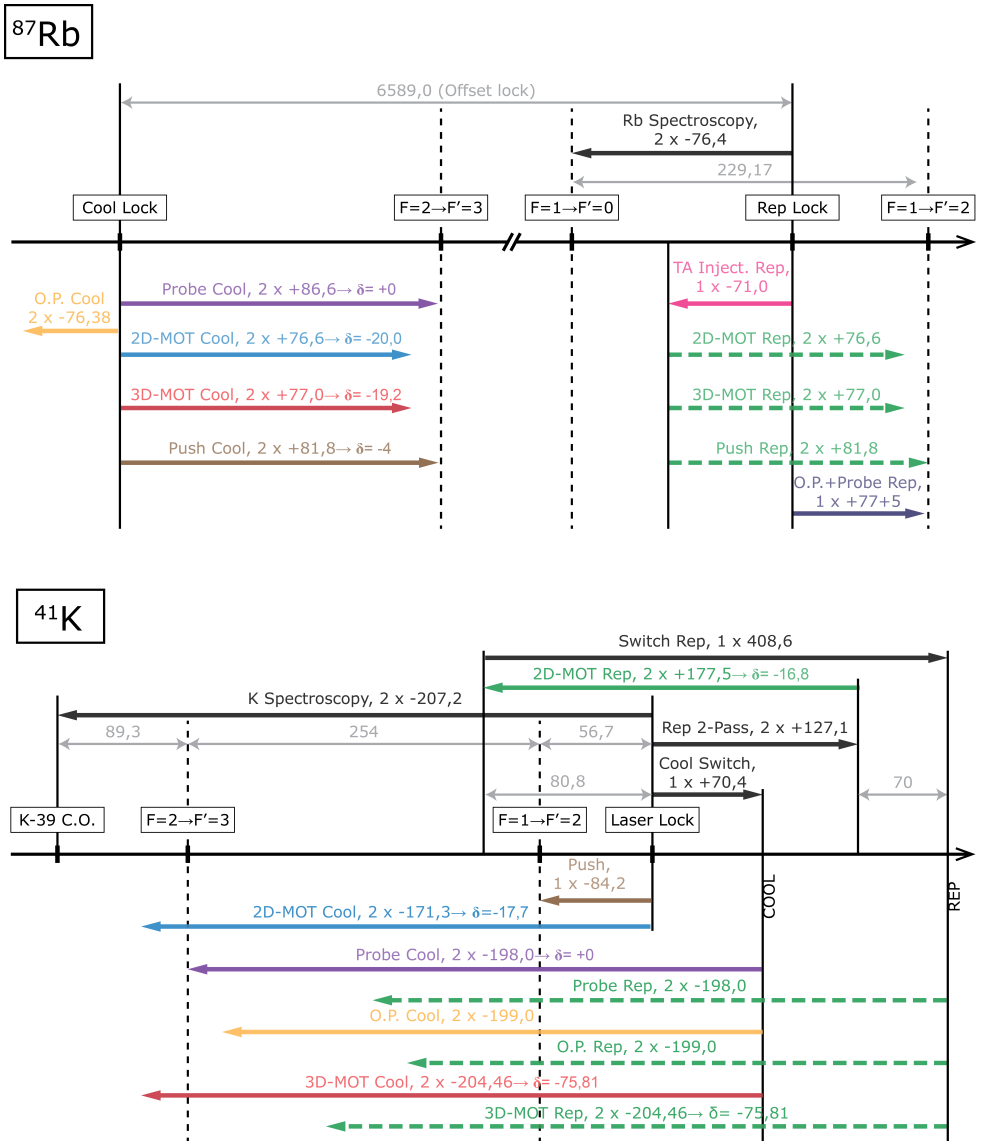

Figure 2.6: Detailed scheme of lock frequencies and AOM frequency shifts (in MHz) for the different beams of Rb and K in our experiment; for each beam, δ indicates the detuning in MHz from its reference transition. Dashed lines are used to indicate the frequency shifts of the repumping beams which are produced by a shared AOM with the relative cooling beam.

The first AOM in the line (*Rb Repumper AOM*) instead is only active in the stages where similar powers are needed for both cooling and repumping lights (namely, when laser light isn't used for cooling purposes). The beam in this configuration is diverted from the other path, getting a ≈+77 MHz shift as the +1 diffraction order of the AOM, to directly inject the fibers of the Optical Pumping and Probe beams.
In this second configuration we prevent the repumping from injecting the TA by simultaneously turning off the RF amplitude on the TA Inject AOM and and misaligning the fiber injection of the diffracted beam by shifting the AOM frequency.

The cooling source is offset-locked from the repumping one, at a frequency which can be changed during the experimental procedure. Its locking scheme, implemented in the re-building of the experiment, is extensively described and characterized in the following Chapter. It only requires to draw a few mW from the output, and combine them with a suitable amount of repumping light on a fast photodiode.
The rest of the output power after the isolators is overlapped with the repumping light and a fraction of both injects the Rb Main TA, after the PBS for the polarization matching mentioned in the previous section. A $\lambda/2$ waveplate before this cube sets the relative ratio of cooling versus repumping light feeding the amplifier.
This first TA was home-built using a newly designed mount (described in the Appendices), holding the bare tapered chip on a C-mount (*EagleYard EYP-TPA0780-020000006-CMT04-0000*). It provides a power of about 2.0 W at 2.5 A, when optimally injected with 20 mW. The output beam is directly fiber coupled into a suitably chosen single-mode polarization maintaining fiber (*Schafter-Kirchhoff FC-APC End-Cap fibers*), able to handle the maximum power of 2.5 W we can send at its input. Using a fiber here has the first advantage of providing an initial separation of the optical setup into blocks, decoupling the alignment duties among the two sections. Secondly, it acts as a spatial-mode cleaning element, making the efficiency of the following optical components (AOMs and other fibers) independent on the TA output mode; the latter could poorly overlap with the optimal TEM_{00} and possibly be subject to long term modifications over the course of the chip lifetime. These advantages come at the well-known cost of a power loss (up to a 45%) at the fiber coupling, given by the imperfect mode matching of the TA output and the single-mode fiber; in our case, though, such limitation is superseded by the large powers that our TA chip provides.

The fiber after the Main TA sends its output to a second block of optics on the table, where the beam is split, frequency shifted and eventually fiber launched to produce the other beams used in the experiment. (Note that the Probe and Optical Pumping branches in Fig. 2.5 are only when no repumping light injects the TA, being them meant to provide the cooling component only.)
The 2D-MOT fiber is the only one which doesn't go directly to the Vacuum Table, providing instead the injection to the other Rb TA (*Rb 2D-MOT TA*). This second one is an exact copy of the Main TA, solely dedicated to the amplification of the light for the 2D-MOT stage: with a minimum of 20 mW injection power it grant us up to 1 W of optical power

at the fiber output on the Vacuum Table.

Potassium

On the potassium we use a commercial MOPA setup (*Toptica TA pro*) as the unique laser source, providing a total output power of 1.3 W to the system. The laser is locked via a saturated absorption spectroscopy setup similar to the one just described for the rubidium repumper source, with a lockpoint set about 56 MHz above the ^{41}K repumping transition. More precisely, we lock the laser on the cross-over line of ^{39}K, after a 400 MHz frequency shift provided by a double-pass AOM (*K Spectroscopy AOM*). In fact, the cross-over has the largest amplitude among the features of the sub-Doppler spectroscopy profile from our vapor cell, due to the bigger natural abundance of ^{39}K over the two other isotopes.

The MOPA emission gets split into three branches. Most of the power goes into the first one which provides, after a single-pass AOM (*K Cooler Switch AOM*), the K cooling light for all stages of the experiment (except from the 2DMOT) and it is sent to straight to the 50/50 non-polarizing beam splitter used for the overlap with the repumping light. Both the other (low power) branches instead, after suitable frequency shifts from double-pass AOMs, are fiber coupled and directly inject the two external TAs of K.
A larger power one (an old commercial setup refurbished by Toptica, containing a chip: *TA-0765-1500-4*, 1.5 W max output) amplifies the light used for the cooling light of K 2DMOT, its output being directly fiber coupled to the associated fiber. A second, homemade one (containing a chip by *Eagleyard EYP-TPA-0765-01500-3006-CMT03-0000*, with max 1,5 W emission at 767 nm) is fed by the light which is frequency shifted towards the repumping transition, and it sources the power for all the repumping beams.

Part of the output from the *K Repumper TA* is immediately fiber coupled as the repumping component of the 2DMOT, while the rest goes through a high frequency single-pass AOM (*K Repumper Switch AOM*) to be combined with the cooling light on the non-polarizing beam splitter.

Finally we note that mechanical beam shutters were added before each of the fibers to the Vacuum Table, to prevent any fiber coupled light from reaching the atoms when it is not supposed to.

2.4.3 The dipole lasers

We use two different sources at 1064 nm wavelength to generate the beams of our crossed-dipole trap and optical lattice. Both of them are placed on the Vacuum table, together with their full optics' setups.
The source for the optical trap is a fiber coupled laser (*IPG YLR-20-1064-LP-SF*), whose output in current running conditions is about 9 W. Its optical setup has been preserved during the renewal of the experiment: the laser emission is split in two parallel arms, corresponding to the dipole trap beams, where the beams travel through an AOM in single-pass configuration and inject a high-power (armored) optical fiber (*Crystal Technologies LMA-PM-15*, polarization maintaining). The output of each fiber is sent to

the Main Chamber after an aspheric lens, which sets the beam focus on the atoms. Both optical trap beams have a ≈80 μm waist on the atoms' position, and they are aligned in the horizontal plane: one enters the Main Chamber along the millitrap axis (*axial beam*), the other one from the small viewports on the millitrap side (*radial beam*). The maximum power available for a single trap beam is about 1 W, in the case of balanced powers among the two: this corresponds to a limit temperature of ~ 1.5 μK for the ^{87}Rb atoms to be captured and maintained by our crossed-dipole trap.
At the fibers' output a small fraction of the optical power is taken off a back-side polished mirror and sent on a photodiode, for the trap stabilization: the signal corresponding to each beam is sent to a PID servo amplifier, acting on the AOM driver of each beam. We use dual-frequency drivers to tune the frequency and amplitude of the trap AOMs, which allow to rapidly switch on/off the dipole beams while always keeping a RF active on the modulators, keeping them warmed up.

The optical lattice light is provided by a commercial 21 W laser (*Innolight Mephisto*). In the previous version the optical setup for the lattice, the laser output (after being split into three separate arms) was directly sent to the Main Chamber along an extended optical path, and the beams underwent multiple reflections from adjustable optics. A new compact setup was built, with the same scheme as the optical trap one, to improve the mechanical stability and avoid long optical arms; in the current version, after the laser output is split in three arms to produce each direction of the cubic lattice, the beams go through separate AOMs and fibers (*Schafter-Kirchhoff FC-APC End-Cap fibers*). On the output side of each of the latter, pointing instabilities were further reduced by using the minimum number of adjustable optics' mounts: two before the vacuum chamber, to allow for the path alignment, and one for the retro-reflection mirror. The power stabilization of every single beam is again provided by separate PID servo amplifiers, with error signals derived from photodiode voltages, whose feed-back controls the amplitude and frequency of the respective AOM RF.
The wavelength and the counterpropagating geometry define the lattice periodicity of $d = \lambda_L/2 = 532$ nm, while the waist of the beams on the sample region is ≈ 150 μm. At the maximum power of about 2 W available on each of the lattice beams, for rubidium we can produce a lattice depth of at least $60E_R$ on every single direction.

Chapter 3

The Rubidium offset lock

In an offset lock, the laser emission is stabilized a fixed distance away in frequency from another reference point; it represents a fairly simple solution for an easier and faster tuning of the laser lockpoint, which best matched our design for a compact optical scheme. In fact, we can now fully exploit the large lock bandwidth and the possibility to change the laser frequency during the experimental procedure with unprecedented bandwidth and speed. This we shall show into detail during the following sections, discussing the lock electronics and the advantages of using a combination of a spectroscopy lock and an offset lock for our Rb sources, over the previous solution of a spectroscopy lock on both lasers.

3.1 Method of error signal generation

The offset lock stabilizes the separation between our Rb cooling and repumping laser diodes via their relative beatnote frequency, on an error signal generated by a suitable coaxial delay line. A first example of this scheme can be found in [53, 54].
More specifically, the error signal is produced in three steps: the beatnote production and detection; the signal downconversion; the actual error signal generation.

When the emissions from two different lasers are overlapped, the intensity of the resulting field will behave in time as

$$I \propto \left| \hat{\varepsilon} E_1 e^{i2\pi\nu_1 t} + \hat{\varepsilon} E_2 e^{i2\pi\nu_2 t} \right|^2 = {E_1}^2 + {E_2}^2 + 2E_1 E_2 \cos(2\pi\Delta\nu t) \tag{3.1}$$

where E_i and ν_i are the amplitudes and frequencies of each laser beam, respectively, and the polarization $\hat{\varepsilon}$ is the same for the two beams. The frequency difference is $\Delta\nu = |\nu_2 - \nu_1|$: the overall intensity shows a modulation at the frequency difference (beatnote). When the beams are sent on a photodiode, the corresponding oscillating signal at $\Delta\nu$ will be detected (provided that the photodiode can follow it) and the DC component easily filtered out.
Still, in most of the applications the beatnote frequency is too high for standard electronic components and a downconversion below the GHz range is needed. An easy way

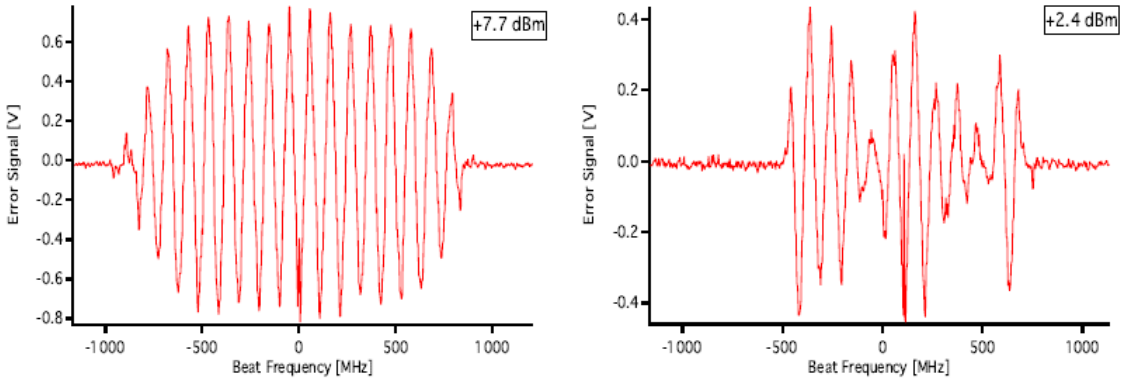

Figure 3.1: Example of the error signal obtained by scanning the laser frequency on our system, with/without saturation of mixer/phase detector. The left hand side shows the optimal shape (with little or no modulation of the sinusoid aside from the envelope of phase detector bandwidth), given an input power of 7.7 dBm into the error signal production circuit (splitter+delay line+phase-detector). On the right hand side we see instead what happens when the same power is lowered to 2.4 dBm. Both traces were taken for a delay line length of 2 m.

to do it is by combining the beatnote signal on a mixer with a second one at a frequency ν_{REF} of similar magnitude, taking from the mixer output

$$\cos(2\pi\nu_{REF}t)\cos(2\pi\Delta\nu t) = \frac{1}{2}\left[\cos(2\pi(\nu_{REF}-\Delta\nu)t) + \cos(2\pi(\nu_{REF}+\Delta\nu)t)\right] \quad (3.2)$$

only the difference-frequency component (while the sum-frequency signal is generally filtered out by the mixer itself).
At this stage the actual error signal is produced by splitting the line into parallel sections, one of which has a longer length of coaxial cable serving as a delay line, before recombining them on a phase detector. The delay time accumulated along such cable is effectively frequency-independent (about 5 ns per meter), so the relative phase shift Φ seen after recombination will be only a function of the beatnote frequency for any given cable length. The resulting voltage at the phase detector output will be proportional to

$$\cos(\Phi) = \cos(2\pi(\Delta\nu - \nu_{REF})\tau) \quad (3.3)$$

for a delay time τ, provided that the other output at frequency $(\Delta\nu + \nu_{REF})$ gets filtered out (as it's usually done by the phase detector). Every zero crossing of the sinusoid can be used as a locking point.
When dealing with a real system though, two remarks must be made about this result. First, one has to take into account the limited bandwidth of the circuit elements: the actual error signal will be a sinusoid convolved with the bandwidth envelope, mostly that of the final phase-detector, limiting the number of available zeroes to lock to. The actual error signal is shown on the left hand side of Fig. 3.1.
Second, the mixer and the phase-detector will require a minimum power level at their inputs to guarantee a stable signal at their output, namely, independent of input power

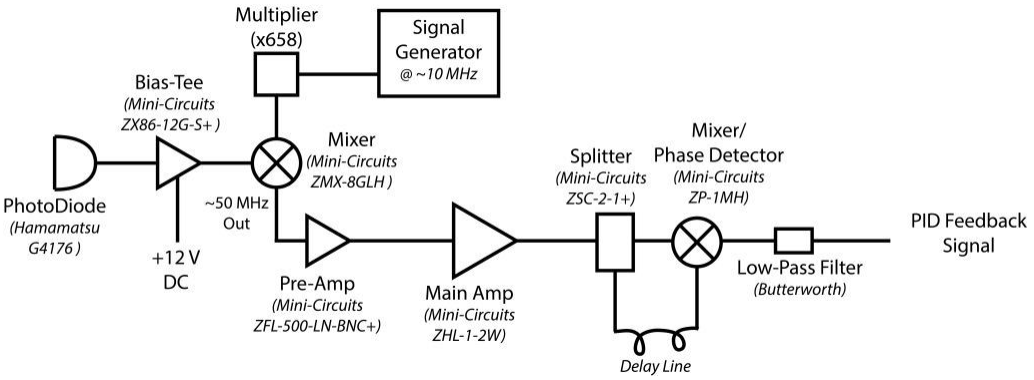

Figure 3.2: Schematic depiction of the Rb offset lock scheme.

fluctuations. Working away from this "saturation" will otherwise result in time dependent and/or irregular shapes of the sinusoid which will cause an unstable lockpoint (e.g., right hand side of Fig. 3.1). Because of this, typically after the downconversion, an amplification step is added, in order to get an overall better signal-to-noise ratio and to sit above the saturation power level in the forthcoming electronics.
Going back to (3.3), it is clear that for a given scan amplitude on the laser frequency the signal will depend on the changes of:

- *Reference signal frequency:* its variation rigidly shifts the position of the whole sinusoid, hence that of any lockpoint;

- *Delay line length:* increasing the cable length "squeezes" the sinusoid, effectively acting on three parameters at once. In fact, a larger number of lockpoints will be available (since the bandwidth envelope is independent of the delay line) and their zero-crossing slope will increase too, but at the expense of a smaller tuning range between the different zeroes.

So, while the reference signal frequency always remains a valuable active parameter, it is still important to correctly choose a delay line length which allows the desired range on it without weakening too much the lock strength.

3.2 Our setup: components and running conditions

A schematic depiction of our setup is shown in Fig. 3.2, for reference. Here we will proceed to describe its components and overall features.

Photodiode: As anticipated, the frequency separation between ^{87}Rb cooling and repumping transitions lies in the GHz range (6568 MHz) and it requires a fast response detector for the beatnote. We use a *Hamamatsu G4176* photodiode, with rise/fall time of 30 ps.
Assuming same polarization for both beams, a minimum of 1 mW optical power is

needed on the photodiode to detect a visible beatnote signal (S/N>2), with little dependence on how the power is split among the two beams; we normally run at about 2 mW total power, where the beatnote amplitude starts to more weakly depend on optical power and we are still safely away from the photodiode's damage threshold of 4 mW.

Bias-Tee: The photodiode is directly connected to a bias-tee (*Mini-Circuits ZX86-12G-S+*) which serves the double purpose of supplying the driving voltage (12 V DC, from batteries) to the latter, and offsetting for any DC component in the output signal, letting only the oscillating contribution through.

Downconversion and Reference Signal: It occurs on a mixer (*Mini-Circuits ZMX-8GLH*) of 7dB saturation level, whose local oscillator (LO) input is provided by a VCO phase-locked to the 685th harmonic of a radio-frequency signal at 9.7 MHz from a signal generator (*Agilent 33220A*). The latter can be remotely controlled with an analog voltage channel, rapidly changing the lockpoint even during the experiment. The LO power level is sufficient to saturate the mixer, so the weak $\approx$ 6 GHz signal from the photodiode is not amplified.
Once more, at the mixer output, the filtering of the higher (sum) frequency component automatically occurs due to the limited bandwidth of the electronics, so we can safely restrict the discussion to the signal at a few hundreds of MHz.

Amplification: The mixed output has low power (about -40 dBm), which we increase up to a few dBs with two stages of amplification (*Mini-Circuits ZFL-500-LN-BNC+*, 24 dB gain, and *Mini-Circuits ZHL-1-2W*, 33 dB gain). More specifically, we could see that the final section of the circuit requires an input power above 7 dBm in order to saturate all its parts, as can be seen in Fig. 3.1.

Error signal production and filtering: After the amplifiers we have the splitter (*Mini-Circuits ZSC-2-1+*): its first output goes to the delay line, whereas the other one is connected straight to a second mixer (*Mini-Circuits ZP-1MH*) where it gets recombined with the delay line output. Finally, before sending the error signal to the servo stabilization circuit, we employ a low-pass filter (Butterworth type 3 filter, cut-off frequency 80 kHz) to suppress the sum-frequency output of the mixer/phase-detector, as well as any other high frequency noise from the system.

3.3 Lock characterization and linewidth measurement

The characterization of the offset lock reported in this Chapter was performed stabilizing the repumper to the cooling laser. Even though the stabilization is currently reversed, i.e. the cooling laser is locked to rempuper, we could verify that the general conclusions hold valid nonetheless.
As part of the loop circuit used for the frequency locking, the error signal output from the phase-detector is sent to a proportional-integral (P-I) servo controller, handling for the feedback on the laser. The controller output voltage is used to drive the current of the diode and the voltage on the piezoelectric transducer, that controls the extended cavity length by pushing on its diffraction grating. The driving signal is actually split inside the laser driver between the piezo and current components, spectrally restricted

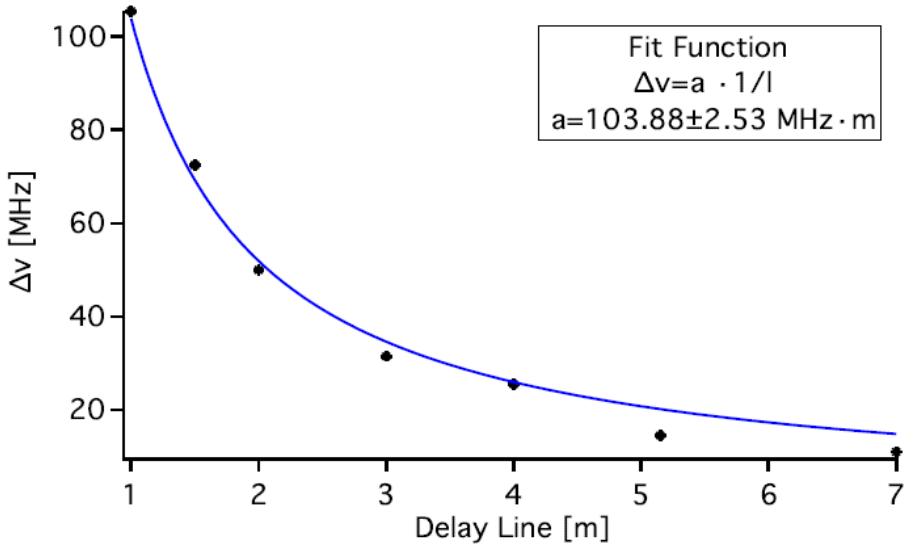

Figure 3.3: Frequency separation $\Delta\nu_0$ of two zeroes (lockpoints) versus length l of the delay line. Experimental points are overlapped with a fit of $\Delta\nu_0 = a/l$.

to a suitable range by filters, since the two have to respond at different frequencies. The low frequencies up to a few hundreds of Hz are handled by the piezo: we could measure a cut-off around 400 Hz on the one used for the characterization, but due to the filter inside the laser diode driver the actual feedback of the piezo was limited by a cut-off at 90 Hz. After establishing a first lock, we characterized its quality through the error signal for different delay lines. In Fig. 3.3 the measured frequency distance $\Delta\nu_0$ between two lockpoints (zeroes) is plotted versus the corresponding cable length l. The fitting curve a/l estimate for the parameter $a = c/2n$ is in good agreement with the expected value for the refraction index n reported in the cable specifics ($n = 1.44$).
We could classify the lengths in three ranges, by the quality of the lock they produced after optimizing the P-I gains in each case. Cables shorter than 2 m gave a zero-crossing slope small enough to make the lock weak against small fluctuations. Cable lengths larger than 4 m, instead, made it easier to to jump on different lockpoints or to lose the lock altogether in the case of sudden drifts (e.g. due to mechanical shocks on the optical table); they also gave a worse signal-to-noise ratio (S/N), most likely due to a larger pick-up noise contribution which was hard to shield completely. Finally, in the range from 2 m to 4 m, no significant variation of the S/N could be seen, so we decided to use a 2 m delay line as a best compromise between S/N and range of accessible frequencies.

To quantitatively measure the effect of the lock we calculated the Frequency-Noise Power Spectral Density (FNPSD) of the error signal from its noise spectrum, in the intervals: from 1 kHz to 10 kHz, from 10 kHz to 100 kHz, from 100 kHz to 1.1 MHz[1]. Note that for these measurement a 15 m delay line was used, giving a frequency tuning

[1]Above 10 kHz we could directly acquire the noise spectrum on our spectrum analyzer (*Advantest R3162*). Since the smaller frequencies were outside of the operating range of the latter, we obtained spectrum below 10 kHz as the Fourier transform from an error signal trace on a oscilloscope.

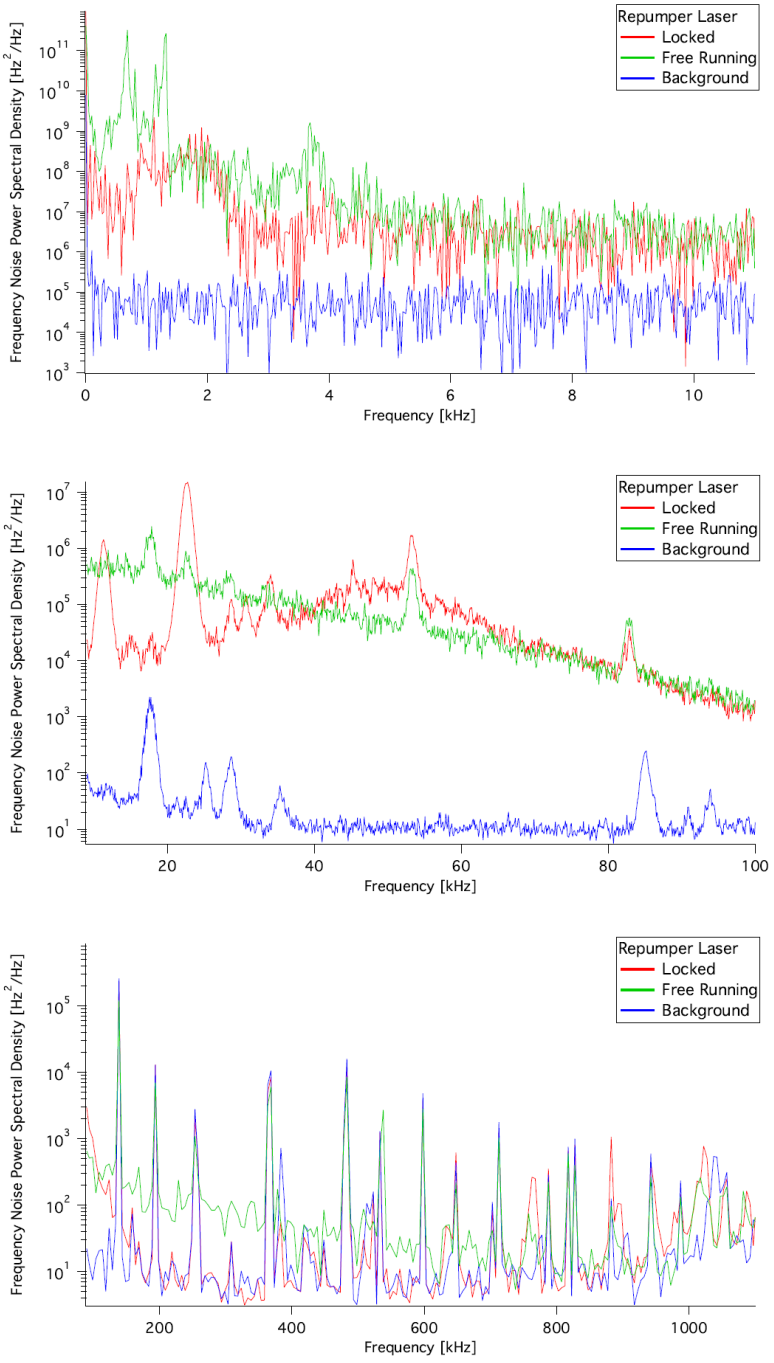

Figure 3.4: FNPSD of the offset lock error signal. Curves in the two top plots are calculated directly from the acquisitions of the spectrum analyzer (ResolutionBandWidth=1 kHz, VideoBandWidth=100 Hz). The bottom one, instead, from the Fourier transforms of oscilloscope traces. (A 15 m delay line was used in these measurements.)

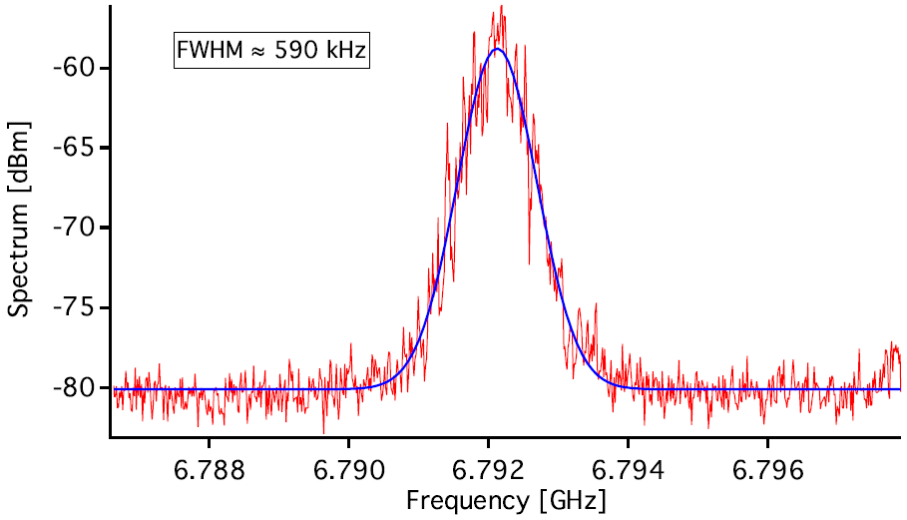

Figure 3.5: Spectrum profile of the beatnote between the Ti:Sapphire laser and the Rb repumping one, locked via the offset lock. This was observed on a spectrum analyzer (ResolutionBandWidth=100 kHz, VideoBandWidth=3 kHz, Sweep time= 80 ms).

range (distance between maximum and minimum closest to the zero crossing) of about 7 MHz. The plots in Fig. 3.4 report three different traces for each spectral window: the red one refers to the error signal of the locked laser; the green one to that of the free running laser; the blue one is a measure of the electronic background noise, since it refers to the error signal when the photodiode was blinded.
The stabilization actively reduces the noise level in the largest part of the observed spectrum. An exception to this is the interval from 40 to 100 kHz: here we can see a vanishing effect of the lock, which actually provides some form of noise enhancement between 40 kHz and 70 kHz. The high frequency cut-off for the noise reduction, found around 600 kHz, was expected: it is due to the presence of a comparable low-pass filter inside the home-made laser box, placed on the current input of the laser diode to shield it from potential current supply noise. As a final step we could get information on the linewidth of the laser, by measuring the full-width at half maximum (FWHM) of its beatnote with a narrow linewidth laser source.
We used a Ti:Sapphire laser, whose tunable frequency emission can be narrowed down to a few tens of kHz in optimal alignment conditions. This system is equipped with two different locks: a primary one ("etalon lock"), used for the coarse wavelength stabilization; a secondary one ("servo lock") for the fine tuning, which stabilizes the laser on a high finesse reference cavity embedded in the laser setup. When both stabilization loops were closed and active, locking the laser close to the Rb cooling transition (780.032 nm in air), we could measure on the internal reference cavity a linewidth of about 62 kHz.
We fiber coupled part of the Ti:Sapphire emission to send it, together with some repumping light, on a second fast photodiode, identical to the one used on the offset lock

circuit. The corresponding beatnote signal we could measure on a spectrum analyzer (after the bias-tee), when both lasers were locked, is reported in Fig. 3.5. We derived the FWHM in two ways, respectively from: a fit of the direct spectrum curve (in dBm), assuming a gaussian profile, as the value -9 dBm away from the maximum then divided by $\sqrt{3}$; a gaussian fit of the data converted to a linear power scale, as the actual FWHM of such gaussian. Both results agree on a value of $\approx$ 590 kHz, which is comparable to the one we measured in the same way for our other laser diode, locked on the saturated absorption spectroscopy.

Chapter 4

Characterizing the Rb system

This Chapter presents the results we obtained while optimizing and characterizing the experimental procedure with the new setup.
In the beginning, we can summarize the main differences introduced from the past in the three major aspects of:

- Larger optical powers for the laser cooling of both species; after the inclusion of extra tapered amplifiers in our setup;

- Possibility to tune the Rb cooling and repumping light in wider frequency ranges: due to the combination of our new optical setup and the offset lock on one of the two lasers;

- Improved vacuum quality after the bake-out.

Other than these, thanks to the new scheme for the repumper, we could also play with the ratio of powers between repumping and cooling components on the output of the Main TA, which we will indicate as repumping-over-cooling ratio (RCR) hereon (meaning the relative amplitude of the repumping light with respect to the cooling light one). To constantly measure this value a small fraction of light is taken on a PBS at the output of the 2D-MOT TA, fiber coupled and sent to a Fabry-Perot interferometer (Free-Spectral Range 750 MHz). The Fabry-Perot transmission is monitored on a photodiode, while scanning the cavity amplitude, to measure the RCR as the relative amplitude of the peaks for the two light components of Rb.

Each of the aspects we listed played a role in determining the differences we found between our new routine with respect to the previous one. Our optimization proceeded separately for the two species, first reaching quantum degeneracy with the rubidium alone, then starting again with the potassium, finally dealing with the mixture from the magnetic trapping onward. Here results for Rb will be presented, following the procedure step by step wherever possible.
In this perspective it is useful to present here an overview of the full procedure, listing the different sequential stages we will discuss in the course of this Chapter.

1. **MOT loading:** The beams of the 2D-MOT and Push are turned on together with the 3D-MOT ones, current is sent through the 2D-MOT and Quadrupole Coils. A MOT is loaded in the Main Chamber from the beam of slow atoms coming from the pre-cooling one.

2. **CMOT:** After the loading is complete, and the 2D-MOT and Push beams are turned off, current in the Quadrupole Coils is increased while changing the detuning MOT of the 3D-MOT beams. The first direct aim of this compressed MOT (CMOT) is to increase the density of the laser cooled atomic sample.

3. **Molasses:** All magnetic fields are turned off and the 3D-MOT beams' detuning is changed again to provide the final laser cooling stage in the optical molasses.

4. **Optical pumping:** After the MOT lights go off, atoms are optically pumped in the desired hyperfine Zeeman state for the magnetic trapping.

5. **Quadrupole confinement and motion:** Current is turned on again in the Quadrupole Coils,to a value high enough to provide a purely magnetic confinement. The atoms are moved to the region of the millitrap, by a motion of the Coils on the translation stage.

6. **Millitrap, evaporative and sympathetic cooling:** Quadrupole Coils go off while millitrap is simultaneously turned on. After the transfer is complete a microwave knife starts the evaporative cooling on Rb, simultaneously cooling potassium in a sympathetic way, and double degeneracy is thus reached.

7. **Optical trap:** Other than producing a BEC in the millitrap itself, atoms can be loaded in the cross dipole trap after a only partial evaporation in the magnetic trap, to finally reach quantum degeneracy under a further forced evaporation in the optical one.

Detailed descriptions of all these steps will be given in the following section, discussing how were all the parameters in the procedure optimized and what characterizations we made.

A foreword is essential to all the results which will be presented hereon: they are valid provided that the Rb TAs are turned off as soon as possible after their use in the experimental procedure. In fact, even in absence of any direct output from the optical fibers, we could observe how the background emission of such devices inside the room causes a critically detrimental effect on the quality of our samples. This emission acts as a constant source of heating and decoherence, and it initially limited the atom numbers and temperatures we could obtain at all stages after the atomic loading.
To overcome these limitations we decided to remote control the current of both TAs with analog channels, allowing for a fast turn off/on of the amplifiers via suitable ramps (the current in the devices mustn't vary too fast, to avoid causing dangerous electrical shocks). We now only keep the TAs active during part of the experimental procedure:

- *Rb 2D-MOT TA*: It is on while the pre-cooling chamber is in use, going off just at the end of the loading stage;

- *Rb Main TA*: It is first turned off right after the optical pumping and it goes back on just before the absorption imaging is performed (staying on until the end of the experimental cycle).

4.1 Imaging techniques

Before discussing the results, we want to briefly review the different imaging techniques used in the course of this Thesis work to characterize each step of the experimental procedure.
The essential method of cold atoms' diagnostics is *absorption imaging*; it reliably gives access to many properties of the system, based on the absorption profile of the atomic cloud, and it proves to be a valuable tool especially in the case of samples approaching quantum degeneracy.
Other than this, we also employed fluorescence imaging as an alternative way to measure the atom number and temperature in the early stages of the experiment, when the low densities don't always allow for an efficient detection in absorption.

4.1.1 Absorption imaging

In absorption imaging the density distribution of the sample is extracted from its optical density (OD) profile. This quantity is introduced as the multiplication factor to the thickness in the exponent of the Beer-Lambert law

$$I_{\text{transm}} = I_0\, e^{-(\int_0^z dz'\, n(x,y,z')\sigma_{\text{abs}})} \tag{4.1}$$

which describes the transmission of light through a medium of thickness z, density n and light absorption cross-section σ_{abs}.
An absorption measurement records the column density of the cloud, that is its density profile integrated along the imaging direction. To do this, the OD is measured by sending a resonant beam on the atomic sample, generally taking a set of three images on a low-noise CCD/CMOS camera. In the first one the probe is shined on the cloud, yielding the intensity profile transmitted through the medium (I_{transm}); the second one only measures the intensity profile of the imaging beam (I_0), in absence of the atoms. A third image is typically needed to subtract from both other images the background signal (I_{bg}) due to light sources different from the imaging beam and spurious signal fluctuations due to the camera electronics. From (4.1) the OD follows as

$$(O.D.) = -\ln\left(\frac{I_{\text{transm}} - I_{\text{bg}}}{I_0 - I_{\text{bg}}}\right) \tag{4.2}$$

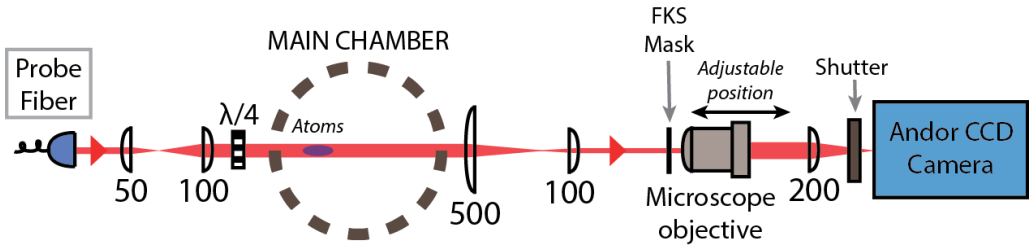

Figure 4.1: Schematic depiction of the imaging setup, where reported focal length values (in mm) refer to the imaging beam along the horizontal direction.

from which the column density of the cloud n_z (corresponding the spatial density integrated along the imaging axis z) is extracted as

$$n_z = \frac{(O.D.)}{\sqrt{2\pi}\sigma_{\text{abs}}}. \tag{4.3}$$

This can be done for the trapped atomic sample (*in situ* imaging), provided a large enough resolution of the imaging system, or more often by imaging the expanding cloud, in a *time-of-flight* (TOF) measurement, after the trapping potential is removed.

Absorption imaging is primarily employed on our quantum degenerate samples. During my PhD we fully redesigned the imaging setup, with the aim of more easily changing the magnification factor in a controlled way, and we also switched to a different camera model.

The Probe beam, at the fiber output on the Vacuum table, is split along two separate paths to access the Main chamber: in the horizontal direction, along the millitrap axis; from the top, in the vertical direction, centered on the minimum of the millitrap and passing through the aperture of its vertical cut. The beams are collimated on the atoms and go through separate telescopes which set the magnification of the imaging region to be acquired.

Right at the output of the chamber a 2-inch-diameter, aspheric lens collimates the diffracted image of the atomic cloud, while effectively focusing the Probe beam. Then the image is magnified with a telescope, constituted by an initial single lens and a final microscope objective of the chosen magnification factor, with the latter mounted on a micrometric translation stage. The advantage of having a microscope objective as part of the telescope is that we can easily switch between different magnifications, simply by setting up different objectives on the pre-aligned mount. In the current conditions the alignment is almost unaffected if we change among different objectives. The scheme is identical for both beams, but the exact optics differ, given the different length of the optical paths the light travels: we typically employ magnification factors of 6× and 10× on the horizontal and vertical beam respectively[1].

Finally, after the telescope, each image is focused on the camera sensor by a single lens.

[1]We report that in all measurements before the addition of ^{41}K presented in this Thesis, a temporary imaging setup was used, which employed standard two-lens telescopes to obtain a camera resolution of: 6.49 μm per pixel on the side imaging and 3.9 μm per pixel on the top imaging.

The new detector is a low-noise EMCCD camera (*Andor iKon-M 934*[2]) with the capability of acquiring fast sequences of images (*fast kinetics mode*, or FKS mode), by limiting the illumination to a partial area of the sensor surface. This is an essential feature, that allows us to acquire the separate images of Rb and K samples (from the same experimental run) with an extremely short relative delay. For instance, when the illuminated region extends to half of the CCD the delay is ≈3 ms; this has to be compared to the >900 ms required for a full readout of the sensor, which would otherwise forbid the double species' imaging. The dark region on the camera was obtained by installing a suitably aligned razor-edge blades in the focus of the imaging telescope, right before the microscope objectives.

A simplified version of the setup we just described was used to image the samples in other stages of the experimental procedure, prior to the magnetic evaporation. In these cases the bigger size of the atomic clouds demanded for a much larger field of view, and lower resolution than for the BECs. The same horizontal Probe beam was employed, but after the Main chamber and the first (aspheric) lens we added a single lens, focusing the image on a different CCD camera (*mvBlueFOX-120a*[3]) installed before the usual imaging telescope.

4.1.2 Fluorescence imaging

During the optimization of our laser cooling and optical pumping stages, the size of the clouds was often comparable with the diameter of our Probe beam and the resulting column density was extremely small. For a better detection in these cases we used fluorescence imaging, its major advantage being the possibility to perform TOF measurements on larger and hotter clouds, thanks to the large size of the MOT beams it relies on.
For this probing scheme atoms were released from the desired cooling/trapping stage, then the 3D-MOT beams were turned on in fixed conditions of power and detuning (without turning on the Quadrupole Coils) and the resulting fluorescence signal was captured on the BlueFOX CCD camera, imaging the central region of the Main Chamber from one of the MOT viewports. The properties of the sample were then extracted from the spatial distribution of the cloud and the corresponding "fluorescence integral" (FI, V_{Fluo}). Inside the field of view of the fluorescence imaging camera we could see the millitrap front side, which made the measurement of real sizes much easier: first it allowed for an optimal imaging of the atomic cloud, focusing the imaging on the trap facet (given the sufficient depth of focus of the imaging system); secondly it made the scaling from pixel to millimeters much easier, as we could use its known dimensions as a direct reference inside the images.

In the actual imaging protocol we took two images, similarly to what is done for

[2]The maximum frame-rate is 4.4 fps, but the pixel readout rate goes up to 5 MHz. The sensor size is 1024×1024 pixels, with single pixel size 13×13 μm. Our camera is cooled down to -60 °C during operation.
[3]Resolution 640×480 pixel, pixel size 7.4×7.4 μm, max frame rate 100 Hz.

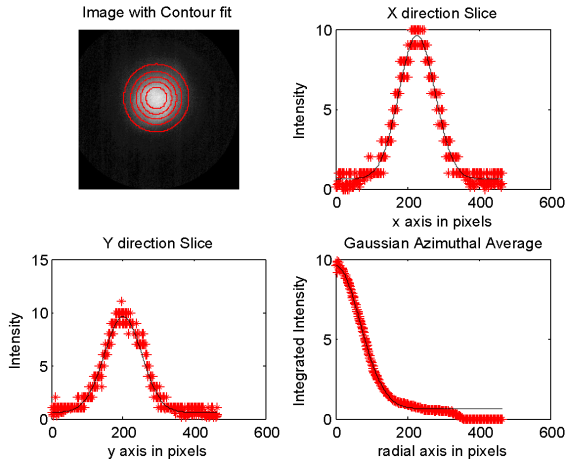

Figure 4.2: Example of a fit from fluorescence images, in this case a cloud after 20 ms TOF expansion from the Quadrupole. (Note that the digitization shown in the data for X and Y slices is just an artifact of the plotting options, which only selected a limited amount of datapoints; the fit was performed on the full set of points instead.)

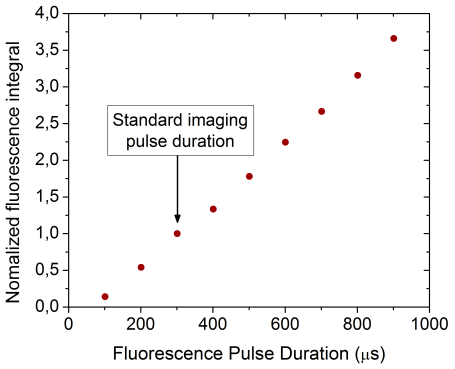

Figure 4.3: Calibration measurement for the fluorescence imaging on Rb. In the plot the fluorescence integrals are normalized to the value obtained for the 300 μs pulse, where the calibration for atom number conversion was performed.

absorption, first shining the MOT pulse on the sample (I_{fluo}) and secondly taking a reference image performing an identical pulse but without the atoms (I_0), to extract the fluorescence distribution as $n_{Fluo} = I_{\text{fluo}} - I_0$. From a gaussian fit of n_{Fluo} we estimated the cloud radius in the vertical and horizontal directions (σ_V, σ_H) and the amplitude A_{Fluo}, from which it followed $V_{\text{Fluo}} = A \times \sigma_V \sigma_H^2$ (we assumed an isotropic MOT in the horizontal plane to estimate the sigma along the integrated direction).
To get a conversion factor of numbers per unit of FI we took a series of measurements with samples of different sizes, and compared V_{Fluo} (at a given exposure time) with the optical density taken from a parallel absorption imaging setup, using our Probe beam on the cooling transition, in the same experimental conditions. We selected the imaging pulse duration making sure that the fluorescence showed no saturation effect, checking for a linear dependence of the integrated fluorescence signal on the exposure time (as shown for instance in Fig. 4.3).

Finally we note that when performing fluorescence imaging, before extracting information from the cloud size, one has to take into account the heating and consequent expansion introduced by the imaging light. Each of the spontaneous emission processes adds a fluctuation on the atomic motion, resulting in a change in the atomic root-mean-square velocity v_{rms} and position. If we take an imaging pulse of duration Δt on the D_2 line, the number of scattered photons by an atom is $N_{\text{scatt}} = \Gamma_{D_2} \Delta t$ and each of them contributes a recoil velocity v_{recoil}; we can estimate the velocity to change by an amount [55] $\Delta v_{\text{rms}} = \sqrt{\frac{N_{\text{scatt}}}{3}}\, v_{\text{recoil}}$ and the spatial displacement introduced by the imaging will be

$$\Delta r_{\text{rms}} = v_{\text{rms}} \Delta t/3 = \frac{v_{\text{recoil}}}{3} \sqrt{\Gamma_{D_2}} \Delta t^{3/2}. \tag{4.4}$$

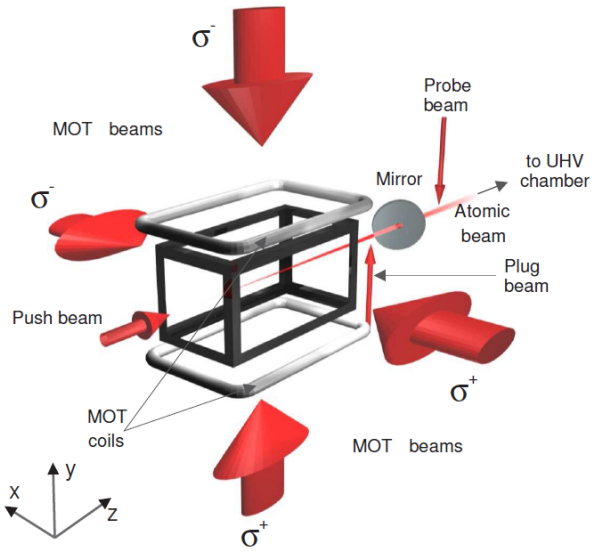

Figure 4.4: Schematic depiction of the 2D-MOT Chamber structure and the associated laser beams.

Substituting for our numbers in the case of Rb, where we used a 300 μs pulse of 3D-MOT beams with $v_{\text{recoil}} \approx$5.88 mm/s, one gets a displacement of $\Delta r_{\text{rms}} \approx 60$ μm. As we shall see later on, the cloud diameters we obtained were always larger by at least one order of magnitude, so this correction was generally neglected in the results we present.

To retrieve temperature estimates of our samples we acquired TOF expansion curves, and we fitted the sigmas $\sigma(t)$ for the gaussian profiles at time t according to equation

$$\sigma^2(t) = \sigma_0^2 + \frac{k_B T}{M} t^2 \tag{4.5}$$

leaving the temperature T and the initial size σ_0 as fit parameters, and M indicates the atomic mass.

4.2 Pre-cooling stage: 2D-MOT and Push beam

Starting from the vapors emitted by our sources, a two-dimensional MOT (2D-MOT) is used in the experiment to collect atoms with suitable velocities and send them to the Main Chamber, in a controlled flux. We can see from the schematic depiction of our 2D-MOT setup in Fig. 4.4 that, given the configuration of magnetic fields and lights, in the pre-cooling chamber atoms are slowed down only in the two transverse directions, by two couples of counterpropagating σ^+ polarized beams. They are made elliptical (waist: longitudinal 2.7 cm, transverse 0.9 cm) by means of cylindrical telescopes to maximize the capture region and the time spent by the atoms inside the MOT potential (condition which determines the chamber's aspect ratio). In the third (longitudinal) direction, where any cooling would counteract the required flux, an effective velocity selection occurs via the narrow skimmer aperture (1 mm diameter) through which the

atoms flow out. In fact, the longer the time the atoms spend inside the illuminated region of the chamber, the smaller their velocity spread is in the transverse directions, which sets the probability of reaching the Main Chamber.
The flux due to the sole 2D-MOT beams is enhanced by means of the *Push* beam, aligned along the flow axis to provide a preferential velocity towards the Main Chamber; it has a waist of ≈1.5 mm and it is σ^+ polarized. In the past it solely consisted of light from the cooling source, whereas with the new optical scheme it inevitably carries a repumping component too, coming from the output of the Main TA. While we did not expect any significant difference in the results, this had to be verified a posteriori.

The tunable parameters of the pre-cooling stage are the magnetic fields from each of the coils (and the resulting magnetic field gradient), the power and the detuning of both the 2D-MOT and push beams, plus the alignment of the latter.
In this early stage of the procedure's development, we used the 3D-MOT fluorescence as the signal to optimize parameters on. For this sake, the 3D-MOT has been loaded in the fixed conditions of: ≈60 mW total power, evenly split among the 6 beams of the three cooling directions, with about 10% RCR; detunings of -12.4 MHz for the cooling light, -0.5 MHz for the repumping one; a 4 A current in the Quadrupole Coils (the usual condition for the MOT loading), producing a 16 Gauss/cm magnetic field gradient in the vertical direction. The MOT loading time was kept fixed for each series of measurements, but set at different values in different optimizations, to always remain in the (approximately) linear region of the loading fluorescence curve vs time. We chose this condition so we could more safely assume the MOT fluorescence to be directly proportional to the actual atom number inside the trapped cloud. The fluorescence was captured from the Main Chamber's viewport opposite to the millitrap (so about 45° away from the directions of the two horizontal directions of the 3DMOT), by collecting its signal on a mirror and focusing it on a tunable gain photodiode. An interferential filter centered at 780 nm(*Lambda 780.0 F-10*, transmission bandwidth of 10 nm) was used to clear the signal from all background light, while the direct contribution due to the light of the cooling beams only provided a fixed offset. By taking into account the numerical aperture of this probing setup we could give a rough estimate of the collected fraction of light to be on the order of 1‰.

We initially did some preliminary characterizations with the 2D-MOT in absence of the Push beam. First we set the physical alignment of the 2D-MOT beams and the values of the currents in the three coils to maximize the 3D-MOT fluorescence; the optimal loading conditions are set by the interplay between the beams' alignment and magnetic field one, but they actually depend on power and detuning too. At this stage we kept the 2D-MOT fixed in the old running conditions, of about 100 mW power and a detuning of -7.4 MHz from the cooling transition.
In order to minimize the consumption of our dispenser, we then identified the minimal current requirement to get a sufficient vapor pressure of Rubidium for the MOT loading. Starting from a negligible atomic pressure and no detectable MOT, we gradually increased the current through the dispenser and measured the loading fluorescence, waiting long times at each new value to allow pressure to settle inside the chamber. A

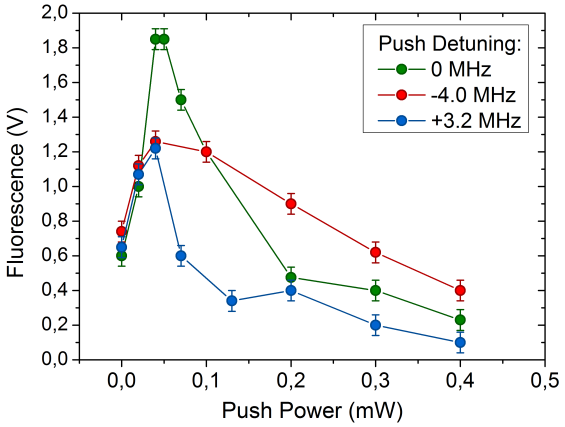

Figure 4.5: MOT fluorescence after 10 s loading time plotted versus the Push beam power, for different detunings of the latter (values in the plot are referenced to the cooling transition). Error bars refer to the noise level we measured on the fluorescence signal from the photodiode.

threshold for the Rb emission rate was found at 2 A (below this value no detectable loading could be seen), while a knee was seen at about 3 A current: the loading rate stays roughly constant between 2 and 3 A, and rapidly increases between 3 and 3.5 A. It keeps on growing, yet more slowly, at least up to 4 A where we stopped our scan of the current. In conclusion, we decided to keep the dispenser current at the intermediate value of 2.4 A.

We also proceeded to look at the effect of different RCR at fixed powers and detunings, finding that indeed a fraction of about 10% repumping light maximizes the loading fluorescence, over any smaller or larger value. Note that this result cannot be considered a priori as an optimization of the repumping requirements in the 2DMOT, since a change in RCR also affects the 3D-MOT light, which stops being an independent probe of the loading quality.

For the optimization of the full pre-cooling setup, including the Push beam, we performed an initial scan with a limited set of powers and detunings of the latter and fixed 2D-MOT parameters. The results in Fig. 4.5 indicate that the best loading is reached with a quasi-resonant beam ($|\delta_{\text{Push}}| < \Gamma_{D_2}$) of <0.1 mW power; here the frequency change was performed via the 2D-MOT AOM, so it simultaneously affected both the cooling and repumping frequencies.
These data were taken using a Push beam perfectly aligned to the longitudinal axis of the chamber, with a diffracted spot fully overlapped to the aperture of the Main Chamber channel. We then went on to identify the optimal alignment of the beam, finding that the atomic flux quality is improved when the beam does not hit the skimmer aperture at all (Fig. 4.6). We could also see that slightly larger powers ($\gtrsim$0.2 mW) further improve the loading in this "misaligned" configuration. A heuristic explanation for this result is that the presence of a repumping component allows the atoms to still be accelerated by the Push beam, even inside the skimmer, where in absence of any compensation

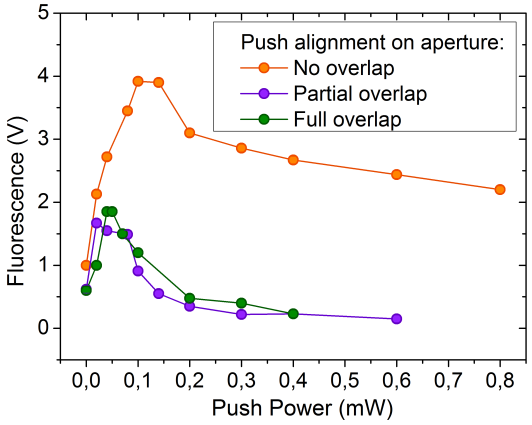

Figure 4.6: MOT fluorescence after 10 s loading time versus Push power, for different alignments of the beam. Error bars refer to the noise level we measured on the fluorescence signal from the photodiode.

from the 2D-MOT cooling their velocity can exceed the capture velocity limit of our 3D-MOT. The fact that when the Push beam is perfectly aligned on the aperture the best flux occurs for a negligible amount of power might also be consistent with such an explanation.
Following these results we set the Push to 0.2 mW power and a detuning of -2 MHz (cooling component), in the "misaligned" configuration.

The final and more important optimization regarded the powers and detunings of 2D-MOT beams. We began by taking series of MOT fluorescence measurements for different laser intensities at fixed detuning, repeating for a set of red detunings for the cooling light in the range $\Gamma_{D_2} < |\delta_{\text{Cooler}}| < 4\Gamma_{D_2}$[4]. Data in Fig. 4.7 show how the optimal power shifts to larger values as the detuning increases, up until a detuning of $\delta_{\text{2DMOT}} \approx -3\Gamma_{D_2}$, where the best conditions are met. This agrees with the picture in which shifting farther away from resonance leads to a net improvement in the 2D-MOT cooling efficiency for as long as there is enough intensity to compensate, since at larger detunings the effect of re-scattered light is minimized. In the 2D-MOT this behavior breaks down for the larger frequency shifts we tested, and a compromise is found where the maximum loading occurs.
We then tested these results against different Push beam configurations. Here we only report for reference the results of a variation of the 2D-MOT and Push detunings against each other, in Fig. 4.8, to highlight that no significant deviation was found from the optimal detunings identified in the separate optimizations, which can be taken as still valid within one linewidth.

In conclusion, we report the final running conditions for the pre-cooling stage of Rb in Table 4.1.
The big difference from the past lies in the detuning and power of the 2D-MOT beams;

[4]The dependence on the repumper detuning was found to be weak, with red detuned values within $2\Gamma_{D_2}$ from resonance giving equivalent results.

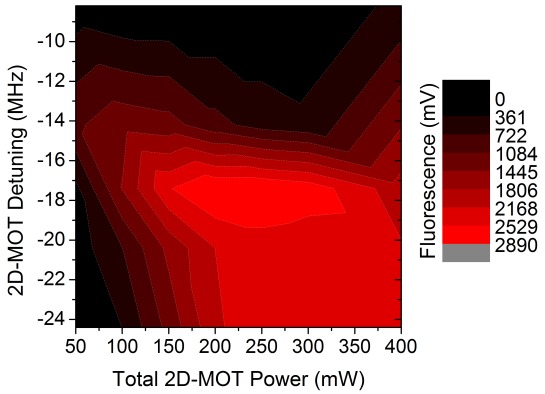

Figure 4.7: MOT fluorescence after 5 s loading time plotted versus the total power of the 2D-MOT beams and their detuning (indicating the cooling component).

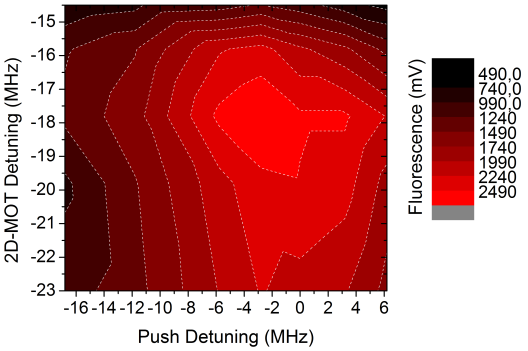

Figure 4.8: MOT fluorescence after 5 s loading time, for different detunings of the 2D-MOT and Push beams (indicating the cooling component).

Table 4.1: Optimized parameters of pre-cooling stage.

Parameter	*New value*	*Old value*
2D-MOT Power (Total)	250 mW	100 mW
2D-MOT Detuning, Cooler	-17.8 MHz	-12.4 MHz
2D-MOT Detuning, Repumper	+0.5 MHz	-0.5 MHz
Push Power	0.2 mW	5 mW
Push Detuning, Cooler	-2.0 MHz	0 MHz

back then the experiment the 2D-MOT was running at the maximum available power, and the detuning optimization was most likely only valid within the allowed intensity range. In light of this, we can also expect that smaller flux velocities correspond to our new running conditions, even though no specific measurement to compare to was available for the old setup.

4.3 Laser cooling: 3D-MOT, CMOT and molasses

The flux of atoms from the 2D-MOT is collected in the Main vacuum chamber by the three dimensional MOT (3D-MOT) responsible for the first laser cooling. The confinement is provided by the combination of the magnetic field from the Quadrupole Coils with three orthogonal couples of counterpropagating beams. They have a waist of 0.9 cm, the largest allowed by the dedicated viewports, and a σ^+ polarization. This same beams are responsible for all other steps of the laser cooling performed in our experiment.
For a first optimization of the 3D-MOT detunings we tried loading from the pre-cooling chamber at different frequencies of the 3D-MOT AOM, for a total of 5 s, and finally

switching to a fixed detuning for a short extra time in order to get a comparable fluorescence level for all cases. In particular, we chose to set the cooling component of the MOT light on resonance during this probing phase. The best loading was found for a detuning of -16.0 MHz of the cooling component, with repumping light within one linewidth away from resonance.
We tested for potential variations of this value against frequency shifts in either the 2D-MOT or Push beams; we could see no significant difference in the position of the maximum for changes in a range of about two linewidths around the values we previously identified for the pre-cooling beams. We could also check that the 4 A current in the Quadrupole Coils was indeed optimal.

Once the 3D-MOT parameters were set, we started using its fluorescence signal (as recorded on the photodiode) for the atom number stabilization from run to run: when the other relevant conditions are stable[5], a larger fluorescence corresponds to a larger atomic cloud.
For the active stabilization, the voltage level measured from the MOT loading is compared on a Schmitt trigger to the reference one (user controlled); this basic circuit outputs a TTL signal, on (or off) whether the measured level is lower (or higher) than the reference. Originally the Schmitt trigger acted on the amplitude control of the Push AOM, turning on/off the corresponding beam; this configuration only allowed to strongly decrease the loading without fully suppressing it, since a weak atomic flux still reaches the Main chamber with the sole 2D-MOT light on.
In the final configuration the TTL output of the trigger is sent to the external control input of the Rb 2D-MOT TA driver, directly turning on/off all the cooling light inside the pre-cooling chamber via the current in the optical amplifier. Noticeably TAs are not robust against abrupt changes in their supply current, which are known to rapidly destroy these devices: to prevent their occurrence, in our scheme we effectively turn the TTL step signal into a suitably smooth variation before the analog control input of the TA. The Schmitt trigger output goes through a capacitive circuit with a properly chosen time constant, that limits the current variation below 15 mA/ms. This is safely within the operation range reported by the device manufacturer, and we could register no decay in the emission quality of the amplifier over three years of use.

After the main MOT, the CMOT and molasses were optimized by comparing the fluorescence signal from atoms recaptured in a second 3D-MOT phase, after all the laser cooling stages, with that measured at the end of the initial MOT loading. In this recapture protocol, right at the end of the optical molasses' phase a 4 A current was once more sent through the Quadrupole Coils and the 3D-MOT AOM was switched back at the frequency value used during the MOT loading, without turning on the 2D-MOT and Push beams. The *recapture ratio* is simply taken as the fluorescence voltage of this recaptured MOT over the final fluorescence voltage measured for the loading.
The observed behaviors are reported in Figures 4.9 and 4.10, showing the variation of the recaptured fraction versus the detuning, of both CMOT and molasses, and the duration

[5] In particular we refer to: optical powers and detuning, atomic pressure in the 2D-MOT chamber and loading rate, magnetic field, alignment of the cooling beams and of the photodiode.

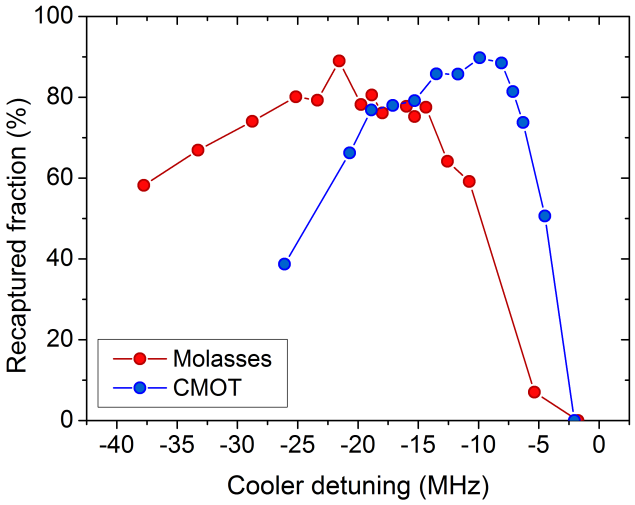

Figure 4.9: Behavior of the recaptured fraction (after the molasses) for different detunings of the cooling light during the CMOT and the molasses. Note that in this second case no CMOT was being performed. For this measurements the repumping light frequency was left unchanged.

time of molasses. Note that the data for the molasses were taken without performing any CMOT phase, only subsequently included in the procedure for its optimization; in the relative measurements the duration of the CMOT was kept constant at 45 ms[6], like in the old experimental routine.
Finally we were able to get an almost full recapture (≈90%), with the chosen conditions of detunings for a molasses time of 4 ms. In particular, this molasses duration was chosen in the perspective of our work on the mixture as the shortest one granting a large and reproducible recapture; potassium-41, lighter in mass and lacking sub-Doppler cooling effects, would in fact suffer enhanced losses in the case of long molasses expansion.

The recapture fluorescence on its own does not give any information about temperature and density, the relevant parameters of the cooling process. To characterize the experimental conditions of the samples, and to check the general validity of the optimizations made, we tried direct measurements of the relevant quantities with the two different techniques of absorption and fluorescence imaging.
An initial fluorescence measurement of TOF expansions after each of the laser cooling stages was used to compare the relative temperature estimates, which we report in Fig. 4.11. We must note that these results should only serve as an indication of the relative behavior, since the exact value might be biases by the improper alignment of the detection camera during these early measurements[7] (which was subsequently corrected).

[6] We waited for the addition of potassium before optimizing this parameter.

[7] In the images, the atomic cloud was significantly overlapped with reflections from parts of the vacuum chamber, so we had to crop the fitting region to a size comparable to that of the expanding cloud after the CMOT. Moreover, the reflection of the millitrap facet (whose dimensions are used for the pixel-to-mm

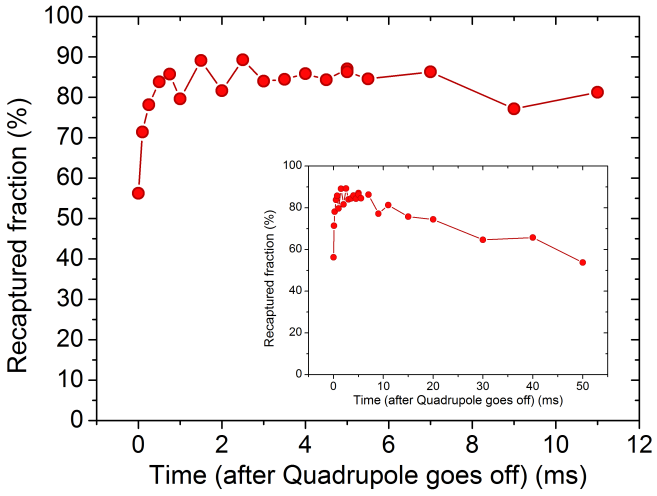

Figure 4.10: Recapture fraction after the optical molasses at the optimized detuning, for different duration of the latter. The inset shows how the same dataset extends for longer duration times.

Nevertheless, we can conclude that the optical molasses can compensate for the heating induced during the CMOT stage (which is mostly important for the potassium sample, as we shall see).
Once we changed the camera alignment we could improve our data quality, eventually getting a result for the final temperature after the optical molasses (Fig. 4.12). Albeit a partial difference in the estimates from the two expansion directions in the image (T_X =98.8±3.0 μm; T_Y =129.5±2.1 μm;), both results are consistent with the presence of sub-Doppler mechanisms during our molasses stage, as expected, even with the short duration imposed by the potassium time limitations. We note that the temperature bound (1.9) in σ^+-σ^- molasses, substituting for our experimental parameters, yields values of: 87 μK if the averaged intensity of the beams is used to calculate Ω_R; 174 μK, if the peak intensity is used instead.
With another series of fluorescence measurements we investigated the effect of detuning during the molasses on the final temperature and density. We didn't see any major variation in the temperatures for changes of ±10 MHz around the previously identified detuning, with values which differ by a maximum of 10%. The density instead clearly gets smaller as we move within two linewidths from resonance.
We can conclude that at the end of the laser cooling we have up to 10^9 atoms, a peak density of the cloud $\approx 3\times10^9$ atoms/cm^3 (right after the molasses), and temperatures around 100 μK; which correspond to a PSD on the order of 10^{-8}.

conversion) was not optimally into focus for the imaging system, determining a increased uncertainty in the conversion to real sizes. Because of the latter, for different conversion factors within the uncertainty range, absolute temperature estimates vary up to 25%.

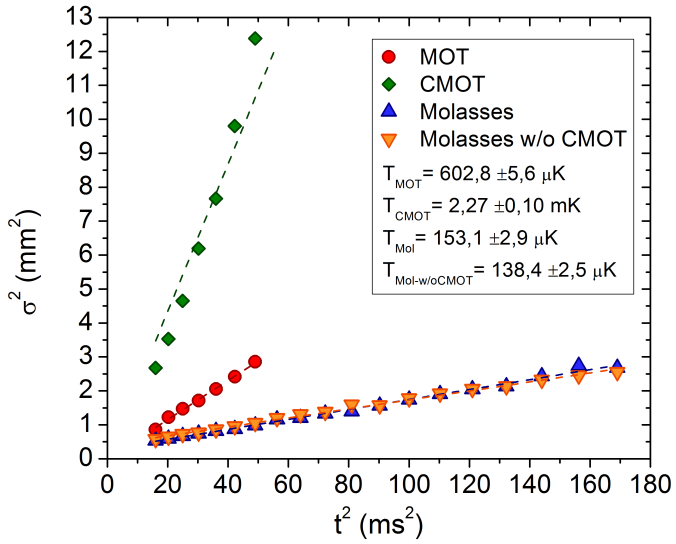

Figure 4.11: Comparison of the cloud size during TOF expansion, after different stages of the laser cooling process, as first measured with a (noisy) fluorescence imaging. Each image was fitted with a gaussian profile, while the dashed lines show the corresponding fit for Eq. (4.5), used to extract the temperature estimates reported in the plot.

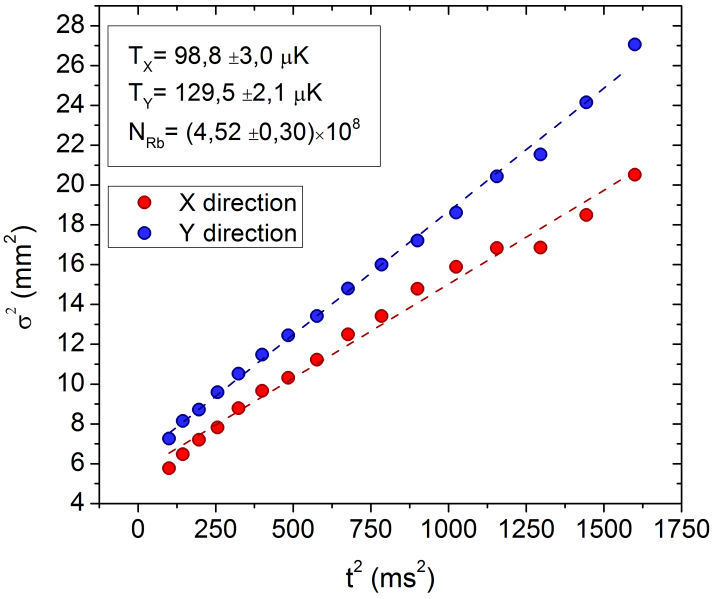

Figure 4.12: TOF expansion profile after the molasses with the best fluorescence imaging, in the two orthogonal directions. Reported temperatures were derived from the fit of each curve as in Fig. 4.11.

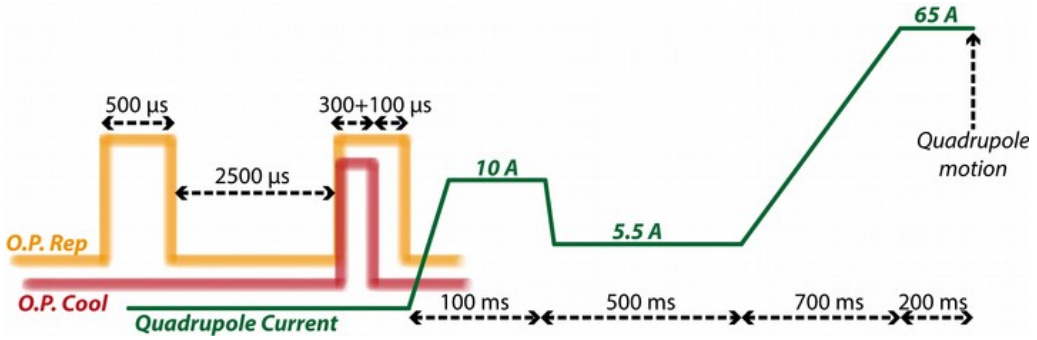

Figure 4.13: Sequence of the optical pumping pulses and following behavior of the magnetic field from the Quadrupole Coils.

4.4 Optical pumping and Quadrupole confinement

In the case of ^{87}Rb and ^{41}K, the signs of magnetic moments in the ground states are such that only 3 out of 8 hyperfine Zeeman sub-levels are low-field seeking states, trapped by the minima of magnetic field: these are the $|F = 2, m_F = 2\rangle$, $|F = 2, m_F = 1\rangle$, $|F = 1, m_F = -1\rangle$. We choose to use the first of the three for both species, for reasons related to the magnetic evaporation of rubidium which will be discussed later on.
After the molasses the atomic samples are in general far from polarized, so the atoms are optically pumped in $|F = 2, m_F = 2\rangle$ before the magnetic confinement, following an appropriate sequence of pulses from cooling and repumping lights.
The beams we use for the optical pumping hit the atoms along the vertical direction; a small magnetic field parallel to the beams is produced by the vertical bias coils, to provide a well defined magnetization axis for the atoms, and the pumping light is seen as σ^+ polarized for the transitions. First, atoms left in the $F = 1$ manifold after the laser cooling are pumped in the $F = 2$ one by shining a pulse of quasi-resonant repumping light, which plays the role of a *Hyperfine Pumping* (HFP). Secondly, a *Zeeman pumping* (ZP) pulse follows, containing light from both sources; in fact, a combination of a quasi-resonant repumper with light from the cooling source, in this case tuned on the $F = 2 \rightarrow F' = 2$ transition, finally pumps the atoms in the only dark state to the σ^+-driven transitions, that is the desired one $|F = 2, m_F = 2\rangle$ [43].

Once the ZP is complete and all laser lights are off, current is sent again through the Quadrupole Coils to provide the magnetic confinement and the vertical magnetic field bias is turned off. The Quadrupole field is then changed according to the sequence depicted in Fig. 4.13; the current finally used in the coils during the motion (65 A) is reached only after temporarily holding the atoms in a shallow quadrupole. This intermediate step is meant to fully remove any remaining Rb atom in the $|2,1\rangle$ state, an extra precaution due to the specific features of our mixture.
When looking at the collisional channels for the trappable sub-levels of the mixture, a critical role for our specific choice of states is played by the collisions of $|2,2\rangle$ atoms with those in the (unwanted) $|2,1\rangle$ state. These can result in spin-exchange processes, removing atoms from the magnetic trap and releasing a significant amount of energy

into the system. We could observe that the two-body collisions which most contribute in making the mixture unstable are those between ^{87}Rb in $|2,1\rangle$ and ^{41}K in $|2,2\rangle$; double degenerate samples can only be produced when a careful spin cleaning is performed.
We must also note that, for each of our species, the $|2,1\rangle$ atoms are more weakly confined than the $|2,2\rangle$, due to their smaller magnetic moment. In particular, this makes the complete removal of $|2,1\rangle$ atoms important even for the case of pure Rb samples: any residual fraction of the atoms in such state is not effectively evaporated, and furthermore acts as a heatload for the rest of the system, especially as the density is increased during the evaporative cooling.

In reality, the efficiency of the optical pumping is never 100% and it concurs to the presence of this specific unwanted state during the magnetic confinement. By exploiting the difference in magnetic moments, we could find a small enough Quadrupole current (5.5 A) that selectively releases Rb in the $|2,1\rangle$ state, due to gravity, while still confining the $|2,2\rangle$ atoms: considering that for the Quadrupole Coils we have a gradient of ≈3.73 G/(cm·A), the threshold currents for gravity compensation are in fact ≈4.2 A for $m_F = 2$ and ≈8.1 A for $m_F = 1$. Note that at the same current nothing similar happens for the equivalent states of potassium, given their lighter mass, and more generally no such cleaning procedure can be performed on potassium without also losing the Rb in $|2,2\rangle$.
In the experiment, a minimum hold time of 250 ms at 5.5 A is required for the $m_F = 1$ removal to be effective. Throughout the developing of the new experimental sequence, we could observe that actively counteracting the appearance of any small amount of atoms in $|2,1\rangle$ can significantly improve the quality of our final doubly degenerate samples[8].

Regarding the optical pumping parameters, durations and powers of all three pulses were again optimized with a fluorescence measurement from a second MOT, using the same recaptured ratio definition we introduced for the molasses. The only difference from the previous case is that here the MOT stage occurred after the magnetic trapping, necessary to sort out the fraction of useful (trappable) atoms alone; after the full sequence depicted in Fig. 4.13, instead of moving the translation stage towards the millitrap, we quickly lowered the Quadrupole Coils' current to 4 A and turned on the 3D-MOT beams, reproducing the conditions of the initial MOT loading and measuring fluorescence on the usual photodiode.
We settled for a condition of equal power in the Optical Pumping beams of cooling and repumping sources (0.8 mW each), with the HFP lasting for 500 μs and the ZP lasting for 120 μs. At the end, we also left an extra 100 μs repumping light pulse after the ZP, to provide a further safety HFP.
A valuable method to check the efficiency of the pumping into $|2,2\rangle$ is to repeat the recapture measurement at different values of the quadrupole during the weak confinement stage, which we use for the final spin cleaning. In absence of any pumping we expect to find the behavior indicated by red dots in Fig. 4.14: at high currents the

[8] We can anticipate how another process exists that induces Rb $|2,1\rangle$ atoms inside the millitrap, but this is related to the microwave evaporation and its discussion is left to the relative Section.

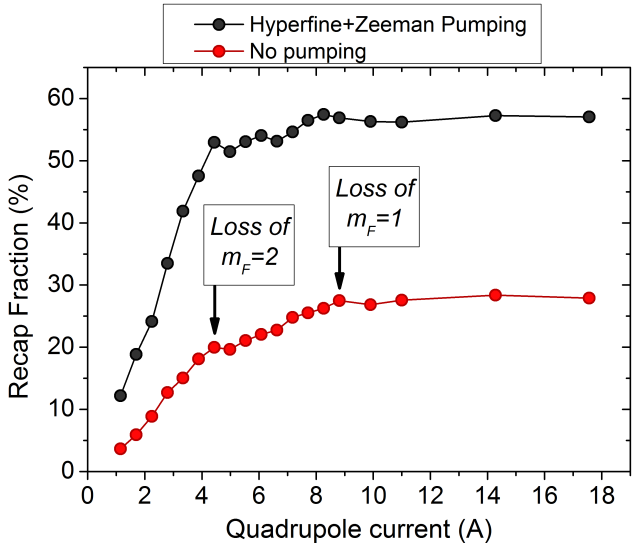

Figure 4.14: Recaptured fraction fluorescence in the MOT after the Quadrupole trapping, for different current values set in 200 ms of shallow confinement. The two sets refer to the cases where optical pumping is performed (black dots) or not (red dots). Error bars report the standard deviation over four measurements.

confinement is strong enough to hold both $|2,2\rangle$ and $|2,1\rangle$ atoms, while all the non-trappable states are lost; below a certain current value the $|2,1\rangle$ atoms start to escape the trap, and the smaller the current the more atoms are lost for a given hold time in the shallow quadrupole; for even lower currents even the $|2,2\rangle$ ones are progressively lost. The corresponding profile of the recapture fraction shows two steps, whose amplitude yields the relative fraction of atoms in the each of the two Zeeman sub-levels.
In optimal conditions, instead, the combined effect of the HFP and ZP is to increase the overall recaptured fraction, recovering the population in the non-trappable states, and to smooth out the first step, by minimizing the fraction in $|2,1\rangle$. The final result in our case are the black dots in Fig. 4.14: the overall recaptured fraction increases from 20% to more than 50%, and only a small amount survives in the unwanted state ($\approx$5% of the initial counts; which gets cleaned out anyway with the 500 ms of hold time in weak confinement).

To obtain a direct measurement of the numbers we again relied on fluorescence imaging, in Fig. 4.15 we compare the atom numbers measured before and after the Quadrupole confinement (including the weak confinement stage) for different MOT loading conditions. The latter is quantitatively measured in terms of the final fluorescence signal from the initial 3D-MOT; in typical running conditions, for instance, we can reach a fluorescence level of 2 V in 20 s of MOT loading. For each of the conditions in the previous plot we also acquired TOF curves, using the same imaging technique, which correspond to temperatures between 100 and 200 μK. They are independent on the loading level, but generally higher after Quadrupole confinement when the optical pumping isn't performed.

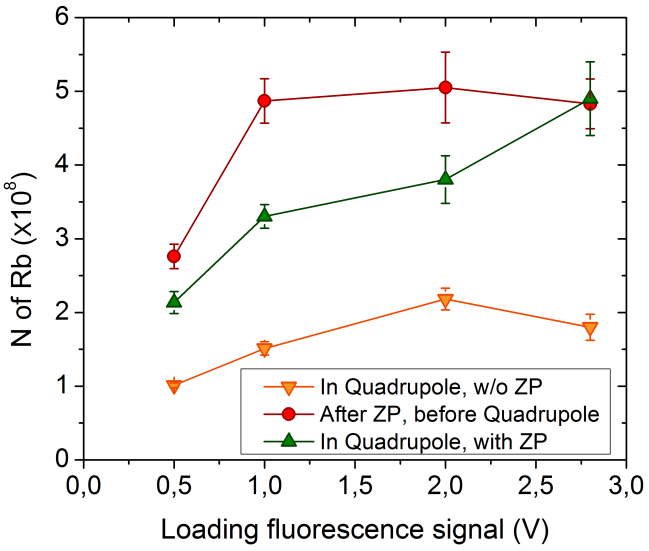

Figure 4.15: Number of atoms measured via fluorescence imaging for different loading levels of the initial 3D-MOT (with maximum-error estimates taken over 4 repeated measurements). The different points refer to the numbers of the expanding clouds measured: after the Zeeman pumping (red dots); from the Quadrupole (green triangles); from the Quadrupole in the case where no Zeeman Pumping was performed (orange inverted triangles).

The previous measurements identify the experimental conditions after the hold-time inside the shallow Quadrupole, but we expected different conditions in the strongly confining field using during the motion of the coils.
An initial estimate of the lifetime was performed by looking at the recapture fluorescence fraction after an increasingly long hold time inside this strong Quadrupole field; with an exponential decay fit we measured a halving time of 44 s, larger than what was last reported before the described upgrade to the Vacuum apparatus. In absence of any difference on the side of the magnetic field properties, which were left unchanged, we interpret this improvement as a first indication of a better quality of the vacuum inside the Main Chamber after the last bake-out.

The temperature in the deep Quadrupole could not be measured via TOF imaging, since when the atoms were released from the strong confinement: the time required for the magnetic field to die down (including that produced by eddy currents) was about 7 ms. After 7 ms, when the expansion could be considered as free, the size of the clouds was already large for fluorescence imaging. Instead, we extracted a temperature estimate from the energy distribution of the atoms inside the magnetic potential.
The energy density was obtained measuring the losses from the trap after a selective removal of the atoms via a resonant microwave frequency[9]. The sample was first held in the strong Quadrupole for the equivalent time of the stage motion (which wasn't being

[9]It was produced by the setup used for the evaporation in the millitrap, which will be presented in the devoted section of this Chapter

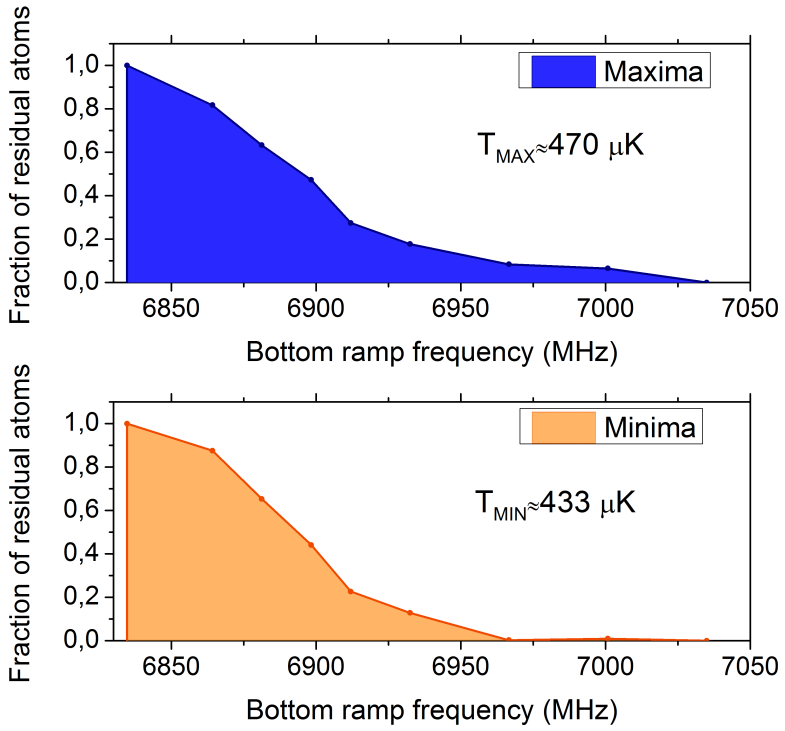

Figure 4.16: Fraction of surviving atoms inside the Quadrupole after a microwave scan in the frequency range $\nu_0 < \nu < 7$ GHz. The two "limiting" curves respectively consider the lowest and highest recaptured fraction values observed over a set of repeated measurements for each frequency.

performed), then the microwave frequency was turned on at a variable initial value ν_0 and ramped up to 7 GHz in 5 ms, transferring to the non-trappable state all atoms with energies $h\nu > h\nu_0$; the recapture fluorescence fraction was then measured as previously described after a TOF sufficiently long time for the Quadrupole field to be zeroed.
The surviving fractions for different cut-off frequency values are plotted in Fig. 4.16. The number of atoms lost at the given frequency ν_0 is given by

$$N_{\text{lost}} = \int_{3(h\nu_0)/2}^{\infty} \rho(E)\,dE.$$

The integral of this quantity over the full frequency range equals to the highlighted region in Fig. 4.16, and it can be easily seen as corresponding to the mean energy of the atoms in the sample $\langle E\rangle = \int E\rho(E)dE$. Now, using the Virial Theorem for our linear trap we also get that

$$\langle E\rangle_{\text{linear}} = 3\left(\frac{3}{2}k_B T\right)$$

to relate energy and temperature.
We took multiple measurements for each cut-off frequency: the maximum and minimum values at every frequency were selected to produce two different curves, from

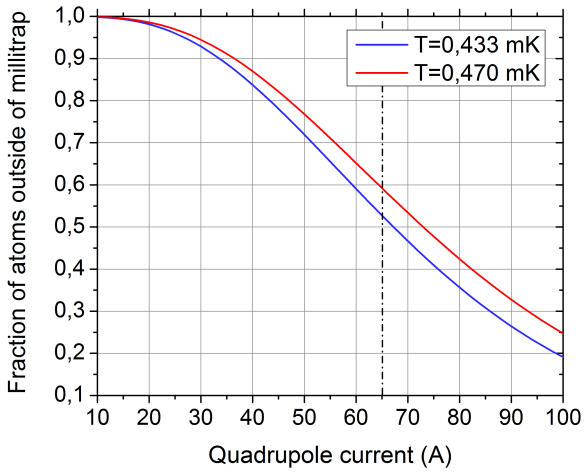

Figure 4.17: Calculated fraction of atoms residing in regions of the Quadrupole trap outside of the millitrap aperture, at different currents in the Coils. For each of the two curves, the atomic distribution in the linear Quadrupole field was derived assuming the corresponding limiting temperature, as derived from Fig. 4.16.

whose integral we could extract an upper and lower bound for the temperature. With this method we could estimate a temperature bounded by the values of 430-470 μK, for rubidium inside the Quadrupole Coils at 65 A.
This method is not extremely precise in presence of noisy atom number measurements, considering how the integral depends the exact value assumed for the maximum atom number (to which the other ones are normalized to). But albeit not perfectly accurate, the magnitude of our estimate is large enough to state that atoms undergo heating when the Quadrupole confinement is strengthened, which is partly expected in the case of an adiabatic compression of the sample.

With this idea in mind, we optimized the current value for the Quadrupole motion, in terms of heating rates and recapture fractions.We first measured the recapture fluorescence for translations over different distances, moving the stage back and forth in a fixed time, to check for losses during the motion.
For all short distances the recaptured fraction is identical and independent from the Quadrupole current; as the zero of the trapping field moves inside the millitrap region, we always see a smaller recapture value, independent on the exact distance but significantly affected by the current. The best conditions are met for 65 A, where we anyway see a 40% reduction of the recapture fluorescence; the smaller the current, the larger the drop in fluorescence after the motion.
These losses aren't simply due to a misalignment between the field zero and the millitrap axis, since adding a vertical or horizontal bias (with our dedicated coils) only made the recapture worse. We attribute the observed behavior to the finite size of the millitrap aperture with respect to the size of the cloud inside the Quadrupole; in fact, as shown in Fig. 4.17, the lost fraction is comparable with a rough estimate for the fraction of atoms

inside the Quadrupole confinement (65 A) at distances larger than the millitrap internal radius.

4.5 Millitrap and evaporative cooling

When the Quadrupole Coils reach the millitrap center, their current is slowly turned off while the millitrap one increases to its final value of 70 A. The transfer is meant to be as adiabatic as possible for the sample, so both the position and the timescale at which it takes place were subject of a separate optimization; we finally settled for a total transfer time of 700 ms. After a wait time of 100 ms we begin the evaporative cooling on Rb, which is induced by a microwave (~6.8 GHz).

In magnetic traps, hotter atoms are selectively removed by sending a proper resonant frequency which transfers them to a nearby high-field seeking state; the forced evaporation is carried out as this frequency is progressively lowered in time. Inside a magnetic potential, the level spacing of the atoms depends on their spatial position because of the Zeeman shift of the internal energies; the hotter atoms can reach regions of the trap where the magnetic field is larger, farther away from the minimum in the center. A given microwave frequency is resonant only at the corresponding magnetic field, thus it may remove only atoms with energy larger than the corresponding trap potential.

We note that the use of a microwave for the rubidium evaporation is a consequence of the properties of our specific mixture. Considering the ^{87}Rb ground state structure, one can always find several high-field seeking states among the Zeeman sub-levels of the same hyperfine manifold; the most obvious choice would then be to set the evaporation knife on one of these Zeeman transitions, since its energy conveniently falls in a radio-frequency (RF) range, rather than on the hyperfine one at 6.8 GHz. While this is the typical solution for most cold atom experiments on rubidium, for our mixture that same RF would also match the Zeeman transition of potassium-41, removing it from the trap.

In our experiment the microwave frequency is provided by a GPIB controlled signal generator (*Agilent E8257D*, max 10 dBm). The low power emission first goes to a fast non-reflective switch (*Hittite HMC547LP3*, DC-20 GHz) and a directional coupler in series, then it is sent to a 40 dB amplifier. A resulting microwave power of ≈8 W is sent on the atoms by a horn antenna (*Q-par Angus WG15*), pointing at the millitrap region of the Main Chamber. Notably, the fast switch can turn off the input of the amplifier in less than a μs (according to the switch specifics the on/off time is just 9 ns); its speed is not strictly required for the evaporation, but becomes a relevant feature in the case of hyperfine transfers.

The steps of the evaporation ramp are triggered by an external signal generator, via a definite number of square pulses at fixed time steps.

During the evaporation frequency ramp, a separate microwave source is constantly kept on to deplete the magnetic trap from $|2,1\rangle$ atoms of rubidium. In fact, throughout the whole ramp, the evaporation microwave is responsible for the constant production

of $|2,1\rangle$ atoms via second order processes. This originates from the fact that a given frequency can be resonant to transitions of both ground level Zeeman sub-states at different magnetic fields; atoms in $m_F = 2$ transferred by the evaporation frequency can be directly coupled back in $m_F = 1$ as they move to a higher magnetic field region.
In absence of an active removal, even a fully polarized Rb sample would eventually contain a small fraction of the more weakly confined state; while the $|2,1\rangle$ fraction induced by this process is not enough to significantly affect the pure samples of Rb, it strongly degrades the quality of double degenerate ones. Since the interspecies collisions among mixed states are especially dangerous in the final stages of the simultaneous cooling, the second microwave source is kept sweeping across the resonant frequencies for Rb $|2,1\rangle$ atoms at the lowest magnetic fields in the millitrap (leaving the other ones unaffected).
The *sweeping ramp* setup differs from the other one we described. The source is a low frequency generator (*Stanford Research Systems DS345*), at a central value of 10.012 MHz with a 7 kHz modulation, which is phase-locked to the same reference signal we use for the evaporation ramp; its output is multiplied by a 683 factor via a BCO, and subsequently sent to a large power amplifier (32 dBm max ouput) and a dedicated microwave horn, identical to the evaporation one. The sweeping ramp is efficiently controlled by turning on and off the BCO, and we found that no further switching electronics is needed.

In order to set an upper bound to the allowed timescale for the evaporation, we performed a lifetime measurement on atoms: the exponential decay fit of data yielded a 90 s time constant[10].
We could observe that a direct application of the old evaporation ramp was enough to first produce a Rb BEC, with atom numbers comparable to the best conditions of the past setup ($\approx 10^5$). The frequency in this ramp follows the profile of a linearized exponential decay, reaching its final value in a total of 20 s.
We went on by checking for variations of this profile, following three different methods of variation.

Our initial approach was to test the behavior of stretched/squeezed versions of the original ramp, produced from the latter multiplying the time separation between each of its steps by a fixed scaling factor. This realized a simultaneous change of the duration and "time constant" of the ramp.
All squeezed ramps resulted in a worse quality of the final sample, preventing the production of quantum degeneracy already for a scaling factor of 0.8. The opposite was true for stretched ramps, as indicated in Fig. 4.18, where we plot the atom numbers observed after the evaporation was stopped at different frequencies (all lying in the final range of the evaporation ramps). The corresponding temperature couldn't be extracted, since in all reported cases quantum degeneracy was produced and no discernible

[10]Notably, if the TAs had not been turned off before the magnetic confinement, this $1/e$ time would have been even shorter than the evaporation time of 20 s; the reduction of the samples' lifetime inside the magnetic traps was the effect which more clearly helped in addressing the detrimental effect of scattered light from the TAs emission.

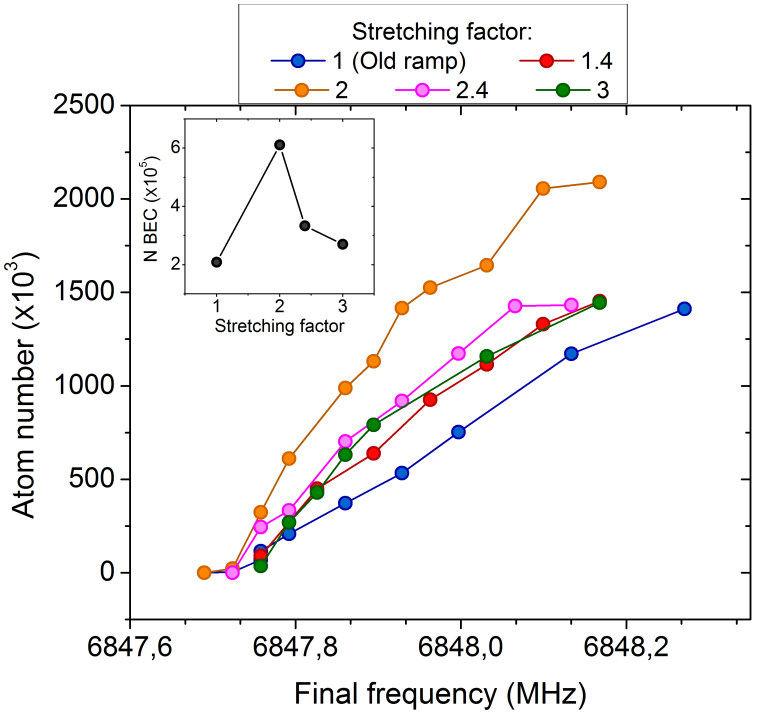

Figure 4.18: Comparison of the stretched evaporation ramps varying the scaling factors. The data report the atom number measured for different final frequencies of the evaporation ramp.

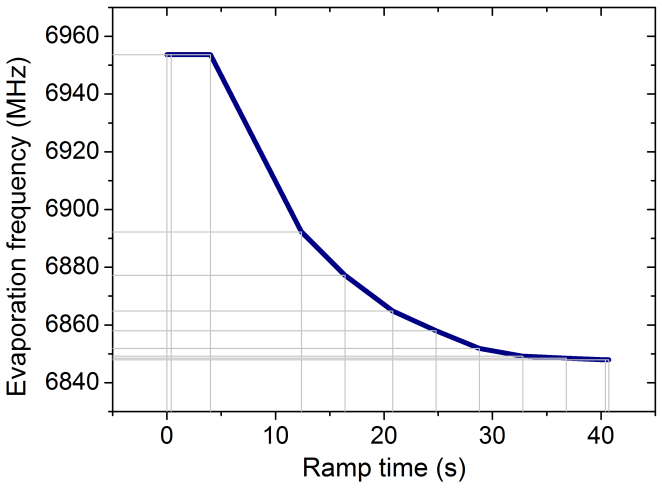

Figure 4.19: Temporal profile of the new evaporation ramp, lasting for approximately 40 s. The grey drop lines indicate the position of the fixed points between which the linearized ramp profile interpolates.

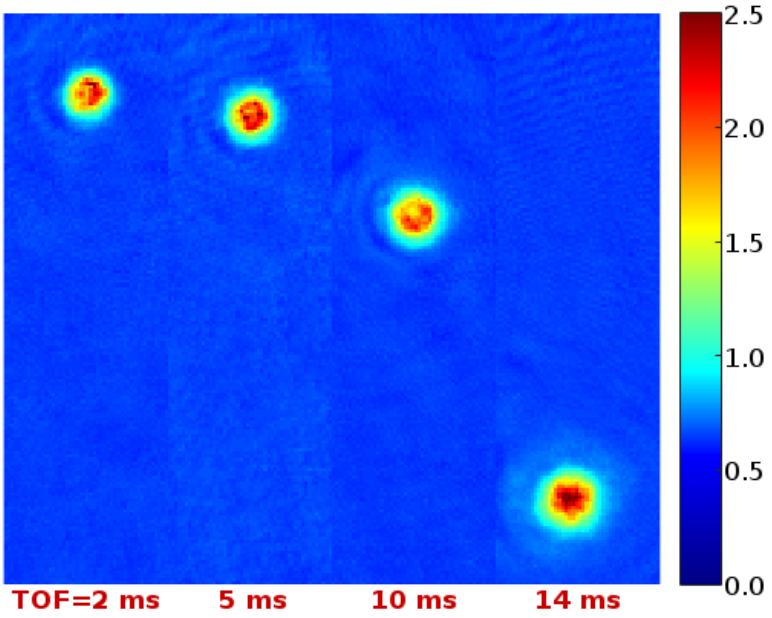

Figure 4.20: Example of a TOF expansion from a sequence of O.D. images for a (optically dense) BEC ^{87}Rb in the millitrap, after a full evaporation. In this case we let a visible thermal fraction survive (O.D.<1 in the distribution tails at TOF=14 ms) to compare its expansion with the BEC one. (The imaging axis is parallel to the elongated direction of the millitrap, thus an isotropic expansion is observed also for the BEC.)

thermal fraction could be detected. Notably, the best BEC always occurred for a same final evaporation frequency value, hence we could directly use the population of the final BEC to address the optimal conditions.
The strongest improvement was seen for a stretching factor of 2 (the corresponding ramp profile is reported in Fig. 4.19). It is crucial to note that in the past any ramp longer than 20 s in duration could never give a degenerate sample, we believe this was a consequence of a poorer quality of the vacuum in the Main Chamber before the latest bake-out.

We then proceeded to characterize the evaporation steps of this new ramp, in terms of atom number density and temperatures (Figures from 4.21 to 4.24). For this process we used both the standard absorption imaging setup (Andor camera) and the secondary one, with the BlueFOX camera and the focusing lens aligned on the horizontal Probe beam axis, to provide a larger field of view on the fast expanding clouds of the early evaporation steps[11].

Initial considerations on the quality of the bare rubidium evaporation can be directly drawn from the data presented here, while a more complete analysis of the millitrap cooling (evaporative and sympathetic) is left to the relative section in the following Chapter about the mixture.

[11] As a consequence, the relative part of the characterization doesn't follow the ramp down to the final evaporation frequencies, where the sample becomes small and slowly expanding and cannot be efficiently imaged with the limited resolution of this setup.

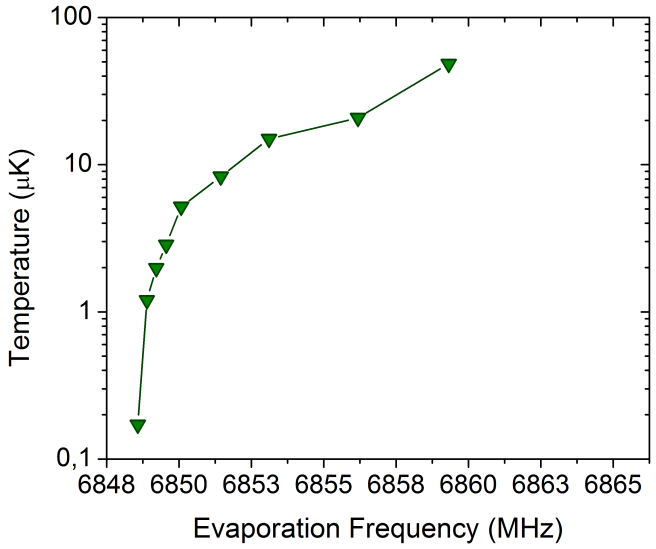

Figure 4.21: Rb temperature (from fit of TOF curves) when the different frequencies are reached during the evaporation ramp in Fig. 4.19.

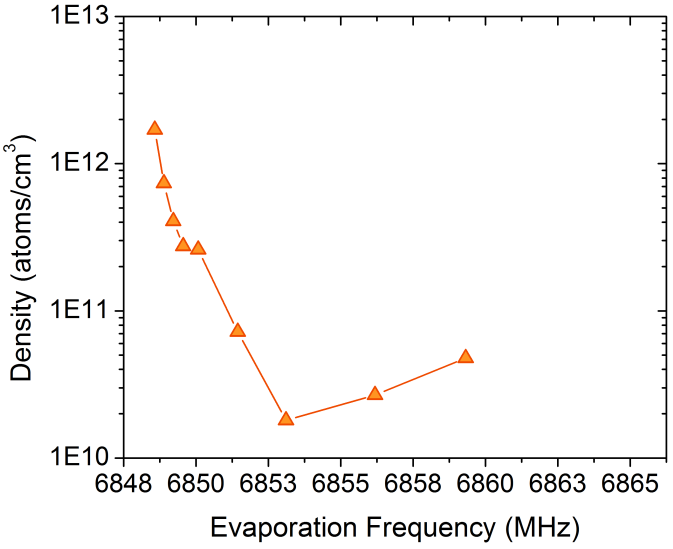

Figure 4.22: Rb densities (after 1 ms TOF) when the different frequencies are reached during the evaporation ramp in Fig. 4.19.

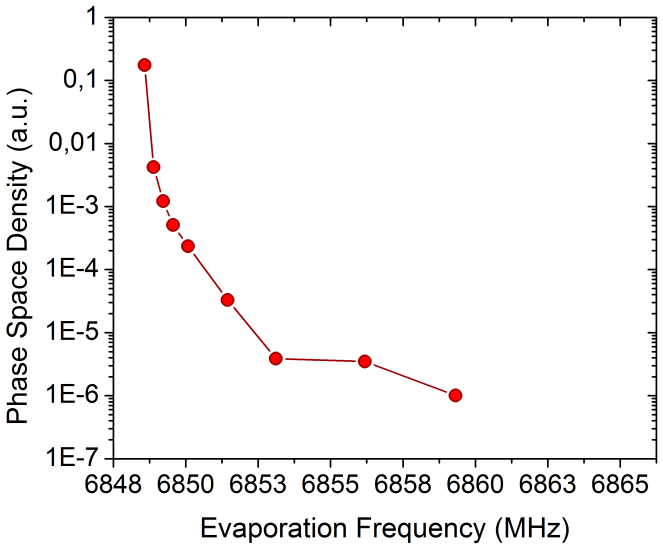

Figure 4.23: PSD estimates at different frequencies during the new evaporation ramp, obtained from the temperature and density measurements of Figures 4.21 and 4.22.

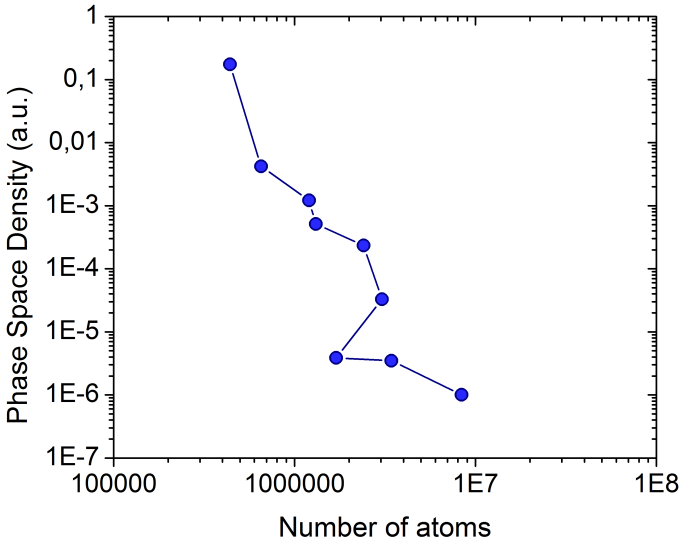

Figure 4.24: PSDs versus atom numbers throughout the 40 s evaporation ramp (for the same measurements as in 4.23).

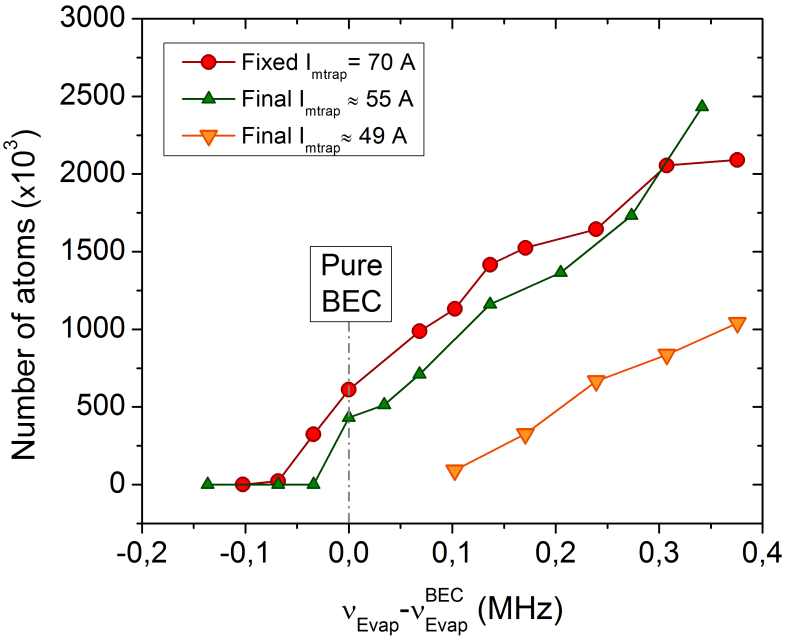

Figure 4.25: Atom number at different frequencies ν_{Evap} of the 40 s ramp approaching the evaporation trap bottom, in three cases of final millitrap current I_{mtrap}: 70 A, normal confinement (red dots); weakened confinement at ≈55 A (green triangles) and ≈49 A. In the plot, since the exact trap bottom varies with the current, all frequencies are referenced to the value where a pure BEC was first produced in each case (ν_{BEC}); no BEC could be observed for I_{mtrap} ≈49 A, where plot frequencies are arbitrarily referenced to ν_{BEC}(55 A).

For practical purposes, the efficiency of evaporative cooling processes on trapped atoms is typically discussed in terms of two parameters (see, for instance [56]): the truncation parameter η, defined as the ratio of trap depth to temperature [57], which estimates how much of the thermal distribution gets cut during the evaporation steps; the scaling (or, efficiency) parameter $\gamma = -\frac{\ln(\rho_{\mathrm{PS}})}{\ln(N)}$ [57], which more directly quantifies the efficiency by weighing the variation of the PSD ρ_{PS} over the corresponding loss of atoms.
In our case, where the trap depth throughout the evaporation is set by the microwave ramp value, a truncation parameter $\eta \simeq 11,5$ could be estimated from a fit of Fig. 4.21. Similarly, data in Fig. 4.24 yield a large value for the scaling parameter estimate, within 20% of $\gamma \simeq 4$, which confirms the high efficiency of the 40 s evaporation ramp across the optimization range considered in the plot.

The second stage of tests on the evaporation investigated the effect of using different exponential decay profiles $\propto e^{-(t/\tau)}$, keeping the full evaporation time fixed but changing the decay time constant τ. This was meant to probe the effect of finer variations of the ramp profile than those performed under the "stretching" method; our starting point was again the 40 s evaporation ramp, almost equivalent to a (linearized) exponential decay of τ =10.3 s.
A comparison of the final BECs from different τ still indicates the initial 40 s ramp as the

best one, but this may only be a consequence of the specific generation method here used for the design of the modified ramps.

In a last attempt to improve our experimental conditions we tried minimizing the heating rate in our final BECs, by decreasing the millitrap current during the evaporation. We wanted to see how much of a reduction we could get on the collision rates of the fully evaporated BEC, while still preserving the final number of atoms.
A set of measurements was taken using the new (slower) evaporation, lowering the millitrap current to different values, 30 s after the beginning of the ramp (when the density has already increased by one order of magnitude). We looked only at the last evaporation steps with the Andor camera absorption imaging, optimizing the efficiency in terms of final atom number in the BEC and slope of the number variation over frequency change.
The plot of Fig. 4.25 only compares the results for three different levels of millitrap weakening with the new ramp, but we repeated a similar set of measurements using the original evaporation ramp too. In all cases, no improvement was observed in the BEC atom number with respect to the constant current condition.

Finally, after settling for the 40 s evaporation ramp, we repeated a final optimization of the earlier stages in the experimental procedure, this time directly maximizing the size of the sample close to the end of the evaporation. In the end we found no clear deviation from the results obtained with the recapture fluorescence, in either of the parameters which were subject to a previous optimization.

Chapter 5

Characterizing the K-Rb mixture experiment

As pointed out in Section 2.1, ^{41}K is characterized by a narrow level spacing in both the ground and excited manifolds of the D_2 line, which results in a largely reduced efficiency of the standard cooling processes. Again consequence of this sole aspect, a series of differences arises in the preparation process with respect to that we just discussed for rubidium.
We must note that in recent years, strategies to produce sub-Doppler cooling on the bosonic isotopes of potassium have been demonstrated [58], but their implementation would have required more significant changes in the case of our mixture system, both in the optical setup (or frequency management of the optical beams) and the control electronics, as well as in the experimental sequence itself. For this reason we decided to postpone the inclusion of a more advanced cooling protocol on ^{41}K.

According to our current procedure the preparation of potassium and rubidium samples takes place in parallel and independent stages, up until the millitrap confinement, as it did in the past; the only a priori limitation due to the addition of the second species is the need to find matching times for the cooling and optical pumping sequences. In the magnetic trap, instead, the temperature and density of potassium atoms at the time of their loading do not grant a sufficiently large collision rate for the forced evaporation to be efficiently initiated; the rubidium is then used as a bath, throughout its evaporative cooling, to sympathetically cool potassium to quantum degeneracy.
We will here discuss where in the experiment, already before the sympathetic cooling, the ^{87}Rb-^{41}K mixture is only not a mere combination of two single species. The presence of the other component affects each of the two in specific ways and the manifest effect is a generalized anti-correlation in the respective atom numbers during the combined confinement, be it inside a magnetic, optical or magneto-optical trap.
Finally, we note that the following results refer to the procedure where the potassium TAs are turned off when not in use, while running the experiment, just like the rubidium ones. Again, the background light emission from the amplifier, scattered onto the atomic samples, is enough to reduce the lifetime in the magnetic traps by one order of

magnitude and to eventually prevent the production of a potassium BEC altogether.

5.1 Optimization of the procedure with potassium

The optimization of ^{41}K procedure was initially performed in absence of rubidium. We initially adjusted the pre-cooling parameters in the same way we described for rubidium in Section 4.2 (note that the 2D-MOT and Push beams of the two species can be aligned independently in the setup). Finally, the 2D-MOT light was set to: ~100 mW total power on the repumping component (close to the maximum available power), red-detuned by ≈17 MHz ($\sim 3\Gamma_{D_2}$); ~250-300 mW total on the cooling component, red-detuned by ≈18 MHz ($\sim 3\Gamma_{D_2}$). For the Push beam we need a power of 0.8 mW, set on resonance with the repumping transition (as in the past), finding similar results to rubidium about the optimal alignment offset from the chamber's aperture.
For the laser cooling of potassium we decided to directly use the atom number inside the Quadrupole confinement as the optimization signal, instead of separately dealing with each stage in shorter sequences[1]. The atom number values were measured using fluorescence imaging[2], in which we needed both cooling and repumping component of 3D-MOT beams to get enough photon counts for the detection, unlike the rubidium imaging, where we could get comparably strong signals by imaging with or without repumper, consistently with the smaller loss rate of its cycling transition. In order to get similar numbers at the time of the detection, we adjusted the loading fluorescence level of the 3D-MOT accordingly for each data acquisition (or, the loading time in the case of the 3D-MOT beams' optimization).
Figures in this Section report the results for the optimizations of detunings (and duration) in all the laser cooling stages, and the temperatures finally measured after each of them (extracted from fits of TOF expansions, from fluorescence imaging).

The 3D-MOT power was set to have a total of 35 mW and 25 mW of cooling and repumping light respectively, values close to the maximum available with our current setup. The optimization results (Fig. 5.1) show that the best detunings for the two components differ by one full linewidth; we could also verify that the atom number did not improve with smaller powers at different detunings. The fact that solely the cooler wants to be within a linewidth from resonance, it might indicate that we are still partially power limited in its 3D-MOT beam, even if the total power was increased by more than 50% in the new optical setup.

Like in the case of rubidium, the 3D-MOT fluorescence signal is used to stabilize the loaded atom number with the same electronics, which for potassium controls the current in the K Cooler 2D-MOT TA.

[1] This approach wasn't merely chosen because of the pre-established procedure developed on rubidium, but it was partly necessary due to the faster expansion of the lighter species in the early laser cooling stages far from optimization.

[2] Finally, we also checked that repeating the optimizations via absorption imaging inside the Quadrupole yielded the same results discussed in the course of this Section.

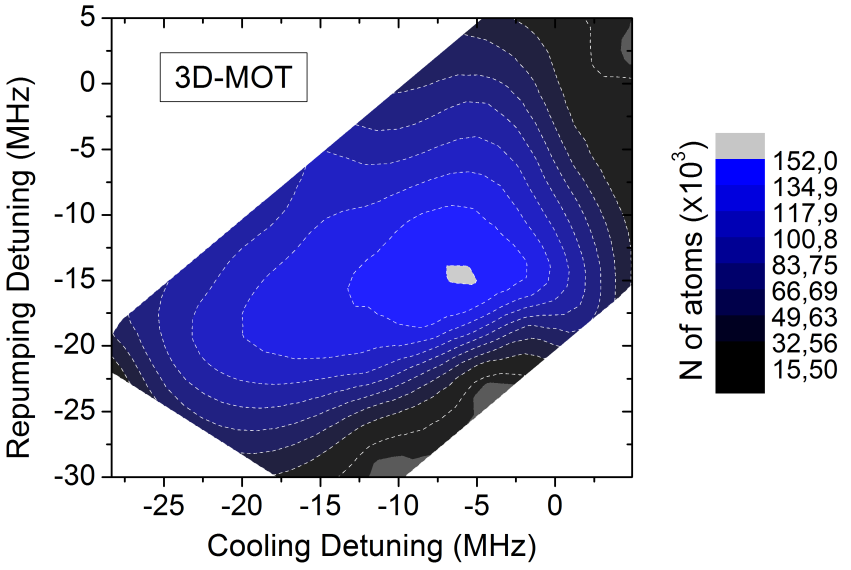

Figure 5.1: Atom number estimate of K sample from fluorescence imaging inside the Quadrupole, for different detuning of the cooling and repumping MOT beams during the 3D-MOT stage.

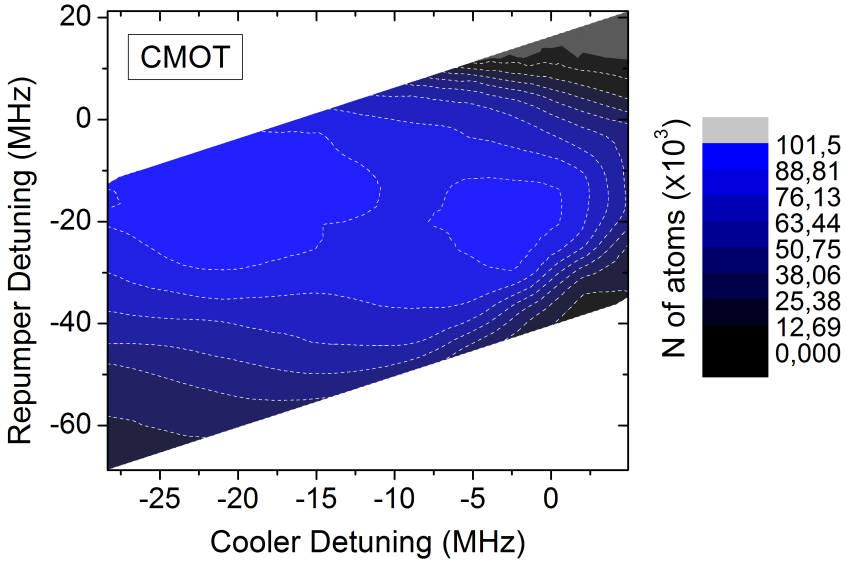

Figure 5.2: Atom number estimate of K sample from fluorescence imaging inside the Quadrupole, for different detuning of the cooling and repumping MOT beams during the CMOT.

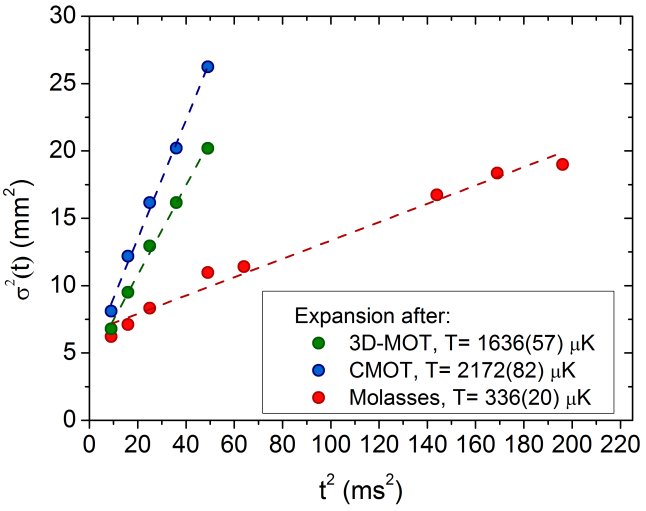

Figure 5.3: TOF expansions of the K sample (from fluorescence imaging) after different stages of the laser cooling. The dashed lines are the linear fits of the curves used to extract temperatures.

The CMOT optimization profile in Fig. 5.2 indicates an unexpected double regime, with two distinct regions giving almost equivalent results (note that one of them has matching parameters with the 3D-MOT). We set the frequencies at the larger detunings, but at this point in the procedure we couldn't resolve any clear difference between the conditions given by each regime[3]. In both cases, the best duration was found around 50 ms and similar final temperature were obtained.

The temperatures estimates extracted from TOF expansions (Fig. 5.3) indicate that, during the compression, some heating is still induced over the final MOT temperature ($T \approx 1.6$ mK); its limited magnitude reflects the fact that the CMOT already starts with a smaller initial PSD. For potassium the necessity of a CMOT stage is apparent, differently from the case of rubidium, considering that in its absence a much smaller Quadrupole capture is always observed. The full set of characterizations we performed indicates that the main role of our CMOT is that of effectively squeezing the cloud, to compensate for the subsequent fast expansion during the molasses (at the cost of a much smaller temperature increase than what is simultaneously seen on rubidium).

In the case of the optical molasses, two main observations can be made about the dependence of the Quadrupole capture on the two detunings (Fig. 5.4). First we notice that the dependence on the repumper one is very weak; secondly, the cooling frequency which maximizes the signal happens to be on the blue side of the transition, albeit within one single linewidth from resonance. It must be noted that deviations from the Doppler or sub-Doppler cooling models are reasonable in presence of the ^{41}K level structure (more complex optical pumping mechanisms might be involved), but we did not have any a priori explanation for the result.

[3]For a more definitive conclusion we had to wait until the final re-optimization, done on the atom number of the potassium BEC in the mixture case.

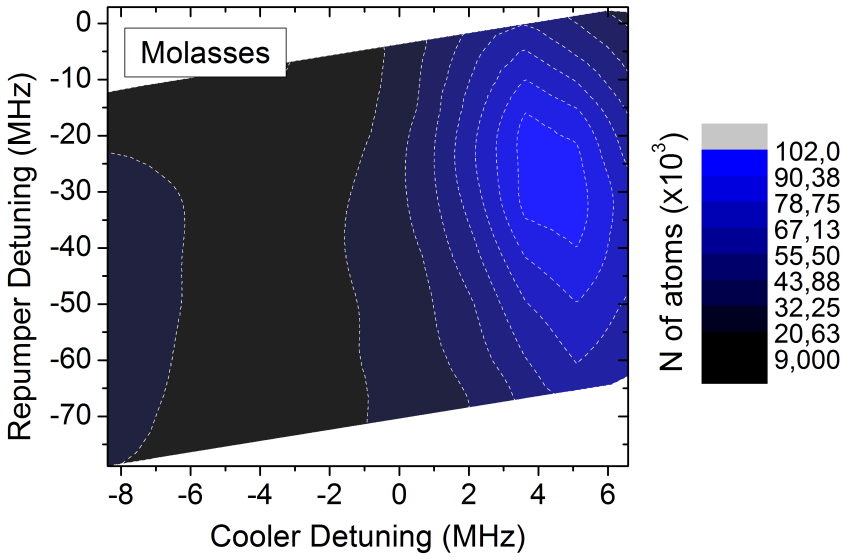

Figure 5.4: Atom number estimate of K sample from fluorescence imaging inside the Quadrupole, for different detuning of the cooling and repumping MOT beams during the optical molasses.

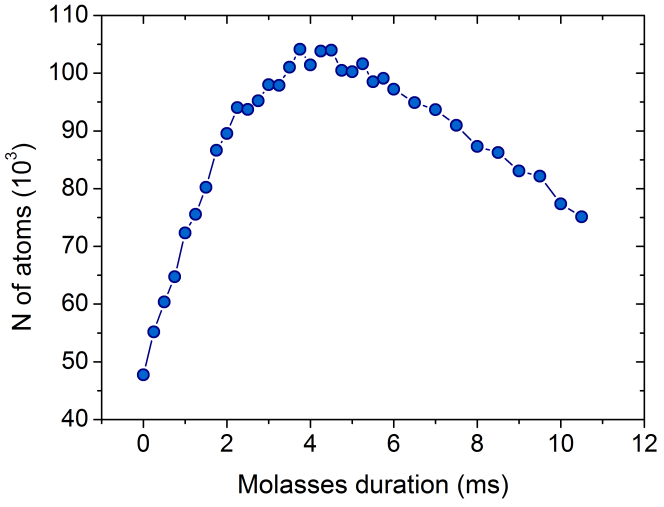

Figure 5.5: Atom number estimate of K sample from fluorescence imaging inside the Quadrupole, for different durations of the optical molasses.

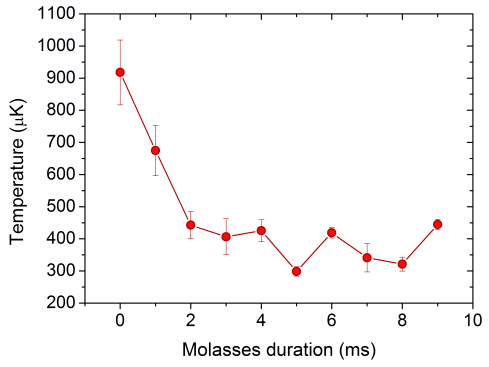

Figure 5.6: Temperature of potassium after optical molasses of different durations. Value are extracted from the fit of TOF expansions, error bars only refer to the error of the fit (they underestimate the uncertainty).

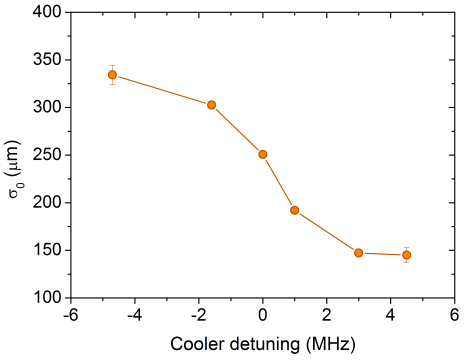

Figure 5.7: Initial size σ_0 (before TOF expansion) of the potassium cloud after the laser cooling, for different detunings of the 3D-MOT cooler beam during the 5 ms of optical molasses. In this data set repumper was kept fixed at $\delta = -30$ MHz. The error bars report the standard deviation over a serie of 4 measurements for each condition (for some points the error bars fell within the dot and were consequently omitted).

In fact, the role of our optical molasses on ^{41}K was not uniquely determined: in absence of cooling processes expected to overcome the limits of the 3D-MOT, the optimal duration of 4-5 ms indicated by data in Fig. 5.5 and the dependence on the detuning could simply be a consequence of effects other than mere temperature ones.
To clarify the actual mechanisms driving the potassium optical molasses, we performed a further characterization by imaging (via fluorescence) the atoms right after the laser cooling, looking at the behavior of the final temperature and size of the cloud.
The plot of the temperature dependence on the molasses time (Fig. 5.6) gives a first significant insight: temperature reaches a lower limit after a 3-4 ms time, which roughly matches our optimization's result. Hence, we can conclude that the molasses duration is set by the timescale at which the cooling stops; any extra time only adds an expansion of the cloud, unmatched by any further temperature decrease.
Then Fig. 5.7 shows how the size of the cloud increases, starting from the optimized conditions, as the cooling beam's frequency is moved across resonance and towards the red side[4]: over the relatively small frequency range we considered (about one linewidth), the σ_0 of the gaussian fit is more than doubled. This strong dependence on the detuning might cause the spatial matching conditions to the Quadrupole trap to be more relevant than the final temperature, for the sake of determining the optimal cooling frequency during the optical molasses. In fact, while it is true that the latter provide a significant cooling even for ^{41}K, they just reach a relatively high temperature $\approx 2.3\, T_D(^{41}\mathrm{K}, D_2)$.

[4]We could see that the dependence on the repumper detuning stayed weak, as already indicated by the previous optimization

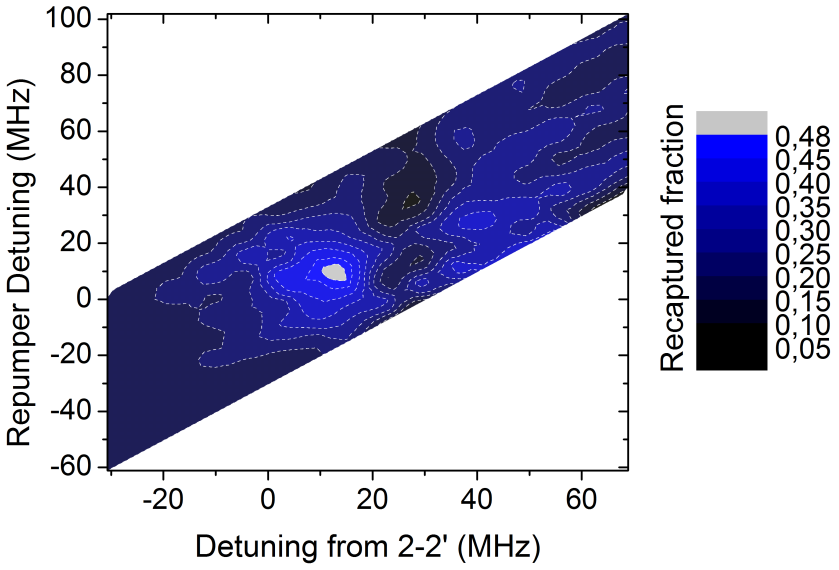

Figure 5.8: Fraction of K atoms recaptured in the second 3D-MOT after Quadrupole confinement, as measured via fluorescence counts on a photodiode, for various detunings of the cooler and repumper components of the Optical Pumping beam during the Zeeman pumping. The horizontal axis refers to the frequency of the cooler beam, but the detuning is referenced to the transition involved in the ZP.

Finally, for a more definitive conclusion to be drawn, one would need to compare the variation of the cooling effect in the same frequency range, measuring the actual temperatures associated to data points in Fig. 5.7. Unfortunately, for both red-detuned frequencies we considered, the large initial cloud size prevented us from obtaining TOF expansion curves for such purpose; just at the end of the molasses, its diameter was already comparable to the free field of view in the fluorescence images (limited by the presence of the millitrap reflection); this.

The optical pumping stage for the potassium cloud is constituted by the separate stages of hyperfine and Zeeman pumping, like the rubidium one, with the difference that only the second stage is performed using the Optical Pumping beam.
The HFP pulse is instead realized by selectively shining the repumper component of the 3D-MOT beams, in order to more safely illuminate (when possible) all the atoms of this cloud, which is larger than the other species' one. In optimal conditions, the light is resonant to the repumping transition and the pulse lasts for 500 μs.
The ZP frequencies were set by looking at the fluorescence signal from a recaptured MOT after the Quadrupole confinement, following the procedure we previously described for rubidium; the recaptured fractions, as compared with the respective initial MOT loading, are plotted in Fig. 5.8. The maximum occurs when the two components are resonant to the $F = 1 \rightarrow F' = 2$ (repumping) and $F = 2 \rightarrow F' = 3$ (cooling) transitions, respectively[5].

[5]This is somewhat nontrivial for the latter, which was instead expected to act on the $F = 2 \rightarrow F' = 2$

During the detuning optimization we used temporary settings for the power and timing of the ZP pulse, which was finally set to have a duration of 100 μs and ≈1 mW in each component; also for potassium we keep the sole repumping component on at the end of the ZP, for an extra 50 μs, to get a final safety HFP. With such sequence we get a recaptured fraction of about 60% of the initial loading.

The pulses for the optical pumping of the two species are matched so that the atoms spend the same time in free expansion, to finally be captured by the Quadrupole Coils' potential and undergo the same sequence of steps inside the magnetic confinement (as pictured by the green line in Fig. 4.13).
The hold-time inside the weak quadrupole has no direct effect on potassium, like we said, because of its smaller mass: residual atoms of ^{41}K in the $|2,1\rangle$ state after the ZP cannot be easily removed once magnetically captured. While they might cause heating and losses in the system during the millitrap evaporation, we can expect such contribution to be limited by their low density.

Multi-component effects before the millitrap

At the time of repeating the optimization of parameters for every procedure stage in presence of the full mixture, we could find the same values as in the single species case for both ^{87}Rb and ^{41}K. We also found matching results for the stages following the laser cooling: at the time of the Quadrupole capture, we get identical temperatures for both species as measured in the single component case, independently on the relative atom numbers; the same can be said for the lifetime inside the Quadrupole trap.

In fact, the sole evidence of a mutual effect is observed during the simultaneous loading, where the atom number of at least one species is decreased by the addition of the other one; this multi-component effect, limiting the amount of atoms which can effectively be captured, is similar to that reported for similar mixtures [59, 60]. It is attributed to a radiative emission from heteronuclear collisions, occurring when at least one of the atoms has been pumped to the excited manifold by the laser radiation. For such processes the interparticle potential scales with the relative distance R as $\sim R^{-6}$, and the timescale of the interaction can be long enough for the excited atom to spontaneously decay while inside the attractive region of the potential [61]: the emitted photon is red-detuned with respect to the absorbed one and the remaining energy is split among the two atoms according to the mass ratio, resulting in the trap losses.
In most known examples in literature, the reported losses are exclusively affecting the lighter mass species [61]; on our experiment we could also observe a mutual effect among ^{87}Rb and ^{41}K, depending on the loading rate from the pre-cooling chamber[6]; this is particularly evident after a simultaneous loading, when both species are approaching the respective MOT saturation level (see Fig. 5.9).
An effective solution (for all loading rates) was found by changing the procedure to

transition for pumping purposes (with $\Delta E_{F'=3-F'=2} = h\cdot$13.4 MHz), at least when only purely resonant processes are taken into account.

[6] We remark that no sign of interaction effects between the two species was ever observed inside this first vacuum chamber, directly.

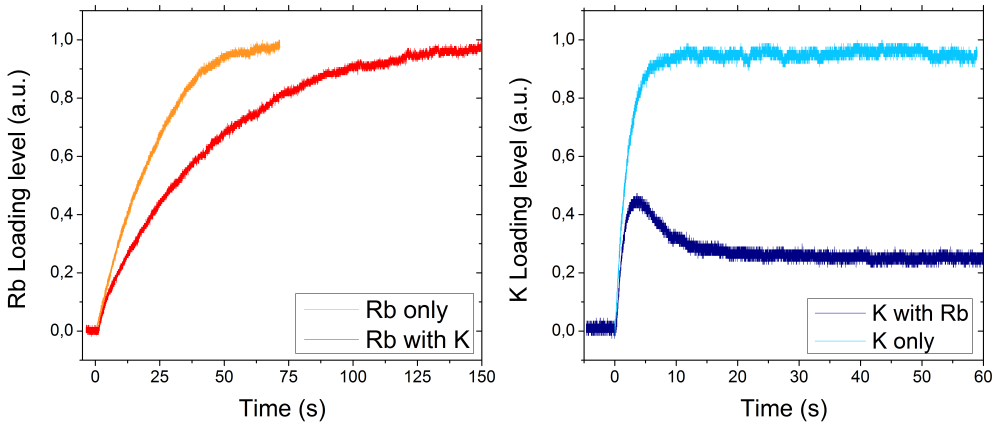

Figure 5.9: Examples of 3D-MOT loading fluorescence curves, comparing the behavior for a simultaneous loading of the mixture (darker colors in the plots) with that of a single-component MOT, in absence of the second species (lighter colors). Here the fluorescence voltages measured on the MOT photodiodes have been normalized to the saturation level of the single-species 3D-MOTs.

load the two species with a relative time delay, where the MOT of the faster loading species is turned on only after the other one has reached the desired fluorescence level; more in specific, in typical running conditions, the ^{87}Rb is first loaded up to the desired level, followed by ^{41}K for a short time. The feasibility of such protocol is granted by the improved loading rate from our potassium source, which we owe to the use of an enriched atomic sample and the higher 2D-MOT power on ^{41}K. Finally, this precaution alone is enough to produce stable conditions from shot-to-shot on our experiment.
The assumption that the loading anti-correlation is a density-related issue was also confirmed in an attempt to further minimize its effect, when we tried to offset the 3D-MOT center of potassium from the rubidium one. We unbalanced the light among two counterpropagating MOT beams of the first species, by adding a dichroic $\lambda/2$ waveplate in the vertical 3D-MOT beams' direction. Even though this partially increased the atom numbers at the MOT level, it also determined worse cooling efficiencies and a smaller Quadrupole capture, which washed out any net improvement.

5.2 Trap confinement and cooling of the mixture

Following the Quadrupole motion, the mixture transfer from the linear to the harmonic trap occurs in the same way described in the previous Chapter; the microwaves for the evaporation and sweeping ramps are then turned on, initiating the cooling process on rubidium, and potassium sympathetically.

After we identified the running conditions to produce double degenerate samples in the millitrap, we went on to fully characterize the mixture cooling process in terms of numbers, temperatures and phase space densities: a selection of such results is reported in Figures from 5.10 to 5.13. For these measurements, the clouds were imaged after

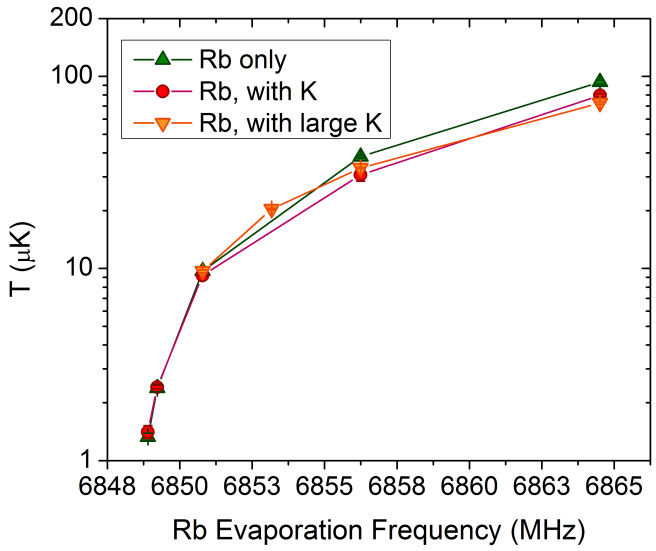

(a)

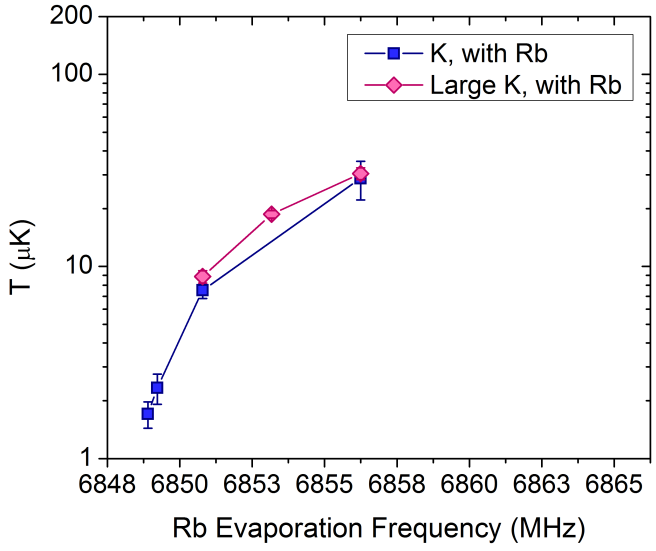

(b)

Figure 5.10: Temperature of potassium (*b*) and rubidium (*a*), during the last 20 s of evaporative cooling of the latter. The multiple curves refer to different loading levels of the initial 3D-MOT of potassium (see plot legend): no potassium loading; enough loading to finally produce small and balanced BECs of rubidium and potassium ($\sim 10 \times 10^3$ atoms); four times as much fluorescence as in the previous conditions. In the latter case, both species were fully lost from the millitrap after 32 s of evaporation.

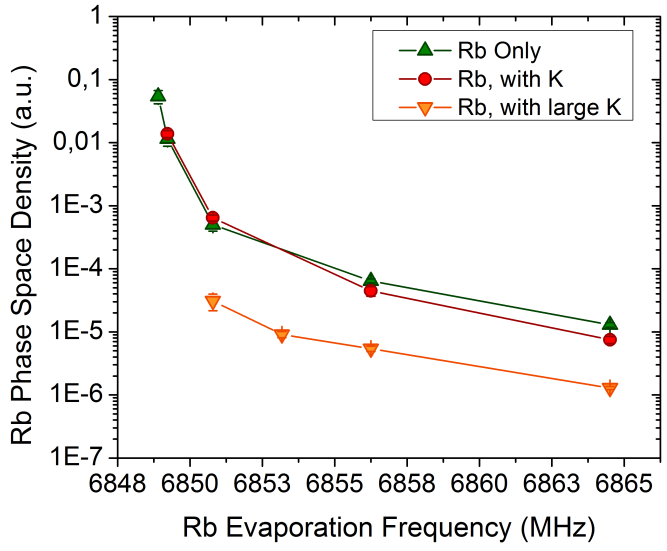

(a)

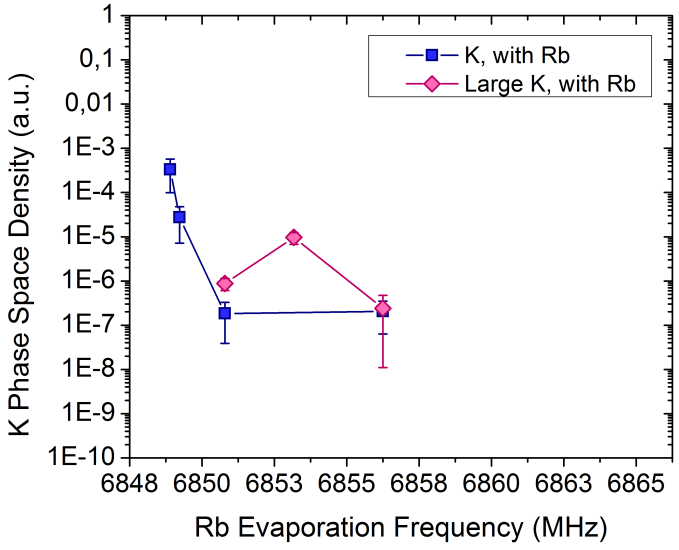

(b)

Figure 5.11: Phase-space density estimates for potassium (*b*) and rubidium (*a*), during the last 20 s of evaporative cooling of the latter. Each curve corresponds to the relative one in Fig. 5.10.

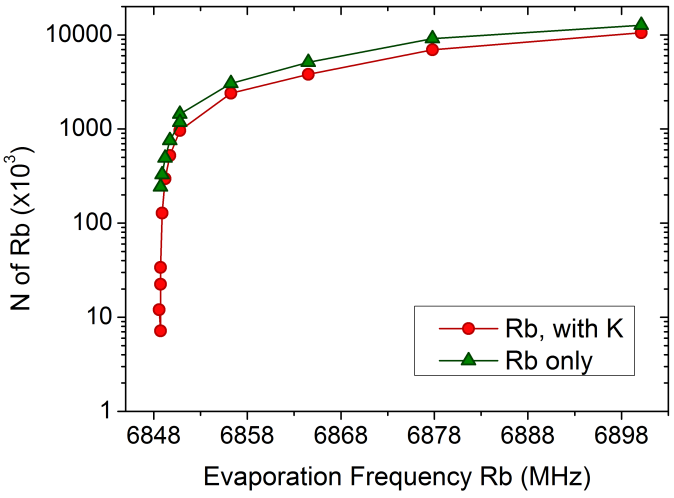

(a)

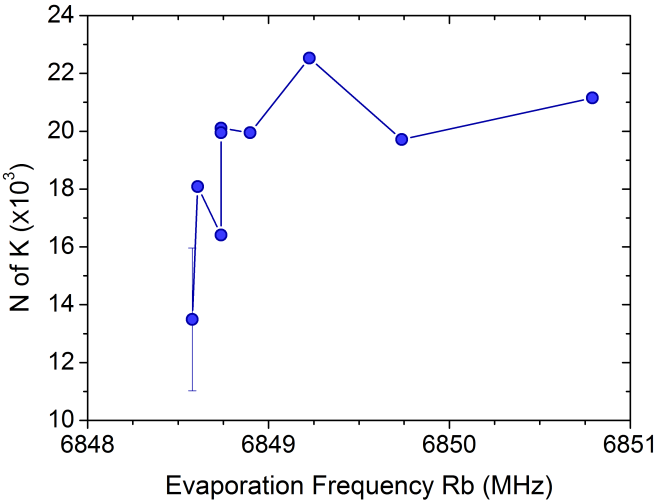

(b)

Figure 5.12: Numbers of potassium (*b*) and rubidium (*a*) during the final evaporative cooling of the latter. In the rubidium plot, the two curves compare the single species result with that for the mixture (where enough K was loaded to have a small double BEC). The error bar in the final point of the K plot indicates the typical fluctuations on its final atom number, for the chosen loading balance of the mixture.

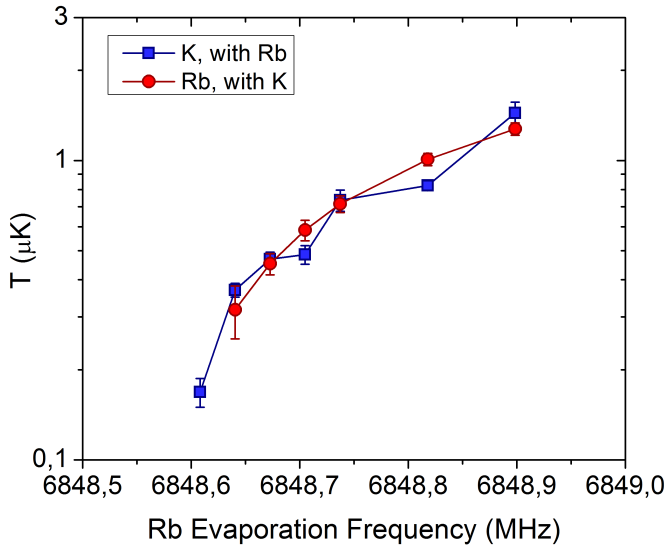

Figure 5.13: Temperature curves for the final seconds of the evaporation, taken in comparable experimental conditions to those in Fig. 5.12. For each set, the frequency at which the solid line interrupts corresponds to the point in the evaporation where no discernible thermal fraction could be detected to derive a temperature.

TOF expansion with our main absorption imaging setup (Andor camera). In the case of rubidium the detuning of the Probe beam for each TOF curve was selected, depending on the atom number, to have suitable optical density values (0.2≤O.D.≤1.5); the Probe beam frequency of potassium was kept fixed, on resonance. To extract a PSD value, the density was derived from the atom numbers and temperatures, using the harmonic profile approximation of the millitrap at 70 A.
The detailed behavior of the system changes depending on relative magnitude of the two samples, with specific turning points during the process, as highlighted by the comparisons in the plots. In general, the mixture cooling sequence can be divided in three stages or regimes, which we will address by the corresponding time during the rubidium evaporation process (lasting for a total of 40 s).

1) Early evaporation: $t_{evap} \lesssim$25 s, or $\nu_{evap} \gtrsim$6858 MHz. In terms of the rubidium observables, we get marginal deviations from the behavior discussed in the previous Chapter; we must remind that, already for the single species case, the initial 20 s of the microwave ramp only gave a poor indication of the evaporation effect on PSD.
Little can be said for the potassium sample, since the optical density of its cloud is just too small to allow reliable number measurements (or temperature estimates from TOF expansion, moreover), whatever its initial loading.

2) Thermal sympathetic cooling: 25 s$\lesssim t_{evap} \lesssim$38 s, or 6851 MHz$\lesssim \nu_{evap} \lesssim$6858 MHz. Temperatures decreases consistently for the components of the mixture, which appears to be in thermal equilibrium, from the initial ~100 μK down to about 1 μK. The number of potassium atoms is relatively stable throughout this stage, as the rubidium

gets evaporated and cooled. The two aspects indicate that in this regime the sympathetic cooling process is most efficiently carried out.
In typical loading conditions, also in this part of the cooling sequence we get limited differences for the rubidium sample with the addition of potassium. More specifically, this holds whenever the initial loading of the samples is balanced to give a detectable number of atoms of each species in the final seconds of the evaporation. Larger deviations arise instead as more K is loaded, up to the point where the rubidium disappears already in this stage of the sequence. Considering the numbers in Fig. 5.12 and 5.13, though, even in such conditions the potassium is efficiently cooled for as long as some significant fraction of rubidium survives.
In the end, while we could effectively observe that a maximum level for potassium loading exists (beyond which the samples don't survive the full millitrap cooling), we can also conclude that this is not consequence of a limiting mechanism for the sympathetic cooling process: eventually, if we could produce larger rubidium samples, we would further increase the size of our double BEC.

3) Approach to quantum degeneracy: $t_{evap} \gtrsim$38 s, or $\nu_{evap} \lesssim$6851 MHz. Already with pure rubidium samples, at the frequency value corresponding to this evaporation time, a knee was observed in the temperature and PSD curves. With the mixture, we also see potassium getting progressively lost from this point on, while the number of rubidium decreases more prominently in its presence[7]. Similarly to other combinations of potassium and rubidium [19], we can attribute this behavior to heteronuclear three-body losses becoming more effective as the mixture hits the high density on the edge of quantum degeneracy.

Nevertheless, in typical running conditions, our system can easily produce double BECs (no visible thermal component) at the end of the millitrap cooling, with different balances between the two components; depending on the initial loading, we can go from comparable numbers ($N_{Rb} \approx N_K \sim 5 \times 10^4$) to a strongly unbalanced mixture ($N_{Rb} \sim 10^5$, $N_K \lesssim 10^4$).
To shed some light on the mechanisms which set our atom number limits after the millitrap cooling (other than the losses in its final seconds), we looked at the heating rate of the samples inside the millitrap. It was measured after the full evaporation ramp, by taking TOF expansions after increasingly long hold times in the millitrap. In Fig. 5.14 we compare the heating rate in the single species cases with those for the mixture, at different final PSDs. In all conditions we observe a significant heating of our samples, strongly dependent on the final level of degeneracy, but which is less affected by the presence of the second species.
To test if the losses at $t_{evap} \gtrsim$38 s could be related to the cooling time, we then compared the final result and PSD evolution produced by different evaporation curves on rubidium. Other than the standard 40 s ramp, we chose two ramps from the set of stretched ones tested for single species ^{87}Rb: the old ramp, with 20 s running time, and

[7] In fact, for a stable production of pure K BECs, the initial balance must be chosen to have Rb evaporated out just during this final section of the millitrap cooling.

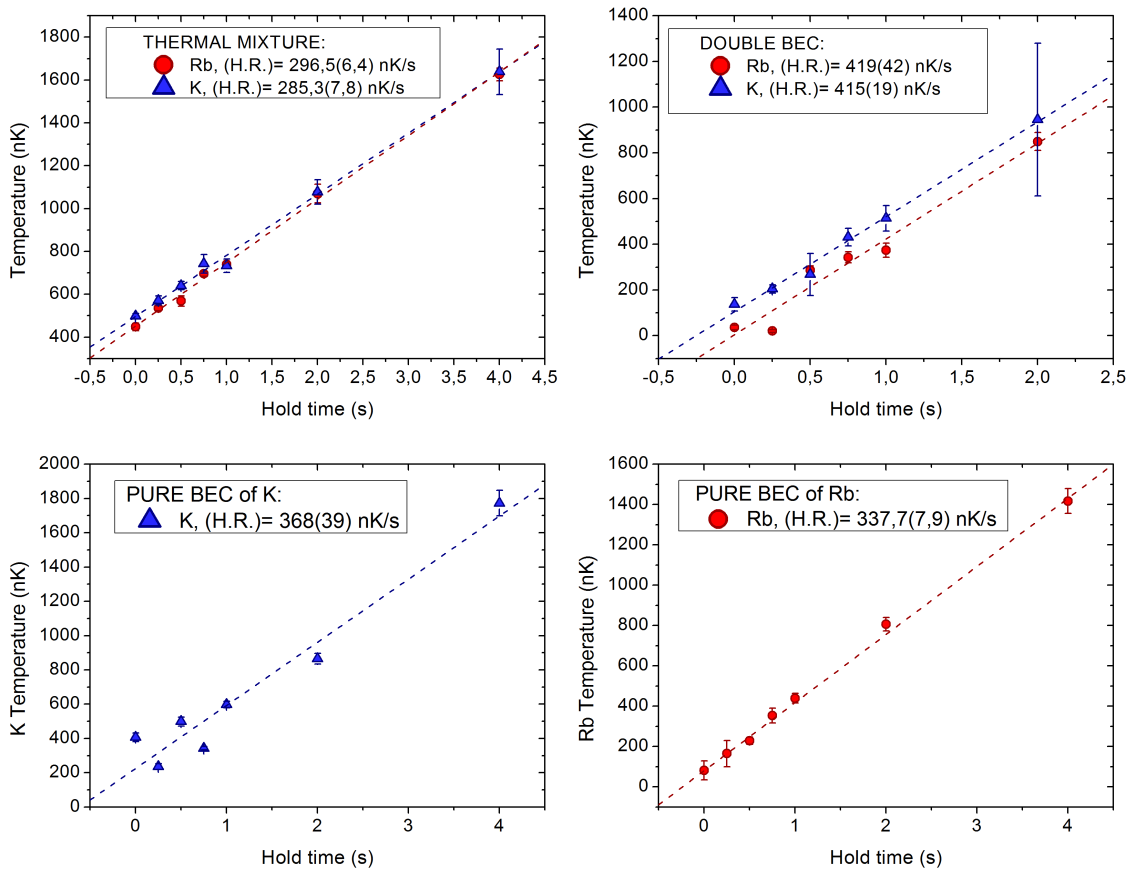

Figure 5.14: Heating rates of rubidium and potassium in the millitrap, after 40 s of evaporative/sympathetic cooling. *Bottom:* only one species in the trap (which for K actually means Rb was evaporated out by the end of the ramp). *Top:* mixture in the trap, for different final evaporation frequencies (right: for 0 hold time there are BECs with thermal components; left: initial condition are thermal samples, close to condensation).

its longest version of 60 s running time[8]. With the mixture we could observe that in order to produce good BEC numbers, slower evaporation ramps require larger initial fractions of potassium for a given rubidium loading.

With our apparatus in the past it has been typically harder to produce a stable double BEC with an unbalance of the kind $N_{\mathrm{Rb}} < N_{\mathrm{K}}$, given the large number fluctuations occurring as a consequence of the sympathetic cooling used on potassium. In search of a better control on this regime, we decided to test the effect of applying a direct evaporation of ^{41}K after an initial purely sympathetic cooling (anyway needed to reach a high enough PSD to initiate the evaporation process). A controlled production of this kind of mixture gives access to other interesting regimes of fundamental problems, such as in the Bose-polaron case [31, 62], where the impurity mass could also be made larger

[8]On rubidium it was the case that the two gave a smaller rubidium BEC than our current ramp, yet comparable between the two.

than the bath one. Another reason was our interest in comparing the decrease of the potassium number during its evaporation with the losses observed for $t_{\mathrm{evap}} \gtrsim 38$ s in the standard procedure.
The evaporative cooling we implemented on ^{41}K occurs via a radio-frequency tuned to the hyperfine splitting of the ground state, acting on the transition $|F = 2, m_F = 2\rangle \rightarrow |F = 1, m_F = 1\rangle$. For its purpose a suitably designed antenna was built, made up of a wide oval copper trace on a dielectric substrate; it is placed over the top viewport of the Main Chamber (and below the top Quadrupole coil on the translation stage), having a large enough internal aperture to let through the vertical beams of 3D-MOT and Probe. The RF power is provided by a signal generator (*HP 8656B*, 0.1-990 MHz) feeding a protected amplifier (*Eaton 3552B*, 100-512 MHz), with a reflective switch placed between the two to ensure fast control on the turning off/on of the frequency on the atoms.
After a series of direct tests, we could identify the earliest time for the RF evaporation to be stably initiated at about 30 s into the rubidium microwave ramp. When performed simultaneously to the rubidium one, the best evaporation profile for potassium directly matches the final section of the microwave ramp, generated by rescaling the ^{87}Rb transition energies to the ^{41}K ones at the corresponding (millitrap) magnetic field. While the addition does not improve the size of our final samples where $N_{\mathrm{Rb}} > N_{\mathrm{K}}$ (the usual running condition), it does effectively stabilize the potassium-dominated degenerate mixture (as the 3D-MOT loading level of K is increased).
When the loading is instead chosen to have rubidium evaporated out before the last 10 s of the evaporation, also different ramps can produce pure BECs of ^{41}K with comparable numbers of $\sim 10^5$.

5.2.1 Optical trap and optical lattices with the mixture

In order to exploit the interspecies Feshbach resonances of our mixture, atoms must be transferred to non-magnetically trappable states, which makes the use of an optical trap necessary. Moreover, the coherence lifetime of our degenerate samples in the millitrap is strongly limited by the reported heating rate.

In the current experimental procedure we perform the transfer from the magnetic to the optical trap before the end of the forced evaporation, after the atoms have been cooled enough to be safely captured by our dipole beams; quantum degeneracy is finally reached by a shorter additional evaporation process directly inside the dipole potential. In fact, during the transfer the atoms are undergo a transformation that has to preserve the degree of coherence of the sample. Our optical trap configuration produces an almost spherically symmetric potential, that strongly deviates from the cigar-shaped one of the millitrap: the different aspect ratios enhance the criticalities of a fast yet adiabatic passage between the two. In particular, the fidelity of the sequence is affected by any relatively small misalignment of the trap beams, inducing a partial depletion of the condensate fraction when performed on a pure BEC.
On top of this, as we could verify, an early passage in the optical potential gives the further advantage of reducing the amount of heating due to the millitrap, which affects

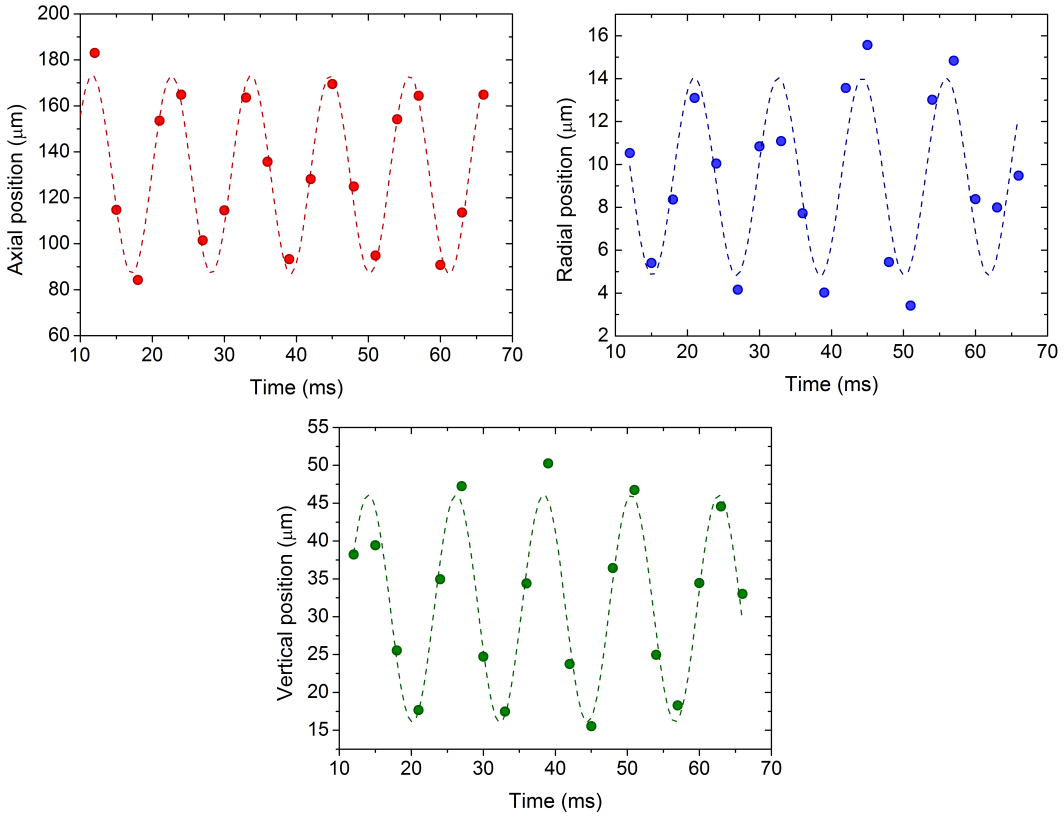

Figure 5.15: Measurement of the optical trap frequencies for ^{87}Rb, with powers of: ≈0.38 W in the axial beam; ≈0.43 W in the radial beam. The oscillations of the cloud (thermal atoms) were induced by suddenly turning on the bias magnetic field in the direction of interest.

the atoms also during the evaporative/sympathetic cooling process.
In the optimal transfer procedure to the crossed-dipole trap, the evaporation is interrupted 35 s into the microwave ramp and the dipole beams are turned on in 200 ms, while the millitrap current is simultaneously ramped down to zero[9]. No significant loss is observed during the transfer, indicating that at this time both species are sufficiently cold for the optical confinement (T_{Rb} <1.5 μK, as expected from Fig. 5.10). Depending on the power balance among the crossed beams, slightly different potentials can be produced.

Inside optical traps, evaporative cooling is carried out by a progressive decrease of the trap beams' intensity in time, that effectively lowers the trap depth and lets the hotter atoms escape from the confinement. With our cross-dipole trap (in the typical configuration of balanced powers and orthogonal alignment), we found that the optimal evaporation profile follows an exponential decay of time constant $\tau = -2$ s, which produces a double BEC as the intensity is decreased in about 4 s.

[9]The microwave is actually turned off only after the magnetic trap field has been zeroed. When the evaporation ramp stops the frequency is kept on at a high value.

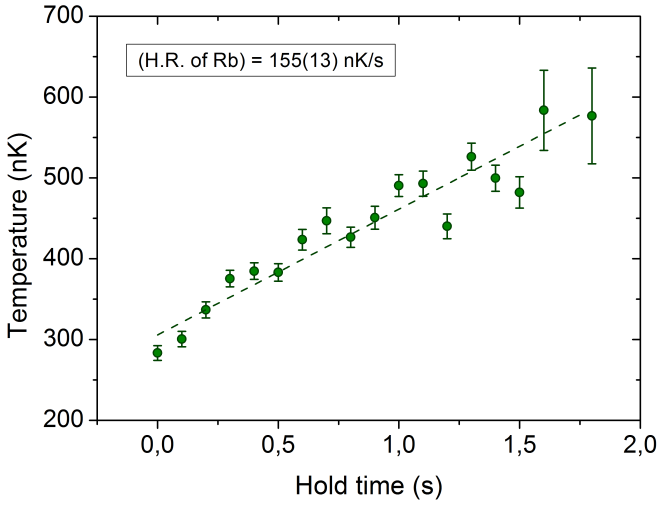

Figure 5.16: Heating of a ^{87}Rb sample inside the crossed-dipole trap, for ~1 W in each trap beam. To produce a sufficiently cold sample in this power configuration, the trap was adiabatically re-compressed (by increasing again the optical power of the beams), after the sample had been evaporated down to quantum degeneracy; the hold time starts after the re-compression.

The harmonic trap frequencies in the final configuration can be obtained with a direct measurement of the sample's oscillation frequency at the relative dipole beam powers, or alternatively from those measured before the optical evaporation, by a direct rescaling of the intensity in each beam to its final value. In typical running conditions, for a pure ^{87}Rb sample we could measure trap frequencies of (Fig. 5.15): $\nu_{\mathrm{axial}^{\mathrm{Rb}}} = 91$ Hz; $\nu_{\mathrm{radial}^{\mathrm{Rb}}} = 86$ Hz; $\nu_{\mathrm{vertical}^{\mathrm{Rb}}} = 82$ Hz. The corresponding frequencies for potassium are derived with the proper mass scaling factor $\nu^{\mathrm{K}} = \nu^{\mathrm{Rb}} \cdot \sqrt{87/41}$.

The condensates produced inside the crossed-dipole trap have comparable numbers to the millitrap ones, still with the possibility to realize different relative populations in the mixture depending on the initial loading. Potassium dominated mixtures can be stabilized also in the optical trap, again using the direct RF evaporation of ^{41}K in the millitrap; in this case, the degenerate samples are produced in the magnetic confinement and only later on transferred to the optical one. Even though this operation causes a reduction of the condensed fractions, the stability in the relative numbers is preserved. Finally, the dipole trap grants a smaller heating rate with respect to the millitrap; in Fig. 5.16, for instance, we report a factor of two reduction over the millitrap one at a comparable initial temperature of the sample.
Because of this condition, degenerate samples in our optical confinement are characterized by a longer coherence lifetime, which allows to perform a number of operations on the double BEC. These include both the hyperfine transfers, to be discussed in the following Section, and the addition of an optical lattice[10], whose turn on procedure

[10]We note that the new optical lattice setup described in Section 2.4.3 has been effectively tested on the samples. Its calibration, realized via the standard method of Kapitza-Dirac diffraction [63], indicated that

alone is characterized by a timescale for adiabaticity of a few hundreds of ms.

5.3 Feshbach resonances and hyperfine transitions

To control the interspecies interaction via the Feshbach resonances, a spatially uniform magnetic field is needed in the trap region, which is again provided by the Quadrupole Coils. At the beginning of the millitrap confinement, they are shut off by the MOSFET circuit and the current flow direction in one of them is flipped, effectively switching to a Helmoltz configuration. Then, the Kepco power supply is initialized so that after the atoms have been moved into the crossed-dipole trap, the coils can be used to produce the desired magnetic field.

Our atomic samples are produced in the internal state $|F = 2, m_F = 2\rangle$ of both species, while the interspecies Feshbach resonances are found in $|1,1\rangle$: inside the optical potential, atoms need to undergo an hyperfine transfer between the two states.
The simplest method to realize such transfers is an adiabatic passage between the two internal states, via Landau-Zener transitions [64], using a proper combination of magnetic field and microwave for Rb (RF for K) [65]. Experimentally, the transfers are induced by applying either a fixed uniform magnetic field (in our case also produced by the Helmoltz coils) or a fixed microwave/RF, while the other parameter is ramped across the resonance value for the atomic transition in the conditions set by the fixed parameter. In both cases, the ramp must be slow enough for the atoms to follow their internal state evolution, through the mixing at the avoided crossing point.
On the renewed apparatus, similarly to the past, with this scheme we could observe transfers on both species throughout the whole magnetic field range of interest for our Feshbach resonances. Unfortunately, an efficient performance of the technique always requires transfer times $\gtrsim$10 ms: this represents a serious limitation in the specific case of our cold samples, for which faster hyperfine transfers are needed. In fact, the ^{87}Rb-^{41}K mixture is stable if both species are in the $|2,2\rangle$ or $|1,1\rangle$ state, but not when the two are in "mixed" states (one in $|1,1\rangle$, the other in $|2,2\rangle$), as it occurs during the intermediate stage of the transfers.
Among the two possible mixed states, the higher one in energy is $\{^{87}\text{Rb}\,|2,2\rangle + {}^{41}\text{K}\,|1,1\rangle\}$, which is therefore unstable against two-body collisions[11].
To prevent these depletion processes, hyperfine transfers must be first performed on rubidium during the experimental sequence.
On the other hand, even the more favorable combination of $\{^{87}\text{Rb}\,|1,1\rangle + {}^{41}\text{K}\,|2,2\rangle\}$ is found to have a large interspecies attraction ($a_{\text{Rb-K}} \approx -2500\,a_0$). This could in principle lead to a collapse of the system, but the gravitational sag reduces the overlap between the two atomic clouds and tends to inhibit the attraction-induced instability.
Nevertheless, we could observe that degeneracy is rapidly lost in this configuration, as a

in our 3D lattice we can achieve depths >60E_R (recoil energies) on ^{87}Rb, with the available optical power.

[11] Spin exchange processes connecting to the opposite configuration are allowed and the latter represents an open channel; the energy released in the process is sufficient to expel the atoms from the trap (≃6.6 GHz, or ≃0.3 K).

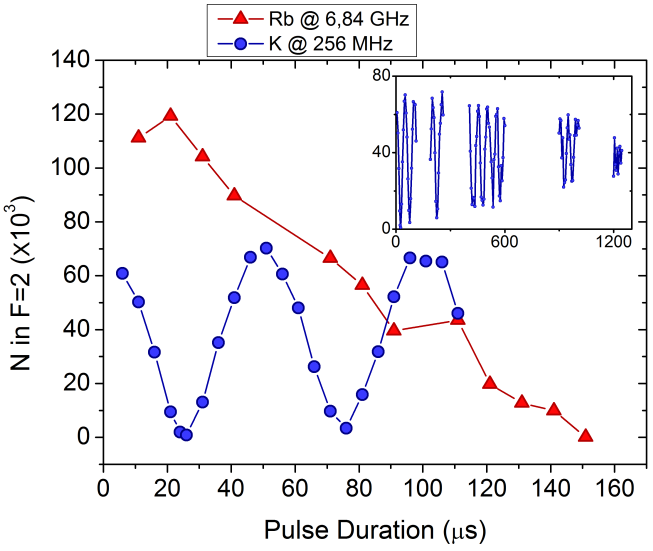

Figure 5.17: Rabi oscillations of the K atom numbers in $F = 2$ (blue dots), at very low magnetic field offset (Quadrupole Coils in Anti-Helmoltz configuration), during the application of the microwave/RF resonant to the hyperfine transition. The inset shows the extended K dataset highlighting the long lived damped oscillations, while the initial oscillations are compared with the first one of Rb number in $F = 2$ (red triangles) under the same experimental conditions.

consequence of the increased three body collisions at high interaction[12]. Starting from fully degenerate samples in $|2,2\rangle$, in the chosen mixed state the coherence is lost over a few tens of milliseconds.

We noted that this heating effect has indeed a smaller impact on thermal samples, but if the transfers are performed before the optical evaporation, the shot-to-shot instability is enhanced in the atom number of the final BECs (and even more noticeably, on the relative population balance).In the last version of the experimental procedure before the rebuilding process, to account for this issue, the total transfer time had been reduced to less than 6 ms so that they could be performed directly on the double BEC in the optical trap. A π-pulse on a two-photon (Raman) optical transition was implemented for the potassium transfer, using a couple of co-propagating beams far-detuned from the D_2 line (770 nm, ~60 mW power each) produced with a Ti:Sapphire laser (*Coherent*), so that the atoms could be fully moved to the $|1,1\rangle$ state in just $\approx 6\ \mu$s [35].

This same scheme is readily adopted also with the renewed apparatus, but it still isn't easily applied to both species, given the drawback of requiring a dedicated large power source for the Raman beams. For this reason, the new optical setup was designed to allow the addition of extra sections for the generation of quasi-resonant Raman beams on each species, tuned close to the respective D_2 lines.

By moving closer to resonance with the single-photon frequency, it is possible to use the standard cooling and repumping laser sources and to also reduce the power require-

[12] For instance, in the single component case, the three-body collision rate depends on the atomic density n as $\langle d\mathcal{N}_3/dt\rangle = K_3 n^2$ and the coefficient scales with the scattering length $K_3 \propto a^4$ for $a \to \infty$.

ments, at the cost of an increased heating rate during the Raman π-pulse. The feasibility of this approach was theoretically tested via numerical simulations, finding the optimal balance between overall Raman detuning and optical power to minimize the heating over the expected duration of the transfer pulse.
Before the setup for two-photon transitions on the D_2 line was built we attempted another approach to reduce the transfer time, using Rabi oscillations on a Raman transition tuned to the hyperfine frequency instead. This one has the advantage of only requiring components already used in the experimental procedure, namely the microwave horn setup on rubidium and the RF antenna on potassium. In particular, it exploits the fact that now short microwave and RF pulses can be performed on our system, owing to the fast switch we added in the rubidium evaporation setup, as well as in the newly implemented potassium one.
In the initial tests, using the Quadrupole Coils in Helmoltz configuration, we could only get mixed signs of transfer, that were very unstable already for the small field of 5 G; Rabi oscillations were rapidly decaying and lacked in reproducibility.
To allow a finer tuning to extremely small values of the magnetic field used for this measurement, we tried setting up the Quadrupole Coils in an anti-Helmoltz scheme, while slightly shifting their axis from the optical trap center; for this configuration we could estimate a ~10 times smaller conversion factor of the current to the actual field offset[13]. In this second case we could efficiently induce Rabi oscillations between $F = 2$ and $F = 1$ on both rubidium and potassium; an example is reported in Fig. 5.17, for a ^{41}K transfer RF set to 256 MHz. The oscillations observed on potassium were long lived, extending over many periods (as shown in the plot inset), and serve as a clear indication that background magnetic fields in our system are small enough for this kind of transfer method to be successfully implemented. Also on rubidium faster oscillations than those reported in Fig. 5.17 could be produced, after a suitable realignment of the horn used for the microwave emission (which increased the effective power level reaching the atomic sample); the Rabi frequency in this case increased up to $\approx 2\pi\cdot 6$ kHz.

Considering our results, the differences between the two configurations can be attributed to a poor control of the current supplied to the Quadrupole Coils.

Throughout all measurements reported in this Section, the current for the Feshbach field was provided by the Kepco power supply in constant current configuration, with its output directly monitored via a *LEM IT-150-S* current transducer (set up with a single winding inside its loop). The value of the Kepco current was set in remote by an analog voltage (with a 1 mA/mV conversion factor) from the electronic boards used to drive the experiment; we note that this voltage output has a resolution of 1 mV, on top of which we could directly observe a rms fluctuation of ≈1.5 mV (at least for values below 1 V).

In the perspective of our hyperfine transfer scheme, current noise affects the process by changing the transition frequency in time via the corresponding magnetic field fluctuation.

[13] Regarding the gradient, it was small enough that the field variation over the extension of the atomic clouds was at all effects negligible, considering the size of the degenerate sample and the ≈ 4 G/(cm·A) conversion factor for the Quadrupole Coils.

A rough general estimate of the maximum noise allowed on the current i, quantified by the rms fluctuation σ_i^{rms} of the latter, can be given under the requirement that the frequency fluctuations it produces must be sufficiently smaller than the Rabi frequency Ω_R. Eventually, any oscillation of the transition frequency occurring much faster than the Rabi flopping shouldn't affect the transfer process, so Ω_R also limits the bandwidth of interest for the current noise[14].
In our specific case a more direct measure for the needed current noise reduction follows by considering that Rabi oscillations could efficiently be produced in the anti-Helmoltz configuration, differently from the Helmoltz case; to match the difference between the two configurations in the conversion factor from current to magnetic field, a reduction of about one order of magnitude is hence due on σ_i^{rms}.

We proceeded to characterize the noise spectrum of the current signal in a series of measurements, performed with a FFT spectrum analyzer (*Agilent 35670-90053*), and the results we obtained are presented in the plots of Fig. 5.18. The second one reports the noise on the circuit loop as seen on the voltage signal output of the LEM current-transducer, normally used for to monitor the stabilization. For the curves in the first plot instead, the current noise was measured on the sensing connections of the 0.5 Ω precision resistor (*Isabellenhütte RUG-Z*) which is part of the circuit loop, directly in series to the cathode output of the supply. For further comparison, corresponding curves in identical conditions were acquired with two distinct current supplies: the Kepco BOP-10-20M and a *Agilent N55744A* (second two plots of Fig. 5.18).

A calculation of its σ_{rms} across the considered bandwidth of the first plot yields values from 0.48 mA to 0.55 mA, as the current is increased between 0.5 A and 5 A. For the Agilent supply a comparatively larger variation of σ_{rms} occurs, whose value at the same currents goes from 0.28 mA to 1.2 mA.
Notably, also the condition derived on σ_i^{rms} from the magnitude of the Rabi frequency indicates a due reduction of the Kepco current noise by a rough factor of 10. Still, it nevertheless represents a more favorable solution than the Agilent supply, given the limited increase of its σ_{rms} at higher current (ultimately, in the experiment, a current of about 9 A is needed to produce the necessary field for the interaction tuning, at which the hyperfine transfers are meant to take place).
In agreement with this conclusion, we note that in the Kepco noise spectrum a larger contribution is brought in by smaller frequencies, which are a priori easier to be compensated.

Finally, these results are driving our implementation of an active stabilization method on the Quadrupole Coils circuit. A parallel observation in this perspective was made regarding the sensing method, where the noise spectra served to address the precision resistor as a cleaner device for current sensing; in fact, even if our current transducer in principle allows to measure the current more closely to the Coils than

[14] If the maximum Rabi frequency observed on rubidium (≈6 kHz) is taken as a reference, by considering the deviation on the $|1,1\rangle \rightarrow |2,2\rangle$ transition frequency with magnetic field (2.1 MHz/G) and the calibration for the Quadrupole Coils in Helmoltz configuration (8 G/A), the request of Ω_R fluctuating by <1 kHz results in a condition of $\sigma_i^{\mathrm{rms}} \lesssim 6 \times 10^{-5}$ A over frequencies up to $\Omega_{\mathrm{Rabi}}/(2\pi)$.

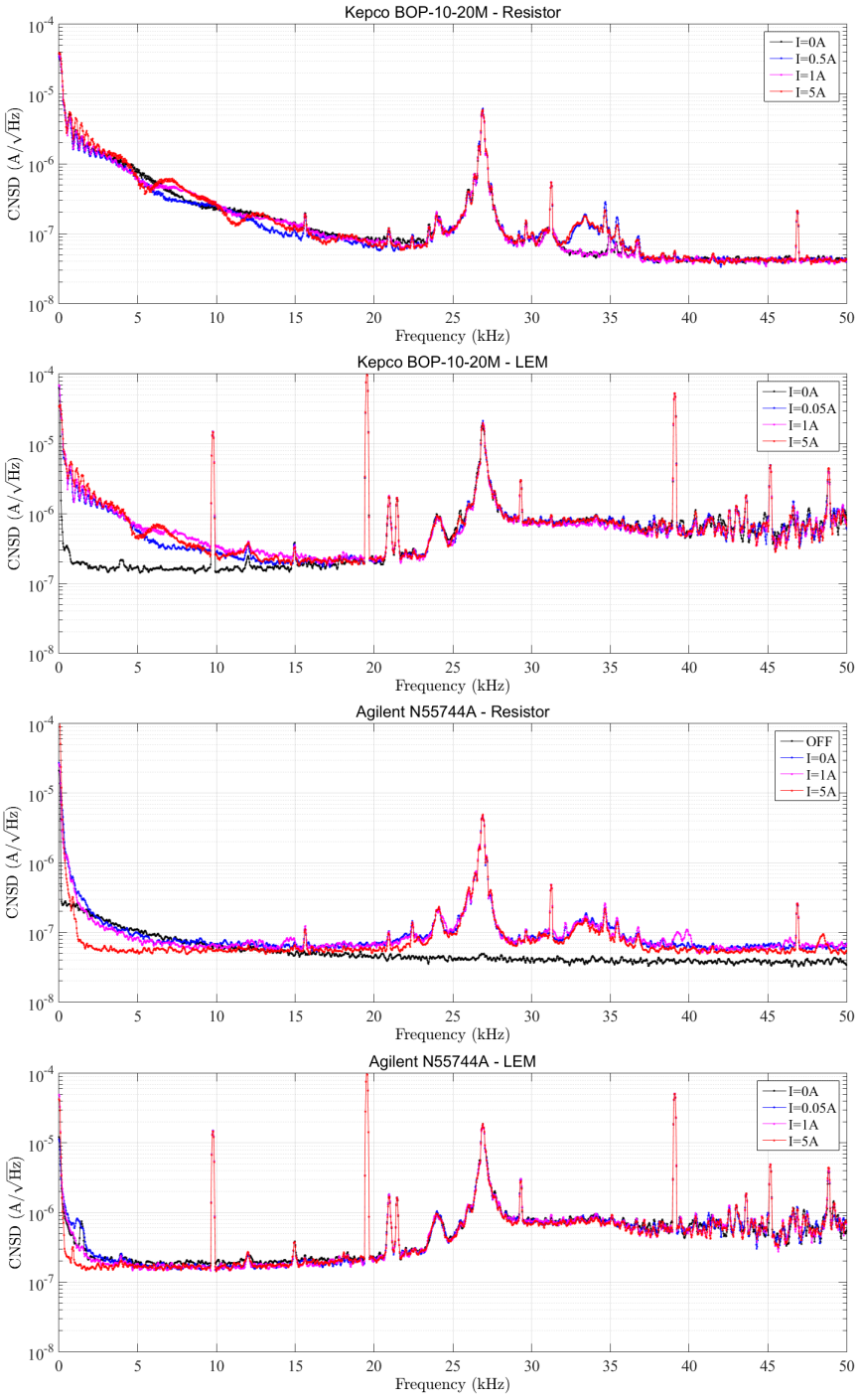

Figure 5.18: Noise plots for the Feshbach field current supplies (see titles for reference) set at different current values (see legend). The two top plot refer to the Kepco BOP-10-20M supply, while the second two ones to the Agilent N55744A supply. The titles indicate whether in each plot the current noise was measured on the 0.5 Ω resistor (*Resistor*) or via the current transducer (*LEM*), respectively. For all measurements the spectrum analyzer was used in AC mode, with a 64 Hz resolution (1600 points) and a bandwidth from 0 Hz to 102.4 kHz. In the plots, as in the following analysis, we restricted ourselves to frequencies within 50 kHz (about one order of magnitude larger than the reference Ω_R).

the resistor, the spectra from the relative plots in Fig. 5.18 show that it significantly contributes to the noise amplitude.

Outline

The results we presented so far demonstrated the effect of the upgrades operated on the system, and how they reflected in the re-optimized procedure.

On the technical side, the new optical setup we built under an optimized design has greatly improved the stability and ease of use of the system. The combination of our optical scheme with an offset lock has granted us a wider tuning range in the frequencies of our Rubidium sources, and a reduction in the response time that is suitable for a fast tuning of the frequencies while running the experiment (as for the purpose of using the light from cooling sources for quasi-resonant Raman transfers at the magnetic field of Feshbach resonances).
The more compact version of the vacuum setup has proved to be a valid alternative to the originary apparatus with separate pre-cooling chambers, with no apparent trade-off to its desirable reduction of the system's volume (and vacuum capacity).

In terms of experimental conditions, a crucial improvement was seen in the the size of our doubly degenerate samples (and in the reproducibility of the final numbers of our mixture), which was increased to at least 5 times its original value. Of particular importance in this sense were the choices of adding new TAs, dedicated to the production of 2D-MOT lights, and using an enriched atomic source of ^{41}K; on top of the latter, we can also list the improvement of our vacuum quality as a positive factor, which allowed for a longer yet more efficient evaporative cooling on ^{87}Rb.
By introducing the possibility of a partial direct evaporation on potassium we could extend the range of unbalanced mixtures that can be produced (in a controllable way), to the limit case where potassium is the dominant species in the double degenerate sample, both in the millitrap and the crossed-dipole trap.

A detailed characterization performed on the working system has lead to a deeper understanding of the mechanisms driving the sample preparation procedure. From its results, we could address the number of rubidium atoms that are captured inside the millitrap as the main factor limiting the size of our degenerate samples; consequently, even larger BECs are to be expected simply by improving the loading quality of ^{87}Rb in the 3D-MOT.
Specific attention was payed, throughout the characterization process, in identifying the loss mechanisms in the ^{87}Rb-^{41}K mixture at each stage. A relevant loss channel in the millitrap is minimized by actively fighting the presence of atoms with smaller magnetic moments; during the 3D-MOT stage, different kinds of radiative emissions contribute in limiting the maximum size of the clouds.

Finally we are in the process of testing two different solutions for a new fast hyperfine transfer scheme, whose setups were already implemented, and we could identify that the magnetic field stability of the system can be enhanced by improving the quality of our current stabilization on the Quadrupole Coils' supplies. The reduction of magnetic field noise in the experiment represents a key passage in perspective for all measurements on the physics of impurities: many-body effects often show up as magnetic field-dependent variations over quantities of interests, as in the paradigmatic example of the transition energy shift due to the Bose polaron binding energy [32].

Appendix A

Design of the Tapered Amplifier mount

In modern cold atoms experiments large optical powers are needed, and tapered amplifiers (TAs) are ubiquitous as a solution to the limited emission of bare laser diodes in the near infrared wavelength range (600-1200 nm). For state-of-the-art TAs, provided an injection power of 15-20 mW, the emission power ranges from several hundreds of mW to ~2.5 W, depending on the length of the tapered section (and the working wavelength).
The TA chip is constituted by a thin structure, in which the injection light travels across an index-guided waveguide [66]: an initial short and narrow section (length <1 mm, width ~1 μm) is followed by a second longer one, which is tapered in the transverse direction; the divergence angle θ of the latter is chosen so that the diffracted light from the first section proceeds to occupy the whole tapered region, getting an amplification from the active medium (Fig. A.1b)). For the device to work efficiently, both the input and the output facet have to be anti-reflection coated, to only allow the one way passage of the ingoing beam and avoiding multiple reflections, whose power build up would easily destroy the chip.
Given the aspect ratio of the waveguide on the output facet of the chip, the emission mode rapidly diverges over a distance along the transverse direction, where the aperture is much narrower, while more slowly expanding along the tapered one. To collimate the diverging output, a combination of a short focal length lens (of a few mm, typically, which collimates the transverse direction while focusing the tapered one) with a cylindrical lens is used; at the input facet, instead, the symmetric injection aperture only requires a single aspheric lens collimator.

While fully mounted setups are commercially available (often as a full MOPA system including the injection source), they are typically expensive and it is not uncommon to use homemade designed mounts for this kind of devices, given the simple and relatively cheap setup they actually require.
As a trade-off, homemade mounted systems also typically expose the TA parts to a larger risk of corruption in the set-up process, considering the strong susceptibility of the chips to external damages. The most common ones include:

- *Electrostatic damage:* TAs are static-charge-sensitive devices, very easily damaged

in the handling process;

- *Damage to the anti-reflection coating:* it can occur optically, due to reflections hitting the chip during the alignment process of either of the optics, or also consequently to the formation of deposits onto the input/output facet, from water condensing off the air or fuming of chemicals (glues,etc) used in the mounting assembly;

- *Mechanical damage:* which often refers to a bending of the thin cathode connection strings, when setting up the chip or even after the process, in the case where the chip isn't properly enclosed.

In their most common version, TA chips are mounted over a *C-mount* as shown in Fig. A.1a): the small chip, with its floating contact being the metallic flag which protrudes from the top, is mounted on top of a bulk metallic part, that is shorted to the ground connection of the chip itself and also provides the contact for the overall cooling.
In the course of my PhD, I designed a new adjustable mount for commercially available C-mounted Tapered Amplifiers. The driving reason was that on our experiment, before building the new optical setup, the assembly design originally used for the TAs was not at all robust against many of the aforementioned issues. Most notably: the TA was only mechanically shielded by an outer removable casing (about 2 cm away from the contacts), which didn't prevent dust particles from flowing close to the chip; glue was used to fix into place both collimators, after their alignment with an external three-axis translation stage, which was exposed to misalignment during the drying process. A large number of degree of freedom was left available in the set-up stage, to compensate for the poor control on the chip placement, which caused the mounting and aligning process to be hard, potentially harmful and often poorly successful.
The concept of the new assembly design is based on the idea of minimizing the amount of alignment needed, while still leaving some freedom of movement, especially using no glue in any of the parts. For this purpose, the TA placement was made reproducible and the two collimators were set up to ensure they are by construction on axis with each other and with the emission direction. An early version of the design was then adapted not to require very high precision machining (a resolution above 1/100 of a mm, like in wire-erosion machines), by implementing a small degree of adjustability in the parts[1]. In particular, all four holes for the screws holding the Collimator Mount were widened 0.1 mm beyond the minimum diameter for M3 screws, and three micrometric screws were added for the fine alignment of the optics (two opposing ones horizontally, plus a single vertical one). The final assembly is composed by two main pieces (Fig. A.2):

1) TA Support (or Bottom Part): It has a main central aperture to host the C-mount, leaving it no freedom to rotate away from the horizontal alignment, where the ground

[1] Besides, this also compensates for the uncertainty in the vertical position of the TA emission, due to the chip production process, which is reported by some companies to be $\lesssim$0.1 mm.

connection is fixed with a screw (leaving the anode connection floating about 1 mm above the mount). In the larger one of the pillars on the two sides, the bottom aperture lets a wire through, to be connected onto the anode of the chip; the other two holes hold the extremely fine adjusters for transverse alignment of the collimators (commercially available parts from Thorlabs were used: *F2D5ES12* M2.5 screws; *F2D5ESN1P* threaded bushings). This part is machined in copper, ensuring a proper thermal conductivity.

2) Collimator Mount (or Top Part): It is built from a steel parallelepiped, by removing a central slice of 5 mm thickness over two thirds of the part's height. Orthogonal to the cut plane, along the direction corresponding to the TA emission axis, a single through hole is operated and threaded to insert the collimators from the two extremities. Each of them is held inside via a commercial plastic adapter (*Thorlabs S05TM0x series*, depending on the specific aspheric lens) for which the hole is threaded, which allows a stable and easy adjustment along the focal (emission) axis. It is assembled to the TA Support with two M3-threaded screws, which press it against the Support side facing the output facet of the chip.
Finally, the whole system (via the TA Support) is screwed onto a copper plate, underneath which a Peltier cell is placed to provide temperature stabilization to the system.

For assembling, after the chip has been mounted onto its holder and the electrical connection have been made, the top part is placed in and loosely screwed onto the output side; an initial alignment along the transverse and longitudinal axes is then operated on the free-running emission of the TA, turned on at a its lower threshold current for operation (~0.9 A), and the screws fixing the top part are further tightened. Once the TA is injected, final adjustments for the transverse horizontal direction are operated with the three adjustment screws while progressively tightening the two other screws, holding the Collimator Mount.
This procedure is reproducible and rapid, only requiring a few minutes for a working system, which include the alignment of the collimators. Nevertheless, this latter operation can be safely repeated from scratch, without removing or exposing the chip to damage risks; in fact, the mechanical design prevents any part from touching the chip, even at the maximum bending angle of the Collimator Mount, for as long as its screws are connected to the TA holder.

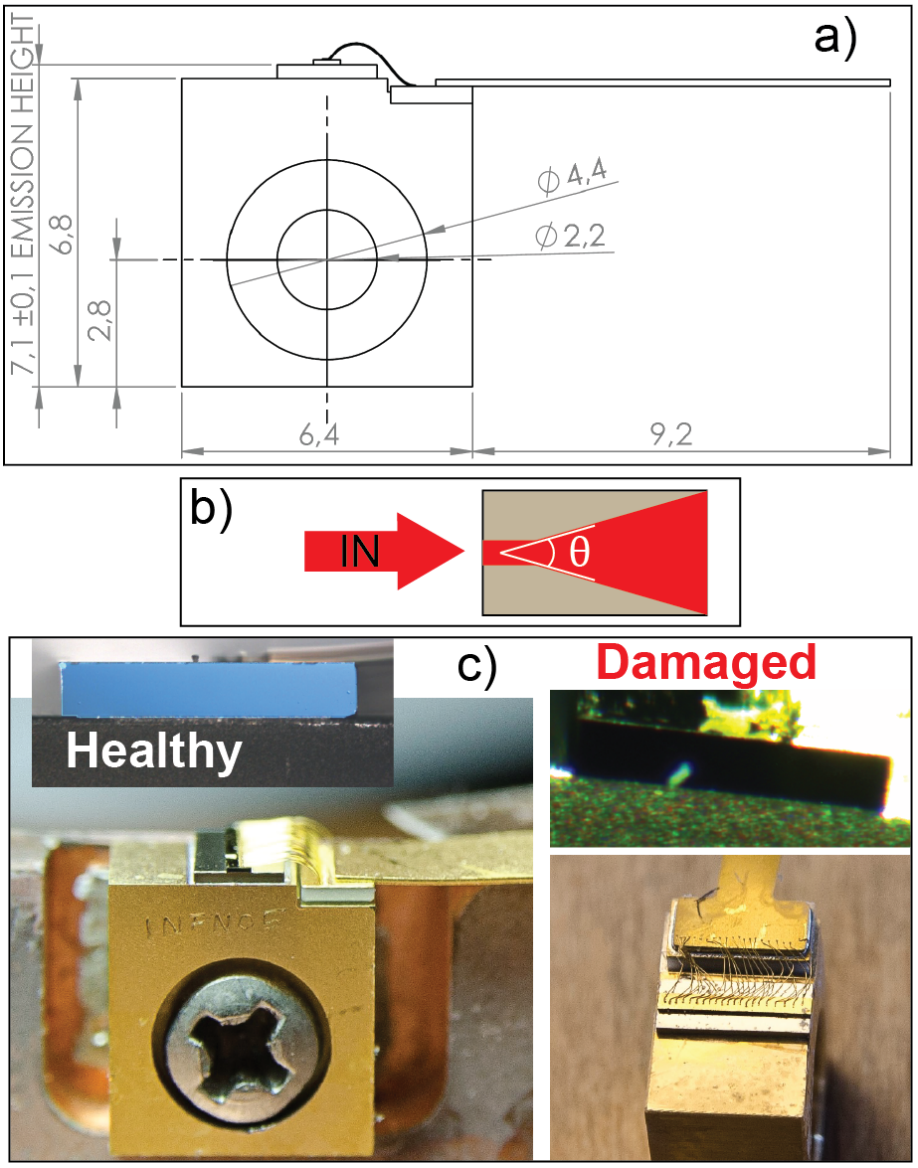

Figure A.1: a) Design of a C-mounted Tapered amplifier (Front view, from: *http://www.m2k-laser.de*). b) Depiction of the TA chip waveguides' profile, from top view. c) Pictures of a working TA component are compared with two examples of damaged ones; the insets show the (anti-reflection coated) front facet of the chip.

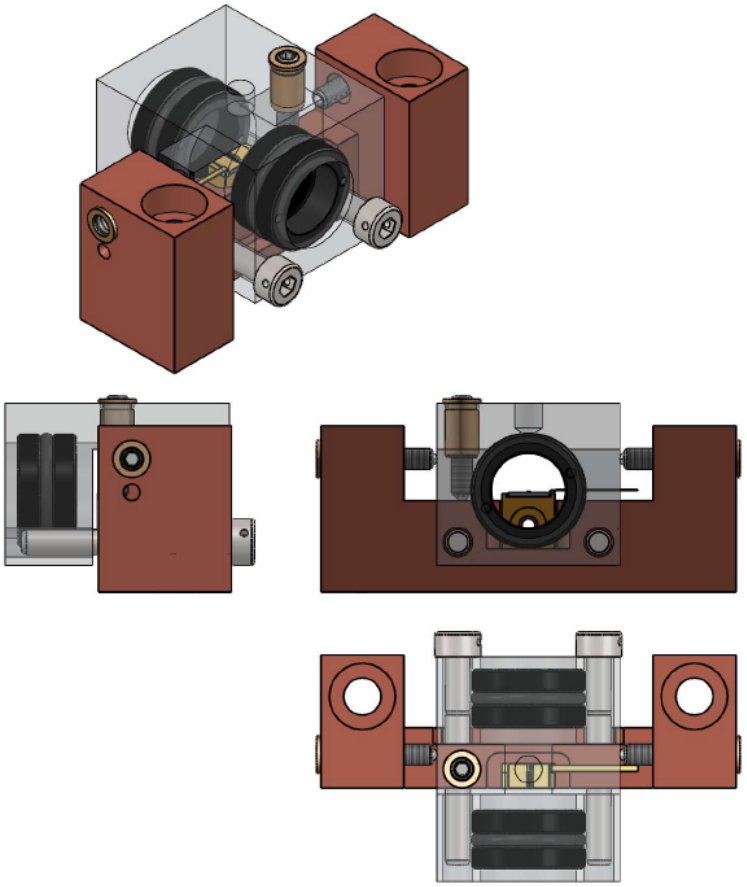

Figure A.2: Schematic visions of the designed TA assembly from different angles.

Where is the string that Theseus laid?
Find me out this labyrinth place.

Bibliography

[1] J. R. Anglin and W. Ketterle, "Bose-Einstein condensation of atomic gases", Nature **416**, 211 (2002).

[2] A. D. Cronin, J. Schmiedmayer, and D. E. Pritchard, "Optics and interferometry with atoms and molecules", Rev. Mod. Phys. **81**, 1051 (2009).

[3] I. Bloch, J. Dalibard, and S. Nascimbene, "Quantum simulations with ultracold atomic gases", Nat. Phys. **8**, 267 (2012).

[4] C. Chin, R. Grimm, P. Julienne, and E. Tiesinga, "Feshbach resonances in ultracold gases", Rev. Mod. Phys. **82**, 1225 (2010).

[5] M. Lewenstein, A. Sanpera, and V. Ahufinger, *Ultracold atoms in optical lattices: simulating quantum many-body systems* (OUP Oxford, 2012).

[6] M. Greiner, O. Mandel, T. Esslinger, T. Hänsch, and I. Bloch, "Quantum phase transition from a superfluid to a Mott insulator in a gas of ultracold atoms", Nature **415**, 39 (2002).

[7] S. Trotzky, L. Pollet, F. Gerbier, U. Schnorrberger, I. Bloch, N. V. Prokof'ev, B. Svistunov, and M. Troyer, "Suppression of the critical temperature for superfluidity near the Mott transition", Nat. Phys. **6**, 998 (2010).

[8] M. Endres, T. Fukuhara, D. Pekker, M. Cheneau, P. Schau, C. Gross, E. Demler, S. Kuhr, and I. Bloch, "The Higgs amplitude mode at the two-dimensional superfluid/Mott insulator transition", Nature **487**, 454 (2012).

[9] J. Dalibard, F. Gerbier, G. Juzeliunas, and P. Öhberg, "Colloquium: artificial gauge potentials for neutral atoms", Rev. Mod. Phys. **83**, 1523 (2011).

[10] N. Goldman, G. Juzeliunas, P. Öhberg, and I. B. Spielman, "Light-induced gauge fields for ultracold atoms", Rep. Prog. Phys. **77**, 126401 (2014).

[11] W. S. Bakr, A. Peng, M. E. Tai, R. Ma, J. Simon, J. I. Gillen, S. Fölling, L. Pollet, and G. M., "Probing the superfluid-to-Mott insulator transition at the single-atom level", Science **329**, 547 (2010).

[12] J. F. Sherson, C. Weitenberg, M. Endres, M. Cheneau, I. Bloch, and S. Kuhr, "Single-atom-resolved fluorescence imaging of an atomic Mott insulator", Nature **467**, 68 (2010).

[13] M. F. Parsons, F. Huber, A. Mazurenko, C. S. Chiu, W. Setiawan, K. Wooley-Brown, S. Blatt, and M. Greiner, "Site-resolved imaging of fermionic ^{6}Li in an optical lattice", Phys. Rev. Lett. **114**, 213002 (2015).

[14] A. V. Gorshkov, M. Hermele, V. Gurarie, C. Xu, P. S. Julienne, J. Ye, P. Zoller, E. Demler, and A. M. Lukin, M. D.and Rey, "Two-orbital SU(N) magnetism with ultracold alkaline-earth atoms", Nat. Phys. **6**, 289 (2010).

[15] S. Taie, R. Yamazaki, S. Sugawa, and Y. Takahashi, "An SU(6) Mott insulator of an atomic Fermi gas realized by large-spin Pomeranchuk cooling", Nat. Phys. **8**, 825 (2012).

[16] F. Scazza, C. Hofrichter, Höfer, P. C. De Groot, I. Bloch, and S. Fölling, "Observation of two-orbital spin-exchange interactions with ultracold SU(N)-symmetric fermions", Nat. Phys. **10**, 779 (2014).

[17] T. Lahaye, C. Menotti, L. Santos, M. Lewenstein, and T. Pfau, "The physics of dipolar bosonic quantum gases", Rep. Prog. Phys. **72**, 126401 (2009).

[18] G. Roati, F. Riboli, G. Modugno, and M. Inguscio, "Fermi-Bose quantum degenerate ^{40}K-^{87}Rb mixture with attractive interaction", Phys. Rev. Lett. **89**, 150403 (2002).

[19] S. Ospelkaus, C. Ospelkaus, R. Dinter, J. Fuchs, M. Nakat, K. Sengstock, and K. Bongs, "Degenerate K-Rb Fermi-Bose gas mixtures with large particle numbers", J. Mod. Opt. **54**, 661 (2007).

[20] A. Schirotzek, C.-H. Wu, A. Sommer, and M. W. Zwierlein, "Observation of Fermi polarons in a tunable Fermi liquid of ultracold atoms", Phys. Rev. Lett. **102**, 230402 (2009).

[21] M. Koschorreck, D. Pertot, E. Vogt, B. Frölich, M. Feld, and M. Köhl, "Attractive and repulsive Fermi polarons in two dimensions", Nature **485**, 619 (2012).

[22] A. Kuklov, N. Prokof'ev, and B. Svistunov, "Commensurate two-component bosons in an optical lattice: ground state phase diagram", Phys. Rev. Lett. **92**, 050402 (2004).

[23] S. Mandal, K. Saha, and K. Sengupta, "Superfluid-insulator transition of two-species bosons with spin-orbit coupling", Phys. Rev. B **86**, 155101 (2012).

[24] E. Altman, W. Hofstetter, E. Demler, and M. D. Lukin, "Phase diagram of two-component bosons on an optical lattice", New J. Phys. **5**, 113 (2003).

[25] E. Altman, E. Demler, and M. D. Lukin, "Probing many-body states of ultracold atoms via noise correlations", Phys. Rev. A **70**, 013603 (2004).

[26] G. Thalhammer, G. Barontini, L. De Sarlo, J. Catani, F. Minardi, and M. Inguscio, "Double species Bose-Einstein condensate with tunable interspecies interactions", Phys. Rev. Lett. **100**, 210402 (2008).

[27] J. Catani, L. De Sarlo, G. Barontini, F. Minardi, and M. Inguscio, "Degenerate bose-bose mixture in a three-dimensional optical lattice", Phys. Rev. A **77**, 011603 (2008).

[28] J. Catani, G. Lamporesi, D. Naik, M. Gring, M. Inguscio, F. Minardi, A. Kantian, and T. Giamarchi, "Quantum dynamics of impurities in a one-dimensional bose gas", Phys. Rev. A **85**, 023623 (2012).

[29] B. Capogrosso-Sansone, G. Söyler, N. V. Prokof'ev, and B. V. Svistunov, "Critical entropies for magnetic ordering in bosonic mixtures on a lattice", Phys. Rev. A **81**, 053622 (2010).

[30] M. Guglielmino, V. Penna, and B. Capogrosso-Sansone, "Ising antiferromagnet with ultracold bosonic mixtures confined in a harmonic trap", Phys. Rev. A **84**, 031603 (2011).

[31] D. Benjamin and E. Demler, "Variational polaron method for Bose-Bose mixtures", Phys. Rev. A **89**, 033615 (2014).

[32] A. Shashi, F. Grusdt, D. A. Abanin, and E. Demler, "Radio-frequency spectroscopy of polarons in ultracold Bose gases", Phys. Rev. A **89**, 053617 (2014).

[33] S. Trotzky, Y.-A. Chen, U. Schnorrberger, P. Cheinet, and I. Bloch, "Controlling and detecting spin correlations of ultracold atoms in optical lattices", Phys. Rev. Lett. **105**, 265303 (2010).

[34] D. Greif, T. Uehlinger, G. Jotzu, L. Tarruell, and T. Esslinger, "Short-range quantum magnetism of ultracold fermions in an optical lattice", Science **340**, 1307 (2013).

[35] S. Conclave, "Transizione di Mott in una miscela Bose-Bose a interazioni controllabili", MA thesis (Università di Roma "La Sapienza", 2012).

[36] F. Dalfovo, S. Giorgini, L. Pitaevskii, and S. Stringari, "Theory of Bose-Einstein condensation in trapped gases", Rev. Mod. Phys. **71**, 463 (1999).

[37] C. Pethick and H. Smith, *Bose-Einstein condensation in dilute gases* (Cambridge University Press, 2002).

[38] M. H. Anderson, J. R. Ensher, M. R. Matthews, C. E. Wieman, and E. A. Cornell, "Observation of Bose-Einstein condensation in a dilute atomic vapor", Science **269**, 198 (1995).

[39] K. B. Davis, M.-O. Mewes, M. R. Andrews, N. J. van Druten, D. S. Durfee, D. M. Kurn, and W. Ketterle, "Bose-Einstein condensation in a gas of sodium atoms", Phys. Rev. Lett. **75**, 3969 (1995).

[40] W. Ketterle, D. S. Durfee, and D. M. Stamper-Kurn, "Making, probing and understanding Bose-Einstein condensates", in *Proceedings of the International School of Physics "Enrico Fermi", Course CXL*, edited by M. Inguscio, S. Stringari, and C. E. Wieman (IOS Press, 1999), p. 67.

[41] A. Polkovnikov, K. Sengupta, A. Silva, and M. Vengalattore, "Colloquium: Nonequilibrium dynamics of closed interacting quantum systems", Rev. Mod. Phys. **83**, 863 (2011).

[42] C. Cohen-Tannoudji, "Atomic motion in laser light", in *Fundamental systems in quantum optics, Les Houches session LIII (1990)*, edited by J. Dalibard, J.-M. Raimond, and J. Zinn-Justin (Nort-Holland, 1992).

[43] H. Metcalf and P. Van der Straten, *Laser cooling and trapping* (Springer, 2002).

[44] C. Adams and E. Riis, "Laser cooling and trapping of neutral atoms", Prog. Quant. Electron. **21**, 1 (1997).

[45] J. Jersblad, H. Ellmann, K. Stöchkel, A. Kastberg, L. Sanchez-Palencia, and R. Kaiser, "Non-gaussian velocity distributions in optical lattices", Phys. Rev. A **69**, 013410 (2004).

[46] C. M. Dion, P. Sjölund, S. J. H. Petra, S. Jonsell, and A. Kastberg, "Time dependence of laser cooling in optical lattices", Europhys. Lett. **72**, 369 (2005).

[47] R. Grimm, M. Weidemüller, and Y. Ovchinikov, "Optical dipole traps for neutral atoms", Adv. At., Mol., Opt. Phys. **42**, 95 (2000).

[48] G. Thalhammer, B. G., L. De Sarlo, J. Catani, F. Minardi, and M. Inguscio, "Double species Bose-Einstein condensate with tunable interspecies interactions", Phys. Rev. Lett. **100**, 210402 (2008).

[49] T. Volz, S. Dürr, S. Ernst, A. Marte, and G. Rempe, "Characterization of elastic scattering near a Feshbach resonance in ^{87}Rb", Phys. Rev. A **68**, 010702 (2003).

[50] R. Côté, A. Dalgarno, H. Wang, and W. C. Stwalley, "Potassium scattering lengths and prospects for Bose-Einstein condensation and sympathetic cooling", Phys. Rev. A **57**, 4118 (1998).

[51] S. Ospelkaus-Schwarzer, "Quantum degenerate Fermi-Bose mixtures of ^{40}K and ^{87}Rb in 3D optical lattices", PhD thesis (Universität Hamburg, 2006).

[52] J. Catani, "A new apparatus for ultracold K-Rb Bose-Bose atomic mixtures", PhD thesis (Universitá degli Studi di Firenze, 2006).

[53] H. Rutt, "A heterodyne frequency offset locking technique for pulsed or CW lasers", Journ. Phys. E **17**, 704 (1984).

[54] U. Schünemann, H. Engler, R. Grimm, M. Weidemüller, and M. Zielonkowskic, "Simple scheme for tunable frequency offset locking of two lasers", Rev. Sci. Instr. **70**, 242 (1999).

[55] M. Joffe, W. Ketterle, A. Martin, and D. Pritchard, "Transverse cooling and deflection of an atomic beam inside a Zeeman slower", J. Opt. Soc. Am. B **10**, 2257 (1993).

[56] J.-F. Clément, J.-P. Brantut, M. Robert-de-Saint-Vincent, R. A. Nyman, A. Aspect, T. Bourdel, and P. Bouyer, "All-optical runaway evaporation to Bose-Einstein condensation", Phys. Rev. A **79**, 061406 (2009).

[57] W. Ketterle and N. J. van Druten, "Evaporative cooling of atoms", Adv. At., Mol., Opt. Phys. **37**, 181 (1996).

[58] M. Landini, S. Roy, L. Carcagní, D. Trypogeorgos, M. Fattori, M. Inguscio, and M. G., "Sub-Doppler laser cooling of potassium atoms", Phys. Rev. A **84**, 043432 (2011).

[59] J. Goldwin, S. B. Papp, B. DeMarco, and D. S. Jin, "Two-species magneto-optical trap with ^{40}K and ^{87}Rb", Phys. Rev. A **65**, 021402 (2002).

[60] L. G. Marcassa, G. D. Telles, S. R. Muniz, and V. S. Bagnato, "Collisional losses in a K-Rb cold mixture", Phys. Rev. A **63**, 013413 (2000).

[61] M. W. Mancini, A. R. L. Caires, G. D. Telles, V. S. Bagnato, and L. G. Marcassa, "Trap loss rate for heteronuclear cold collisions in two species magneto-optical trap", EPJ D **30**, 105 (2004).

[62] A. G. Volosniev, H.-W. Hammer, and N. T. Zinner, "Real-time dynamics of an impurity in an ideal Bose gas in a trap", Phys. Rev. A **92**, 023623 (2015).

[63] B. Gadway, D. Pertot, R. Reimann, M. G. Cohen, and D. Schneble, "Analysis of Kapitza-Dirac diffraction patterns beyond the Raman-Nath regime", Opt. Express **17**, 19173 (2009).

[64] C. Zener, "Non-adiabatic crossing of energy levels", Proc. R. Soc. A **137**, 696 (1932).

[65] M.-O. Mewes, M. R. Andrews, D. M. Kurn, D. S. Durfee, C. G. Townsend, and W. Ketterle, "Output coupler for Bose-Einstein condensed atoms", Phys. Rev. Lett. **78**, 582 (1997).

[66] J. Walpole, "Semiconductor amplifiers and lasers with tapered gain regions", Optical and Quantum Electronics **28**, 623 (1996).